Technische Universität Berlin

Effect of spontaneous emission lifetime on the linear stability properties of a nanocavity laser

Master Thesis

Thorben Kaul
314362

December 20, 2014

1st supervisor: Prof. Dr. Eckehard Schöll
2nd supervisor: Prof. Dr. habil. Kathy Lüdge

Hiermit erkläre ich, dass ich die vorliegende Arbeit selbständig und eigenhändig sowie ohne unerlaubte fremde Hilfe und ausschließlich unter Verwendung der aufgeführten Quellen und Hilfsmittel angefertigt habe.

Die selbständige und eigenständige Anfertigung versichert an Eides statt:

Berlin, den 20.12.2014

_____

Contents

1 Introduction

The hour of birth of laser theory can be traced back to the prediction [EIN17] of the basic effect of stimulated emission by Albert Einstein in 1916, what gives the laser principle its name (*light amplification by stimulated emission of radiation*). At this point the knowledge about the possibility of a light field amplification by this effect was not present and came up a few years later. Nonetheless the process from there to the first real laser device in 1960 [MAI60] (ruby solid state laser) took a long time, as the generation of the necessary population inversion was not easy to realize [SCH58]. Only two years later the first GaAs semiconductor laser appeared. Today lasers are omnipresent in our society. They are getting utilized in medical science, materials processing, entertainment industry, measurement technology, spectroscopy, fundamental research, nuclear fusion and last but not least in telecommunications.
The benefit of semiconductor laser devices compared to *light emitting diodes* (LED) with respect to their usage as optical communication devices and amplifiers [WEG10, MAJ10] is large. Even if they are more expensive to manufacture, they are highly suitable for long range communication due to their energy yield, better modulability, fast switching times and broadbanded emission. However the relatively short lifetime of early bulk semiconductor devices was disadvantageous, which may be connected to their temperature sensitivity. The appealing properties of self-assembled quantum dot lasers could provide a solution in this matter, as they show up temperature independency and reduced threshold currents. Compared to quantum well lasers these devices provide a lower energy consumption, a low linewidth enhancement factor and a greater tolerance to optical feedback [GLO12, OTT12, PAU12]. All these properties are favourable to optoelectronic data transmission devices. Therefore quantum dot lasers show lower output power compared to quantum well lasers. Besides many other effects, the *small signal response* is a major characteristic of a device for suitability in this field of application. Higher modulation speed, higher data transfer rates, lower energy and material consumption, lower manufacturing costs are aspired by today's industry.
In fact the tendency of miniaturization and integration of optical components fulfills these criteria. One future vision for nanolasers are optical driven computer chips with an enormously increased communication speed and efficiency. Decreasing the cavity size down to the nanoscale further changes stability properties [NIN10] and the effect of Purcell enhancement of spontaneous emission is unavoidably included, as altering the cavity size takes effect on the photonic density of states. It is known, that certain devices, even with micro-sized cavities, would not reach the lasing threshold, without considering Purcell enhanced rates [GRE12a]. Nanolaser in particular, operate with subwavelength-sized cavities, such as nanowires. Also the coupling to surface plasmons of metal contacts [NEO02] modify spontaneous emission and thereby the stability character. The great challenge lies in the realization and manufacturing of room temperature nanoscale lasers. An example of a semiconductor-core embedded in a metal-shell driven by electrical injection is depicted in Fig. 1.1 [DIN13]. This device shows up narrow-banded emission lines comparable with typical semiconductor lasers and operates in continuous wave mode. The feature of operation at room temperature marks a significant progress, as metal-semiconductor nanolasers tend to above-average heat generation.

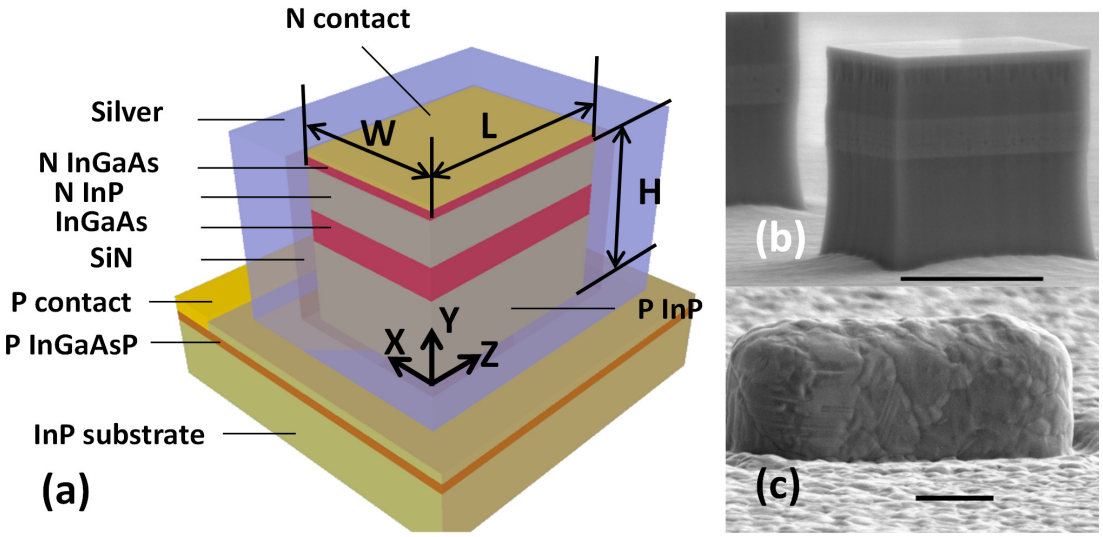

Figure 1.1: [DIN13] (a) Structure of a semiconductor nanolaser device embedded in a silver-shell-cavity. Scanning electron microscope images of the semiconductor core before (b) and after (c) coating with SiN and silver. Cavity length $L_{cav} = 1591\,\text{nm}$, quality factor $Q = 3182$.

All in all, nanolasers, compared to typical semiconductor lasers, differ in their spontaneous and stimulated emission rate, their bandwidth, their heat generation, the coupling to surface plasmons, their high quality factor (up to ten times higher and more), whereby we investigate the influence of increased spontaneous emission rates.

The complex dynamics of single mode quantum dot lasers can be grasped by the semiclassical semiconductor Bloch equations [HAK85, NIN90, NIN92]. The equivalence [HAK75] to the well-studied Lorenz equations provides a head start to modern laser theory, as complex dynamics and stability properties could be transferred to the laser equations. An established way to effectively simplify the complex Bloch equations, is the elimination of polarization dynamics, which leads directly to the classical rate equations with two, instead of three, degrees of freedom (adiabatic elimination [HAK83] - Sec. 2.2). Dynamics, stability and influence of the spontaneous emission rate on the modulability of the rate equations [CHO05, LUE09, LUE10, LIN12, GRE12a], as well as the influence of polarization on stability [WIE14] are well studied. The gap, consisting of the interaction of spontaneous emission and polarization and the effect on linear stability, shall be closed by this thesis.
On closer inspection, the title consists of three subtasks. First of all a characterization of the system's dynamics while isolating the influence of polarization and spontaneous emission, respectively. Secondly the correlation between the dynamics and the linearized rate and Bloch system within the scope of the linear stability analysis and thirdly the investigation of consequences on the small signal response.

2 Fundamentals

This chapter reviews the necessary theoretical framework to follow the thread of this thesis. The main focus is the motivation, derivation and simplification of our model. We derive the microscopic semiconductor Bloch equations for an ensemble of quantum dots and turn them into a real valued system, so we can visualize an initially complex system with three degrees of freedom in phase space. Further we proceed with the derivation of the rate equation due to adiabatic elimination of polarization dynamics. As a next step the phenomenological ingredients will be added, which includes the pump strength, losses, the Purcell factor, the β-factor, the spontaneous emission rate and the coupling to a quantum well reservoir as a wettinglayer. The final step provides an overview of the used numerical concepts and parameters.

2.1 Semiconductor Bloch equations

As a starting point we will derive the equations of motion for the polarization, electron and hole density in a semiconductor medium [CHO99]. In our approach we stay with the most important effects, which is why the dipole interactions between carriers and photons and the interaction between carriers and phonons are not taken into account. Furthermore we neglect the many-body Coulomb term of the system Hamiltonian. The Coulomb interaction term causes effects like fast equilibration into a Fermi-Dirac distribution, decay of the polarization due to Coulomb-scattering (optical dephasing) and weakening of the effective Coulomb potential due to plasma screening. Another effect included by the Coulomb term is the renormalization of the bandgap when many carriers are excited and interband attraction as well as intraband repulsion appears. These effects have influence on gain and refractive index values. Hence we restrict our semiclassical model to the description of semiconductor gain from a noninteracting electron-hole plasma in second quantization, until we proceed with further simplifications.

We begin with the Hamiltonian

$$H = H_{kin} + H_{c,pt}, \tag{2.1}$$

where H_{kin} describes the kinetic energy of the carriers and $H_{c,pt}$ the carrier-photon interaction. These two terms are given by

$$H_{kin} = \sum_{\boldsymbol{k}} (\varepsilon_{c\boldsymbol{k}} a^\dagger_{c\boldsymbol{k}} a_{c\boldsymbol{k}} + \varepsilon_{v\boldsymbol{k}} a^\dagger_{v\boldsymbol{k}} a_{v\boldsymbol{k}}), \tag{2.2}$$

$$H_{c,pt} = -V\boldsymbol{P}\cdot\boldsymbol{E} = -\sum_{\boldsymbol{k}} (\boldsymbol{\mu}_{\boldsymbol{k}} a^\dagger_{c\boldsymbol{k}} a_{v\boldsymbol{k}} + \boldsymbol{\mu}^*_{\boldsymbol{k}} a^\dagger_{v\boldsymbol{k}} a_{c\boldsymbol{k}})\boldsymbol{E}(z,t). \tag{2.3}$$

Here $\varepsilon_{c\boldsymbol{k}}$ and $\varepsilon_{v\boldsymbol{k}}$ are the electron energies in the conduction and valence band, $\boldsymbol{\mu}_{\boldsymbol{k}}$ is the complex dipole matrix element between the two bands, V is the volume of the active region, $\boldsymbol{k}$ the wavevector of the electron, $\boldsymbol{E}(z,t)$ is the electric field strength of the classical laser field and $\boldsymbol{P}$ the macroscopic polarization of the active region. The hermitian operators $a^\dagger_{c\boldsymbol{k}}$, $a_{c\boldsymbol{k}}$, $a^\dagger_{v\boldsymbol{k}}$ and $a_{v\boldsymbol{k}}$ are electron creation and annihilation operators for conduction and

valence electrons, which are fully identified by their momentum $\hbar\boldsymbol{k}$ and z-component of spin s_z with ($s_z = \pm\frac{1}{2}$). In this context we will not write the spin index s_z and the hat accent, labeling the hermitian operators, so that

$$a_{v\boldsymbol{k}} := \hat{a}_{v,\boldsymbol{k},s_z}(t), \quad \sum_{\boldsymbol{k}} := \sum_{\boldsymbol{k},s_z}.$$

First of all we switch to the electron-hole representation by using the relations

$$\begin{aligned} a^\dagger_{v\boldsymbol{k}} &= b_{-\boldsymbol{k}}, \\ a_{v\boldsymbol{k}} &= b^\dagger_{-\boldsymbol{k}}, \\ a^\dagger_{c\boldsymbol{k}} &= a^\dagger_{\boldsymbol{k}}, \\ a_{c\boldsymbol{k}} &= a_{\boldsymbol{k}}. \end{aligned} \tag{2.4}$$

This means the creation of a valence electron equals the annihilation of a hole and vice versa. Necessarily the sign of the momentum need to be switched. Thus our operators $a^\dagger_{\boldsymbol{k}}$ and $a_{\boldsymbol{k}}$ are linked to conduction electrons only. As a consequence we find the relation for the expectation value

$$\langle a^\dagger_{v\boldsymbol{k}} a_{v\boldsymbol{k}} \rangle = 1 - \langle b^\dagger_{-\boldsymbol{k}} b_{-\boldsymbol{k}} \rangle \,, \tag{2.5}$$

which means, that the probability of finding a valence electron is one minus the probability of finding a hole.

We should now take a closer look at the energies $\varepsilon_{c\boldsymbol{k}}$ and $\varepsilon_{v\boldsymbol{k}}$ in Eq. (2.2) of conduction and valence electrons, which in electron-hole representation are given by

$$\varepsilon_{c\boldsymbol{k}} = \varepsilon_{0gap} + \varepsilon_{e\boldsymbol{k}} = \varepsilon_{0gap} + \frac{\hbar^2 k^2}{2m_e}, \tag{2.6}$$

$$\varepsilon_{v\boldsymbol{k}} = \varepsilon_{h\boldsymbol{k}} = \frac{\hbar^2 k^2}{2m_h}. \tag{2.7}$$

The free energies of the charge carriers are described by $\varepsilon_{i\boldsymbol{k}}$ with ($i \in \{e, h\}$) and the bandgap energy in the absence of excited electrons is given by ε_{0gap}. The effective masses m_i are defined by

$$\frac{1}{m_i} := \frac{1}{\hbar^2} \frac{d^2 \varepsilon_{i\boldsymbol{k}}}{dk^2}\bigg|_{k=0}.$$

In conclusion the transition frequency is given by

$$\omega_{\boldsymbol{k}} = \frac{1}{\hbar}(\varepsilon_{h\boldsymbol{k}} + \varepsilon_{0gap} + \varepsilon_{e\boldsymbol{k}}). \tag{2.8}$$

Inserting Eqs. (2.4), (2.6) and (2.7) in our Hamiltonian from Eq. (2.1), leads us to

$$H = \sum_{\boldsymbol{k}} ((\varepsilon_{0gap} + \varepsilon_{e\boldsymbol{k}}) a^\dagger_{\boldsymbol{k}} a_{\boldsymbol{k}} + \varepsilon_{h\boldsymbol{k}} b^\dagger_{-\boldsymbol{k}} b_{-\boldsymbol{k}}) - \sum_{\boldsymbol{k}} (\boldsymbol{\mu}_{\boldsymbol{k}} a^\dagger_{\boldsymbol{k}} b^\dagger_{-\boldsymbol{k}} + \boldsymbol{\mu}^*_{\boldsymbol{k}} b_{-\boldsymbol{k}} a_{\boldsymbol{k}}) \boldsymbol{E}(z,t). \tag{2.9}$$

As we have time-dependent operators (but not explicit time-dependent) and constant state vectors, we can calculate our system dynamics by using the Heisenberg equation for expectation values

$$\frac{d}{dt} \langle O \rangle = \frac{\mathrm{i}}{\hbar} \langle [H, O] \rangle$$

without the partial derivative. Our fermionic particle operators obey the anticommutation relations

$$\begin{aligned} [a_{\boldsymbol{k}}, a_{\boldsymbol{k}'}]_+ &= [a^\dagger_{\boldsymbol{k}}, a^\dagger_{\boldsymbol{k}'}]_+ = 0, \\ [a_{\boldsymbol{k}}, a^\dagger_{\boldsymbol{k}'}]_+ &= \delta_{\boldsymbol{k},\boldsymbol{k}'}, \end{aligned} \tag{2.10}$$

also true for hole creator and annihilator $b^\dagger_{-\boldsymbol{k}}$ and $b_{-\boldsymbol{k}}$. Electron and hole operators commutate with each other. Considering that Eq. (2.9) can be written as

$$H = \sum_{\boldsymbol{k}} H_{\boldsymbol{k}},$$

we can calculate equations of motion for one particular atom with its momentum ($\hbar\boldsymbol{k}$). Thus we use

$$\frac{d}{dt}\langle O_{\boldsymbol{k}}\rangle = \frac{\mathrm{i}}{\hbar}\langle [H_{\boldsymbol{k}}, O_{\boldsymbol{k}}]\rangle .$$

Now we can determine the dynamics of the occupation probability for electrons $\varrho^e_{\boldsymbol{k}}$ and holes $\varrho^h_{\boldsymbol{k}}$, as well as the polarization $p_{\boldsymbol{k}}$, by making use of the anticommutation relations (2.10) and the transition frequency from Eq. (2.8). As a final step we introduce the expressions

$$\begin{aligned} \varrho^e_{\boldsymbol{k}} &= \langle a^\dagger_{\boldsymbol{k}} a_{\boldsymbol{k}}\rangle , \\ \varrho^h_{\boldsymbol{k}} &= \langle b^\dagger_{-\boldsymbol{k}} b_{-\boldsymbol{k}}\rangle , \\ p_{\boldsymbol{k}} &= \langle b_{-\boldsymbol{k}} a_{\boldsymbol{k}}\rangle \end{aligned}$$

for the quantities mentioned above. This leads us to the semiconductor Bloch equations

$$\frac{d}{dt}\varrho^e_{\boldsymbol{k}} = \frac{d}{dt}\varrho^h_{\boldsymbol{k}} = \frac{\mathrm{i}}{\hbar}\boldsymbol{E}(z,t)(\boldsymbol{\mu}_{\boldsymbol{k}} p^*_{\boldsymbol{k}} - \boldsymbol{\mu}^*_{\boldsymbol{k}} p_{\boldsymbol{k}}), \tag{2.11}$$

$$\frac{d}{dt}p_{\boldsymbol{k}} = -\mathrm{i}\omega_{\boldsymbol{k}} p_{\boldsymbol{k}} - \frac{\mathrm{i}}{\hbar}\mu_{\boldsymbol{k}}\boldsymbol{E}(z,t)(\varrho^e_{\boldsymbol{k}} + \varrho^h_{\boldsymbol{k}} - 1), \tag{2.12}$$

where we can identify the Rabi frequency

$$\Omega_{\boldsymbol{k}}(z,t) = \frac{\boldsymbol{\mu}_{\boldsymbol{k}} \cdot \boldsymbol{E}(z,t)}{\hbar}.$$

The expression in the last bracket of the polarization Eq. (2.12) describes the inversion of the atom with the momentum mode $\hbar\boldsymbol{k}$, given by

$$\begin{aligned} d_{\boldsymbol{k}} &= \langle a^\dagger_{c\boldsymbol{k}} a_{c\boldsymbol{k}}\rangle - \langle a^\dagger_{v\boldsymbol{k}} a_{v\boldsymbol{k}}\rangle \\ &= \langle a^\dagger_{\boldsymbol{k}} a_{\boldsymbol{k}}\rangle + \langle b^\dagger_{-\boldsymbol{k}} b^\dagger_{-\boldsymbol{k}}\rangle - 1 \\ &= \varrho^e_{\boldsymbol{k}} + \varrho^h_{\boldsymbol{k}} - 1. \end{aligned} \tag{2.13}$$

Here we used Eq. (2.5). Accordingly we can write the Eqs. (2.11) and (2.12) as

$$\frac{d}{dt}d_{\boldsymbol{k}} = \frac{2\mathrm{i}}{\hbar}\boldsymbol{E}(z,t)(\boldsymbol{\mu}_{\boldsymbol{k}} p^*_{\boldsymbol{k}} - \boldsymbol{\mu}^*_{\boldsymbol{k}} p_{\boldsymbol{k}}), \tag{2.14}$$

$$\frac{d}{dt}p_{\boldsymbol{k}} = -\mathrm{i}\omega_{\boldsymbol{k}} p_{\boldsymbol{k}} - \frac{\mathrm{i}}{\hbar}\mu_{\boldsymbol{k}}\boldsymbol{E}(z,t) d_{\boldsymbol{k}}, \tag{2.15}$$

which will be used in the following. Further phenomenological amendments have to be made, as this is necessary for simulating losses and pump processes. We introduce in Eq. (2.14) a pump parameter d_0, damped by the reciprocal lifetime of inversion T_1^{-1}, and add a term for non-radiative relaxation $d_{\boldsymbol{k}}/T_1$. In Eq. (2.15) we add a damping factor γ for the decay of polarization (dephasing) due to collisions (carrier-carrier scattering). This leads us to the fundamental equations of the semiclassical laser theory for semiconductors

$$\frac{d}{dt}d_{\boldsymbol{k}} = \frac{2\mathrm{i}}{\hbar}\boldsymbol{E}(z,t)(\boldsymbol{\mu}_{\boldsymbol{k}}p_{\boldsymbol{k}}^* - \boldsymbol{\mu}_{\boldsymbol{k}}^* p_{\boldsymbol{k}}) + \frac{d_0 - d_{\boldsymbol{k}}}{T_1}, \tag{2.16}$$

$$\frac{d}{dt}p_{\boldsymbol{k}} = -(\mathrm{i}\omega_{\boldsymbol{k}} + \gamma)p_{\boldsymbol{k}} - \frac{\mathrm{i}}{\hbar}\mu_{\boldsymbol{k}}\boldsymbol{E}(z,t)d_{\boldsymbol{k}}. \tag{2.17}$$

The Eqs. (2.16) and (2.17) contain the undetermined macroscopic electric field strength $\boldsymbol{E}(z,t)$. In order to close this set of equations we will derive the wave equation for the microscopic electric field in section 2.1.2. Since the Eqs. (2.16) and (2.17) are already a good way to describe fundamental laser processes, we will spend an separate subsection for the approximations we make, to receive our simplified microscopic set of equations for resonant systems.

2.1.1 Approximations of the Bloch equations

The first step is to put the electric field ansatz (2.23) into the inversion Eq. (2.16), hence we get

$$\dot{d}_{\boldsymbol{k}} = \frac{2\mathrm{i}}{\hbar}\sum_\lambda \mathrm{i}\boldsymbol{u}_\lambda(\boldsymbol{r})\varepsilon_\lambda(\bar{c}_\lambda e^{-\mathrm{i}\omega_\lambda t} - \bar{c}_\lambda e^{\mathrm{i}\omega_\lambda t})(\boldsymbol{\mu}_{\boldsymbol{k}}\bar{p}_{\boldsymbol{k}}^* e^{\mathrm{i}\omega_{\boldsymbol{k}}t} - \boldsymbol{\mu}_{\boldsymbol{k}}^*\bar{p}_{\boldsymbol{k}}e^{-\mathrm{i}\omega_{\boldsymbol{k}}t}) + \frac{d_0 - d_{\boldsymbol{k}}}{T_1}. \tag{2.18}$$

Here the microscopic polarization $p_{\boldsymbol{k}}$ and $p_{\boldsymbol{k}}^*$ has already been split into a slowly and fast varying part. Now we are able to proceed with the well-founded *rotating wave approximation* (RWA). As far as we consider a low energy system in resonance we can neglect the fast varying terms, which are proportional to $e^{\pm i(\omega_\lambda + \omega_{\boldsymbol{k}})t}$, and keep the slowly varying terms, which contain $e^{\pm i(\omega_\lambda - \omega_{\boldsymbol{k}})t} \approx 1$.
We receive

$$\dot{d}_{\boldsymbol{k}} = \frac{2\mathrm{i}}{\hbar}\sum_\lambda \mathrm{i}\boldsymbol{u}_\lambda(\boldsymbol{r})\varepsilon_\lambda(\boldsymbol{\mu}_{\boldsymbol{k}}\bar{c}_\lambda\bar{p}_{\boldsymbol{k}}^* + \boldsymbol{\mu}_{\boldsymbol{k}}^*\bar{c}_\lambda^*\bar{p}_{\boldsymbol{k}}) + \frac{d_0 - d_{\boldsymbol{k}}}{T_1}$$

and we can simplify this expression by summarizing the constants and introducing a space saving quantity

$$g_{\lambda,\boldsymbol{k}} := -\mathrm{i}\boldsymbol{\mu}_{\boldsymbol{k}}\boldsymbol{u}_\lambda(\boldsymbol{r})\sqrt{\frac{\omega_\lambda}{\hbar 2\varepsilon_0}}. \tag{2.19}$$

This quantity is called *coupling constant*, as it has field and matter properties. Note that for the imaginary dipole matrix element the expression ($\boldsymbol{\mu}_{\boldsymbol{k}} = -\boldsymbol{\mu}_{\boldsymbol{k}}^*$) holds. We finally get our approximated inversion equation for multiple wavemodes λ

$$\dot{d}_{\boldsymbol{k}} = 2\mathrm{i}\sum_\lambda (g_{\lambda,\boldsymbol{k}}^*\bar{c}_\lambda^*\bar{p}_k - g_{\lambda,\boldsymbol{k}}\bar{c}_\lambda\bar{p}_{\boldsymbol{k}}^*) + \frac{d_0 - d_{\boldsymbol{k}}}{T_1}, \tag{2.20}$$

now only depending on microscopic quantities.
Let us now turn toward the polarization Eq. (2.17). Multiplying by $\bar{p}^*_{\boldsymbol{k}} e^{i\omega_{\boldsymbol{k}} t}$ gives us

$$\bar{p}^*_{\boldsymbol{k}}\dot{\bar{p}}_{\boldsymbol{k}} - \mathrm{i}\omega_{\boldsymbol{k}}\bar{p}^*_{\boldsymbol{k}}\bar{p}_{\boldsymbol{k}} = -(\mathrm{i}\omega_{\boldsymbol{k}} + \gamma)\bar{p}^*_{\boldsymbol{k}}\bar{p}_{\boldsymbol{k}} - \frac{\mathrm{i}}{\hbar}\boldsymbol{\mu}_{\boldsymbol{k}} \sum_{\lambda} \mathrm{i}\boldsymbol{u}_\lambda(\boldsymbol{r})\varepsilon_\lambda(\bar{p}^*_{\boldsymbol{k}}\bar{c}_\lambda - \bar{p}^*_{\boldsymbol{k}}\bar{c}^*_\lambda e^{\mathrm{i}(\omega_{\boldsymbol{k}}+\omega_\lambda)t})d_{\boldsymbol{k}}.$$

Neglecting the fast varying term, dividing by $\bar{p}^*_{\boldsymbol{k}}$ and substituting Eq. (2.19) in the previous equation, leads us to the final multiple mode semiconductor Bloch equations

$$\dot{d}_{\boldsymbol{k}} = 2i\sum_{\lambda}(g^*_{\lambda,\boldsymbol{k}}c^*_\lambda p_{\boldsymbol{k}} - g_{\lambda,\boldsymbol{k}}c_\lambda p^*_{\boldsymbol{k}}) + \frac{d_0 - d_{\boldsymbol{k}}}{T_1}, \tag{2.21}$$

$$\dot{p}_{\boldsymbol{k}} = -\gamma p_{\boldsymbol{k}} + \mathrm{i}\sum_{\lambda} g_{\lambda,\boldsymbol{k}}c_\lambda d_{\boldsymbol{k}}, \tag{2.22}$$

where the label for slowly varying quantities is not considered any more, as we stay in the rotating frame picture.

2.1.2 Microscopic wave equation

The quantum-mechanical ansatz [CHO99] commonly made for the electric field is

$$\boldsymbol{E}(z,t) = \mathrm{i}\sum_{\boldsymbol{k}_\lambda,p_\lambda}\sqrt{\frac{\hbar\omega_{\boldsymbol{\lambda}}}{2\varepsilon_0\varepsilon_r V_{cav}}}\boldsymbol{e}_{\boldsymbol{\lambda},p_\lambda}e^{\mathrm{i}\boldsymbol{k}_\lambda\cdot\boldsymbol{r}}\bar{c}_{\boldsymbol{\lambda},p_\lambda}(t)e^{-\mathrm{i}\omega_{\boldsymbol{\lambda}}t} + c.c., \tag{2.23}$$

where the index p_λ represents the polarization directions, which accordingly to the spin direction s_z will not be mentioned furthermore, $\boldsymbol{e}_{\boldsymbol{\lambda},p_\lambda}$ a normalized vector indicating the polarization of the light field, V_{cav} the cavity volume, $\bar{c}_{\boldsymbol{\lambda},p_\lambda}(t)$ the slowly varying and dimensionless amplitude function and the factor

$$\varepsilon_{\boldsymbol{\lambda}} := \sqrt{\frac{\hbar\omega_{\boldsymbol{\lambda}}}{2\varepsilon_0\varepsilon_r}}$$

the vacuum field amplitude with the dimension of the electric field strength. In this context we will not write the polarization index and p_λ and the hat accent, labeling the hermitian operators, so that

$$c_{\boldsymbol{\lambda}} := \hat{\bar{c}}_{\boldsymbol{\lambda},p_\lambda}(t), \quad \sum_{\boldsymbol{k}_\lambda} := \sum_{\boldsymbol{k}_\lambda,p_\lambda}.$$

All space dependencies can be summarized by a quantity

$$\boldsymbol{u}_\lambda(\boldsymbol{r}) = \frac{1}{\sqrt{V_{cav}}}\boldsymbol{e}_\lambda e^{\mathrm{i}\boldsymbol{k}_\lambda\cdot\boldsymbol{r}}.$$

The wave equation for the electric field can simply be derived from the macroscopic Maxwell equations [MAX65]

$$\begin{aligned} \nabla\times\boldsymbol{E} &= -\dot{\boldsymbol{B}}, \\ \nabla\times\boldsymbol{H} &= \boldsymbol{j}_f + \dot{\boldsymbol{D}}, \\ \nabla\cdot\boldsymbol{B} &= 0, \\ \nabla\cdot\boldsymbol{D} &= \rho_f, \end{aligned} \tag{2.24}$$

where $\boldsymbol{D}$ is the electric displacement field, $\boldsymbol{j}_f$ and ρ_f the current density and charge density induced by free charge carriers, $\boldsymbol{H}$ the magnetic field strength and $\boldsymbol{B}$ the magnetic flux density. The quantities $\boldsymbol{D}$ and $\boldsymbol{H}$ are given by the constitutive equations of electromagnetism

$$\begin{aligned} \boldsymbol{D} &= \varepsilon_0 \boldsymbol{E} + \boldsymbol{P}, \\ \boldsymbol{H} &= \frac{1}{\mu_0}\boldsymbol{B} - \boldsymbol{M}, \end{aligned}$$

where $\boldsymbol{P}$ and $\boldsymbol{M}$ are the macroscopic polarization and magnetization of the medium. We make use of the simplified Ohm's law

$$\boldsymbol{j}_f = \sigma \boldsymbol{E}$$

for isotropic media with the electrical conductivity σ and consider a non-magnetic medium with $\boldsymbol{M} = 0$ in the absence of electrical charges, so that $\rho_f = 0$. We now determine the rotation of Eq. (2.24)

$$-\underbrace{\nabla \times (\nabla \times \boldsymbol{E})}_{\nabla(\nabla\cdot\boldsymbol{E})-\Delta\boldsymbol{E}} = \nabla \times \dot{\boldsymbol{B}} = \mu_0 \dot{\boldsymbol{j}}_f + \varepsilon_0\mu_0 \ddot{\boldsymbol{E}} + \mu_0 \ddot{\boldsymbol{P}},$$

assuming that light field vectors vary only little in the direction they point ($\nabla \cdot \boldsymbol{E} = 0$), especially true for plane waves, and get the macroscopic wave equation

$$\Delta \boldsymbol{E} - \frac{1}{c^2}\ddot{\boldsymbol{E}} - \mu_0 \sigma \dot{\boldsymbol{E}} = \mu_0 \ddot{\boldsymbol{P}} \tag{2.25}$$

for the electric field. The speed of light in vacuum is given by ($c = 1/\sqrt{\varepsilon_0\mu_0}$). This equation is for $\ddot{\boldsymbol{P}} = 0$ identical to the Telegrapher's equation for wave propagation in conducting media. In this case the electric field is driven by the electric polarization of the medium, its source term.

The next step is to derive a wave equation which exclusively contains dependencies of microscopic quantities like c_λ and $p_{\boldsymbol{k}}$. We multiply Eq. (2.25) by $(-c^2)$ and consider ($\Delta \boldsymbol{E} = -k^2 \boldsymbol{E}$), thus we get

$$\omega_\lambda^2 \boldsymbol{E} + \ddot{\boldsymbol{E}} + \frac{\sigma}{\varepsilon_0}\dot{\boldsymbol{E}} = -\frac{1}{\varepsilon_0}\ddot{\boldsymbol{P}}.$$

The polarization $\boldsymbol{P}$ and the electric field $\boldsymbol{E}$ can be written in spectral representation as

$$\boldsymbol{E} = \sum_{\lambda'} \boldsymbol{u}_{\lambda'}(\boldsymbol{r}) E_{\lambda'}(t), \qquad \boldsymbol{P} = \sum_{\lambda'} \boldsymbol{u}_{\lambda'}(\boldsymbol{r}) P_{\lambda'}(t), \qquad (\omega_{\boldsymbol{k}} \approx \omega_\lambda),$$

whereas all space dependencies are taken out of P_λ and E_λ. In order to eliminate the space dependencies in the previous equation, we need to project $\boldsymbol{E}$ and $\boldsymbol{P}$ on a single mode, thus we multiply by $\boldsymbol{u}_\lambda(\boldsymbol{r})$ and integrate over all space directions

$$\omega_\lambda^2 E_\lambda + \ddot{E}_\lambda + \frac{1}{\varepsilon_0}\sum_{\lambda'} \underbrace{\int \boldsymbol{u}_\lambda \sigma \boldsymbol{u}_{\lambda'} d^3r}_{\sigma_{\lambda,\lambda'}=\delta_{\lambda,\lambda'}\sigma_\lambda} \dot{E}_{\lambda'} = -\frac{1}{\varepsilon_0}\sum_{\lambda'} \ddot{P}_{\lambda'} \underbrace{\int \boldsymbol{u}_\lambda(\boldsymbol{r}) \boldsymbol{u}_{\lambda'}(\boldsymbol{r}) d^3r}_{\delta_{\lambda,\lambda'}} = -\frac{\ddot{P}_\lambda}{\varepsilon_0}. \tag{2.26}$$

Simplified Eq. (2.26) looks like

$$\omega_\lambda^2 E_\lambda + \ddot{E}_\lambda + \frac{\sigma}{\varepsilon_0}\dot{E}_\lambda = -\frac{1}{\varepsilon_0}\ddot{P}_\lambda. \tag{2.27}$$

In the following we will perform the *slowly varying envelope approximation* (SVEA) and the transformation into the rotating frame. Let us start with the *SVEA*.
We can split the electric field projection in a slowly varying envelope and a fast oscillating part

$$E_\lambda^\pm(t) = \bar{E}_\lambda(t) e^{\mp \mathrm{i}\omega_\lambda t}. \tag{2.28}$$

While calculating the derivatives of the electric field, we assume that the envelope of the travelling wave varies slowly in space and time compared to the wavelength

$$\left|\dot{\bar{E}}_\lambda\right| \ll \left|\omega_\lambda \bar{E}_\lambda\right|, \qquad \left|\ddot{\bar{E}}_\lambda\right| \ll \left|\omega_\lambda \dot{\bar{E}}_\lambda\right|.$$

This is only true for narrow-banded spectra, which means the spectral width of a pulse has to be much smaller than its carrier frequency. Hence this approximation cancels out our second time derivative of the electric field. Remember that the electric field and the polarization is the sum of a normal (+) and a complex conjugated (−) part, respectively. Using

$$P_\lambda = P_\lambda^+ + P_\lambda^-, \qquad \ddot{P}_\lambda^+ = -\omega_\lambda^2 P_\lambda^+ = \omega_\lambda^2 \sum_{\boldsymbol{k}} \boldsymbol{u}_\lambda(\boldsymbol{r}) \boldsymbol{\mu}_{\boldsymbol{k}} p_{\boldsymbol{k}}$$

and by introducing the photon damping constant ($\kappa = \sigma/2\varepsilon_0$) describing optical losses, we find after a few steps (Appendix A.1)

$$\dot{E}_\lambda^\pm = (\mp \mathrm{i}\omega_\lambda - \kappa) E_\lambda^\pm \pm \frac{\mathrm{i}}{2\varepsilon_0}\omega_\lambda P_\lambda^\pm. \tag{2.29}$$

Accordingly to the procedure from Eq. (2.18) to (2.20), we receive our microscopic wave equation

$$\dot{c}_\lambda = (-\mathrm{i}\omega_\lambda - \kappa) c_\lambda - \mathrm{i} \sum_{\boldsymbol{k}} g_{\lambda,\boldsymbol{k}}^* p_{\boldsymbol{k}}$$

for multiple wavemodes. Moving to the rotating frame we find

$$\dot{\bar{c}}_\lambda = -\kappa \bar{c}_\lambda - \mathrm{i} \sum_{\boldsymbol{k}} g_{\lambda,\boldsymbol{k}}^* \bar{p}_{\boldsymbol{k}}, \tag{2.30}$$

which is now our desired wave equation to close the set of Bloch equations. Slowly oscillating quantities will not be labeled in the following.

2.1.3 Simplifications

The following steps are to decrease the number of differential equations, as we have an arbitrary number by now. The first simplification we make is the switchover to a resonant driven two-level system. Therefore we take the Eqs (2.30), (2.22) and (2.21) and cancel the sum over the wavemodes λ and polarization directions p_λ and replace the sum over the electron momentums $\hbar\boldsymbol{k}$ and the z-component of their spin s_z with the factor $(2Z^{QD}\Gamma)$,

which represents the number of quantum dots multiplied with the spin degeneracy and the confinement factor Γ. This factor represents the fraction of the quantum dots within the mode volume, which are contributing to the laser emission. It is measure of the fraction of the active region that amplifies a given mode. This fraction depends on the modevolume and is therefore an uncomplicated way to obtain the modal gain of a device. As we consider a single mode laser the confinement factor reduces to a constant. The coupling constant g can be set real, which is explained below. We get a system of five differential equations

$$\dot{c} = -\kappa c - 2\mathrm{i}Z^{QD}\Gamma|g|p, \tag{2.31}$$

$$\dot{p} = -\gamma p + \mathrm{i}|g|cd, \tag{2.32}$$

$$\dot{d} = 2\mathrm{i}(|g|c^*p - |g|cp^*) + \frac{d_0 - d}{T_1}, \tag{2.33}$$

where c and p are complex quantities and there is a complex conjugated equation for each. The inversion is real. We have now averaged microscopic equations, which describe the whole medium, because the behaviour of all atoms in the medium is approximately identical due to the spatially uniform lattice structure in semiconductors. The photon equation has now averaged information of all quantum dots in the system.
The system can be even more simplified if we make a further assumption. Our coupling constant g (Eq. (2.19)) is complex. The phase factor $e^{\mathrm{i}\boldsymbol{k}\cdot\boldsymbol{r}}$ in the coupling constant g has no effect on system dynamics and can be omitted. We see in the equations above, if g is set real, the polarization p stays imaginary and the field amplitude function c stays real. The complex dynamic of the variables c and p becomes one dimensional in the complex plane without any loss of information. Formally we say

$$\begin{gathered} c = \tilde{c}, \\ p = \mathrm{i}\tilde{p}, \\ g \to |g| = \mu_{12}\sqrt{\tfrac{\omega_\lambda}{\hbar 2\varepsilon_0 V_{cav}}}, \\ \tilde{c}, \tilde{p}, |g| \in \mathbb{R}. \end{gathered}$$

The precondition to this ansatz is obviously to choose real initial values of $\tilde{c}$ and $\tilde{p}$ (the imaginary part is real valued). Putting these relations in Eq. (2.31), (2.32) and (2.33) we receive a system of three real valued Bloch equations

$$\dot{\tilde{c}} = -\kappa\tilde{c} + 2Z^{QD}\Gamma|g|\tilde{p}, \tag{2.34}$$

$$\dot{\tilde{p}} = -\gamma\tilde{p} + |g|\tilde{c}d, \tag{2.35}$$

$$\dot{d} = -4|g|\tilde{c}\tilde{p} + \frac{d_0 - d}{T_1}. \tag{2.36}$$

As a matter of clarity we will not explicitely mark the real quantities with a tilde. This system is a good starting point for numerical calculations.

2.2 Rate equation approximation

This subsection deals with the conversion of the Bloch equations to the well known rate equations. While the Bloch equations are derived by fundamental principles of electrodynamics, the rate equations are heuristically motivated. Nevertheless the rate equations are

a special case of the Bloch equations. If one assumes a very fast settling time of polarization, the polarization dynamics can be neglected. In other words the change of polarization is so fast, that the development of all other dynamic variables stays unaffected. In that sense the rate equation approximation is also called *adiabatic limit*. In order to transform our assumption into mathematics, we take Eq. (2.22) and write

$$\dot{p} = 0 \qquad \rightarrow \qquad p = \frac{g}{\gamma} cd.$$

Putting this result in the Eqs. (2.34) and (2.36), we receive the system of rate equations

$$\dot{c} = -\kappa c + \frac{2Z^{QD}\Gamma g^2}{\gamma} cd, \tag{2.37}$$

$$\dot{d} = -\frac{4g^2}{\gamma} c^2 d + \frac{d_0 - d}{T_1}. \tag{2.38}$$

The terms which couple these two equations are describing the part of stimulated processes, respectively. The semiconductor gain is defined as

$$G := 2Z^{QD}\Gamma \frac{g^2}{\gamma c_n} \tag{2.39}$$

and has the dimension of $[\mathrm{cm}^{-1}]$. The speed of light inside the laser medium is given by ($c_n = c_0/n$) with the refractive index n. The comparison between a system with and without polarization dynamics is an essential part of this thesis.
It is more usual to describe the dynamics of the photon number instead of the field amplitude. The correct transformation between those two quantities will be derived explicitely below. We say the photon number is proportional to the absolute square of the field amplitude, so that

$$\begin{aligned} N_{ph} &= \xi |c|^2 \\ \rightarrow \dot{N}_{ph} &= \xi \cdot 2|c| \underbrace{\partial_t |c|}_{\dot{c}|_{stim}} \\ &= \xi \cdot \frac{4Z^{QD}\Gamma g^2}{\gamma} c^2 d, \end{aligned} \tag{2.40}$$

where $\dot{c}|_{stim}$ is given by the last term of Eq. (2.37). Considering Eq. (2.13) we know, if a photon is emitted, the inversion decreases with

$$\dot{N}_{ph} \stackrel{!}{=} -\sum_{\boldsymbol{k}} \frac{1}{2} \dot{d}_{\boldsymbol{k}}|_{stim} = -Z^{QD}\Gamma \dot{d}|_{stim}$$

By putting the factor $\dot{d}|_{stim}$ of Eq. (2.38) in the equation above, we find that the last relation equals Eq. (2.40). Obviously our constant of proportionality ξ equals one so we can write

$$N_{ph} = |c|^2 \quad \leftrightarrow \quad \dot{c} = \frac{\dot{N}_{ph}}{2|c|}. \tag{2.41}$$

The resulting rate equation system is then given by

$$\dot{N}_{ph} = -2\kappa N_{ph} + \frac{4Z^{QD}\Gamma g^2}{\gamma} d N_{ph}, \tag{2.42}$$

$$\dot{d} = -\frac{4g^2}{\gamma} N_{ph} d + \frac{d_0 - d}{T_1}. \tag{2.43}$$

The rate equation approximation is a prime example of adiabatic elimination [HAK83]. It says that the global system dynamics is determined by the values of its timescales and may be reduced to a subsystem with reduced degrees of freedom, which is still able to grasp the full dynamics within the framework of the chosen timescales. In this case the emerged subsystem consists of the photon amplitude and inversion dynamic and submits the polarization dynamic, which hence is adiabatic eliminated due to its much faster decay.

2.3 Wettinglayer and scattering rates

The aim is to change to a more realistic quantum dot laser model without increasing the complexity of our equation systems. Until this point we simulate electrical pumping due to direct manipulation of inversion with a constant factor d_0. This factor must be chosen between ± 1, as this is the maximum or minimum inversion. The problem is that one can not know which pump current corresponds to this quantity, whereas the pump current is an important and basic parameter in experiments. In addition it is desirable to have a pump current which can be arbitrarily increased, as long as a saturation of charge carriers takes place. To achieve this we need to introduce an additional wettinglayer which can be arbitrarily pumped and from where charge carriers scatter into the quantum dots. These quantum dots are grown directly onto the wettinglayer as seen in Fig. 2.1. This thin layer is a two-dimensional electron reservoir, coupled to the zero-dimensional quantum dots and behaves like a quantum well so charge carriers can be regarded fully quantized. The

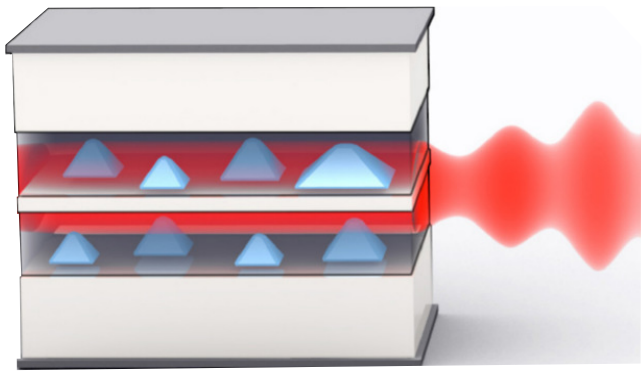

Figure 2.1: [LUE13] Scheme of a quantum dot laser with quantum dots (light blue pyramids), wettinglayer (dark grey layer below the quantum dots) and bulk material (light grey area below the wettinglayer).

actual photon emission comes from the quantum dots. We refer the implementation of the

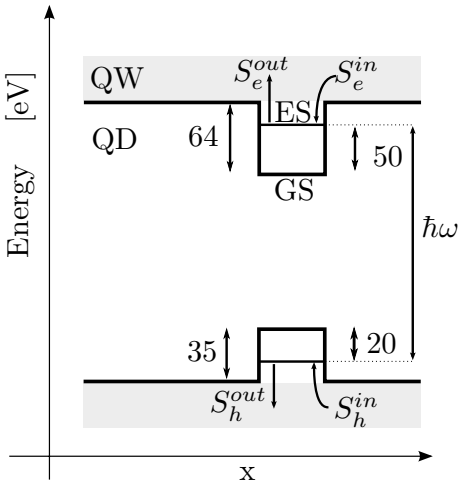

Figure 2.2: Band diagram of a laser device [LUE11a] with quantum dots (QD) embedded in a quantum well (QW). The transition energies between ground state (GS) and excited state (ES) of electron and holes and between ground state and wettinglayer-escape, respectively, are marked.

scattering rates to the well proved rate equations model in [LUE13]. Here the dynamic of the inversion is assumed as

$$\begin{aligned}\dot{d} &= \dot{\varrho}_e + \dot{\varrho}_h \\ &= -\frac{4g^2}{\gamma}c^2 d \\ &\quad +S_e^{in}(w_e, w_h)(1-\varrho_e) - S_e^{out}(w_e, w_h)\varrho_e \\ &\quad +S_h^{in}(w_e, w_h)(1-\varrho_h) - S_h^{out}(w_e, w_h)\varrho_h,\end{aligned}$$

where w_e and w_h are the electron and hole densities in the wettinglayer, respectively, S_e^{in}, S_e^{out} and S_h^{in}, S_h^{out} are the in- and out-scattering rates for electrons and holes between the quantum dots and the wettinglayer. We do not consider the dynamics of the wettinglayer, as we assume a large reservoir with a constant supply of charge carriers. Furthermore we equalize electron and hole densities in the quantum dots $\varrho_e = \varrho_h$ and wettinglayer $w_e = w_h$ so that the scattering rates between them are equal for electrons and holes

$$S^{in} = S_e^{in}(w_e) = S_h^{in}(w_e), \quad S^{out} = S_e^{out}(w_e) = S_h^{out}(w_e).$$

This step simplifies our equations noticably, as we do not have to consider the dynamics of holes and electrons separately. In order to fit our model to this ansatz, we compare the last equation with Eq. (2.38)

$$\begin{aligned}\dot{d} &= -\frac{4g^2}{\gamma}c^2 d + 2S^{in} - \left(S^{in} + S^{out}\right)(d+1) \\ &\stackrel{!}{=} -\frac{4g^2}{\gamma}c^2 d + \frac{d_0 - d}{T_1}.\end{aligned}$$

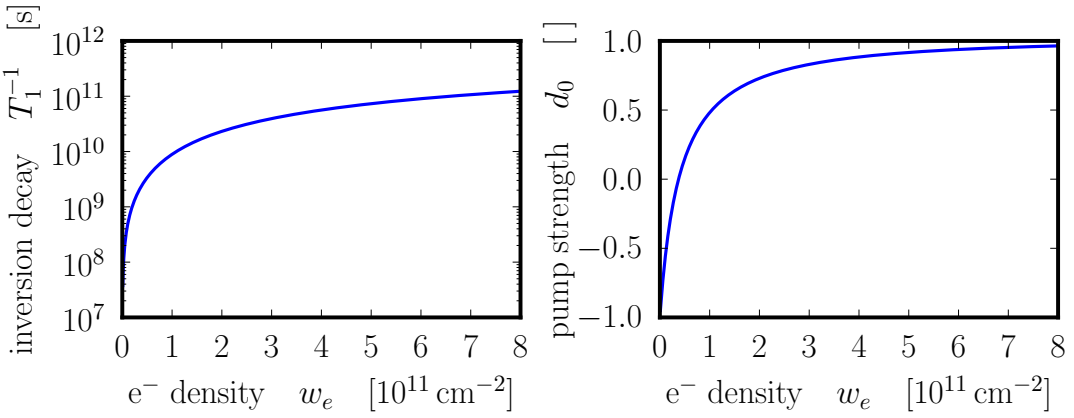

Figure 2.3: Inversion decay $T_1^{-1}(w_e)$ and pump strength $d_0(w_e)$ versus the electron density w_e in the wettinglayer.

This equation is fulfilled, if we set

$$\begin{aligned} T_1 \quad \rightarrow \quad T_1(w_e) \quad &= \quad \left(S^{in} + S^{out}\right)^{-1} \cdot 10^{-12}, \\ d_0 \quad \rightarrow \quad d_0(w_e) \quad &= \quad \frac{2S^{in}}{S^{in} + S^{out}} - 1. \end{aligned}$$

These scattering rates characterize our timescale of inversion lifetime T_1 and pump strength d_0 and give them a new dependency of the charge carrier density w_e in the wettinglayer. The detailed scattering rates, which are used in calculations of this thesis are found in the experiment described in [LUE11a] and were fitted by

$$\begin{aligned} S^{in}(w_e) \quad &= \quad \frac{0,00904605 w_e^2 \cdot e^{0,0001882 w_e}}{0,956096 + 0,406254 w_e + 0,00925689 w_e^2}, \\ S^{out}(w_e) \quad &= \quad \frac{0,084133}{e^{0,215347 w_e} - 1} S^{in}(w_e). \end{aligned}$$

The full scattering rates can be found in the Appendix A.2. The device used in this experiment follows the energy scheme of Fig. 2.2. The new behaviour of the inversion lifetime $T_1(w_e)$ and the pump strength $d_0(w_e)$ is depicted in Fig. 2.3. We can see that the lifetime T_1 of inversion shortens with increasing the electron density in the wettinglayer w_e. The inversion decay becomes fast when in-scattering rates increase, until the in-scattered carriers cannot accelerate the inversion decay any more, as a supremum for the net pump strength d_0 exists.

2.4 Purcell effect

The Purcell effect indicates the phenomenon of altering the photonic density of states due to cavity properties, which entails the modification of the spontaneous and stimulated emission rate. Our focus lies on the effect of spontaneous emission. We basically investigate the ratio of the Einstein coefficient of spontaneous emission in a cavity and the coefficient

in vacuum

$$F_P := \frac{\Gamma_{cav}}{\Gamma_{vac}}, \tag{2.44}$$

which is known as the Purcell factor. We receive the Einstein coefficient of spontaneous emission in vacuum by using Fermi's golden rule

$$W_{1\to 2} = \Gamma_{vac} = \frac{1}{3\hbar}\frac{2\pi}{\hbar}\left|\langle 1|H_{c,pt}|2\rangle\right|^2 D_{vac}(\omega_{\boldsymbol{\lambda}}). \tag{2.45}$$

The first fraction appears due to averaging over the three space dimensions. The interaction Hamiltonian can be written as

$$H_{c,pt} = -e_0 \boldsymbol{r}\cdot\boldsymbol{E}, \tag{2.46}$$

where e_0 is the elementary charge. This Hamiltonian is equivalent to Eq. (2.3), but reduced to one mode. The ansatz for the electric field is given by Eq. (2.23) on page 7. Inserting the Eqs. (2.46) and (2.23) in Eq. (2.45), we find

$$\begin{aligned}
\Gamma_{vac} &= \frac{2\pi}{3\hbar^2}|\underbrace{\langle 1| - e_0\boldsymbol{r}|2\rangle}_{\boldsymbol{\mu_k}}\boldsymbol{E}|^2 D_{vac}(\omega_{\boldsymbol{\lambda}}) \\
&= \frac{2\pi}{3\hbar^2}\cdot\frac{\mu_{\boldsymbol{k}}^2\varepsilon_{\boldsymbol{\lambda}}^2}{V_{cav}} D_{vac}(\omega_{\boldsymbol{\lambda}}) \\
&= \frac{\mu_{\boldsymbol{k}}^2\omega_{\boldsymbol{\lambda}}\pi}{3\varepsilon_0\varepsilon_r\hbar V_{cav}} D_{vac}(\omega_{\boldsymbol{\lambda}}).
\end{aligned} \tag{2.47}$$

The next step is to calculate the photonic density of states in vacuum $D_{vac}(\omega_{\boldsymbol{\lambda}})$. Thus we first calculate the number of states

$$\sum_{\boldsymbol{k}_\lambda, p_\lambda} = 2\sum_{\boldsymbol{k}_\lambda}\frac{\Delta\boldsymbol{k}_\lambda}{\Delta\boldsymbol{k}_\lambda} = \frac{2}{\Delta\boldsymbol{k}_\lambda}\sum_{\boldsymbol{k}_\lambda}\Delta\boldsymbol{k}_\lambda = \frac{2V_{cav}}{(2\pi)^3}\sum_{\boldsymbol{k}_\lambda}\Delta\boldsymbol{k}_\lambda. \tag{2.48}$$

The periodic boundary conditions require ($\Delta\boldsymbol{k}_\lambda = (\frac{2\pi}{L})^3$). We now switch over to continuous wavemodes $\boldsymbol{k}_\lambda$. As we want the density of states to depend on $\omega_{\boldsymbol{\lambda}}$, we build the threshold integral of Eq. (2.48) in spherical coordinates and substitute ($\mathrm{d}k_\lambda = \mathrm{d}\omega_{\boldsymbol{\lambda}}/c$). We find

$$\begin{aligned}
\frac{2V_{cav}}{(2\pi)^3}\lim_{\Delta\boldsymbol{k}_\lambda\to 0}\sum_{\boldsymbol{k}_\lambda}\Delta\boldsymbol{k}_\lambda &= \frac{2V_{cav}}{(2\pi)^3}\int \mathrm{d}^3\boldsymbol{k}_\lambda \\
&= \frac{2V_{cav}}{(2\pi)^3}\underbrace{\int_0^\infty \mathrm{d}k_\lambda k_\lambda^2}_{\int_0^\infty \frac{\omega_{\boldsymbol{\lambda}}^2}{c^3}\mathrm{d}\omega_{\boldsymbol{\lambda}}}\underbrace{\int_0^\pi d\Theta\sin\Theta\int_0^{2\pi} d\phi}_{4\pi} \\
&= \int_0^\infty \frac{\omega_{\boldsymbol{\lambda}}^2 V_{cav}}{\pi^2 c^3}\mathrm{d}\omega_{\boldsymbol{\lambda}}.
\end{aligned}$$

So what is new due to the assumption of quasi-continuous wavevectors is our density of states in vacuum

$$\sum_{\boldsymbol{k}_\lambda,\lambda} \xrightarrow{\Delta \boldsymbol{k}_\lambda \to 0} \int_0^\infty \frac{\omega_{\boldsymbol{\lambda}}^2 V_{cav}}{\pi^2 c^3} \mathrm{d}\omega_{\boldsymbol{\lambda}} = \int_0^\infty D_{vac}(\omega_{\boldsymbol{\lambda}}) \mathrm{d}\omega_{\boldsymbol{\lambda}} \qquad \text{with } D_{vac}(\omega_{\boldsymbol{\lambda}}) = \frac{\omega_{\boldsymbol{\lambda}}^2 V_{cav}}{\pi^2 c^3}.$$

After all, Eq. (2.47) becomes

$$\Gamma_{vac} = \frac{\omega_{\boldsymbol{\lambda}}^3 \mu_{\boldsymbol{k}}^2}{3\pi c^3 \varepsilon_0 \varepsilon_r \hbar}. \tag{2.49}$$

Alternatively we can receive the Einstein coefficient of spontaneous emission in vacuum by regarding a fully quantized two-level system for a semiconductor after rotating-wave-, Born- and Markov-approximation.

The Einstein coefficient of spontaneous emission in a cavity can be found by replacing $D_{vac}(\omega_{\boldsymbol{k}})$ with $D_{cav}(\omega_{\boldsymbol{k}})$ in Eq. (2.47)

$$\Gamma_{cav} = \frac{\mu_{\boldsymbol{k}}^2 \omega_{\boldsymbol{\lambda}} \pi}{3\varepsilon_0 \varepsilon_r \hbar V_{cav}} D_{cav}(\omega_{\boldsymbol{\lambda}}).$$

Under the condition, that our density of states consists of only 1 wavemode

$$\int_0^\infty D_{cav}(\omega_{\boldsymbol{\lambda}}) \mathrm{d}\omega_{\boldsymbol{\lambda}} = 1,$$

we can assume $D_{cav}(\omega_{\boldsymbol{\lambda}})$ as a Lorentz function

$$D_{cav}(\omega_{\boldsymbol{\lambda}}) = \frac{2}{\pi\kappa} \frac{\kappa^2}{4(\omega_{\boldsymbol{k}} - \omega_{\boldsymbol{\lambda}})^2 + \kappa^2},$$

where κ is the decay rate of the photon density due to resonator losses, $\omega_{\boldsymbol{k}}$ is the atomic transition frequency and $\omega_{\boldsymbol{\lambda}}$ the light frequency. This function is normalized by the factor $(2\pi\kappa)^{-1}$ and describes the natural linewidth. Considering the case of resonance ($\omega_{\boldsymbol{k}} \approx \omega_{\boldsymbol{\lambda}}$), the second fraction vanishes and we get

$$D_{cav}(\omega_{\boldsymbol{k}}) = \frac{2}{\pi\kappa} = \frac{2Q}{\pi\omega_{\boldsymbol{\lambda}}},$$

where ($Q = \omega_{\boldsymbol{\lambda}}/\kappa$) is the quality factor of the resonator. Finally the Einstein coefficient of spontaneous emission in a cavity becomes

$$\begin{aligned} \Gamma_{cav} &= \frac{\mu_{\boldsymbol{k}}^2 \omega_{\boldsymbol{\lambda}} \pi}{3\varepsilon_0 \varepsilon_r \hbar V_{cav}} \frac{2Q}{\pi\omega_{\boldsymbol{\lambda}}} \\ &= \frac{2\mu_{\boldsymbol{k}}^2 Q}{3\varepsilon_0 \varepsilon_r \hbar V_{cav}}. \end{aligned} \tag{2.50}$$

Inserting Eq. (2.50) and (2.49) in Eq. (2.44), we receive the Purcell factor

$$F_P = \frac{3}{4\pi^2 n^3} \frac{Q\lambda_0^3}{V_{cav}},$$

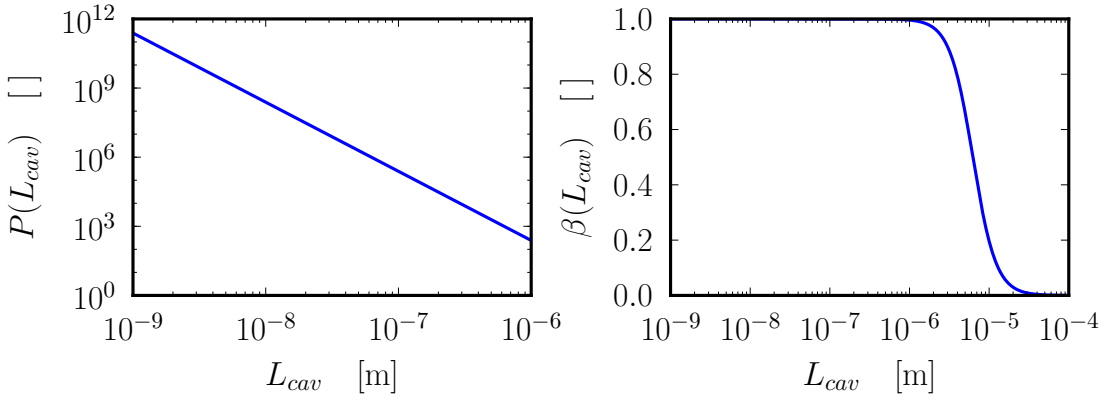

Figure 2.4: Purcell and β-factor versus cavity length.

where λ_0/n is the wavelength within the active media with refractive index n.
To summarize the necessary assumptions for enhancement of spontaneous emission, we need a high quality factor Q, a small cavity volume V_{cav} and an approximately resonant laser field. This means in reversal conclusion, that spontaneous emission can be inhibited using strongly dissonant wavelengths, so that the DOS $D_{cav}(\omega_{\boldsymbol{\lambda}})$ is small and there is no wavemode in which the light can be emitted. Fig. 2.4 shows the Purcell factor plotted versus the cavity length ($L_{cav} = \sqrt[3]{V_{cav}}$).

2.5 Deterministic spontaneous emission

There are different ways to implement the spontaneous emission afterwards as an phenomenological amendment, as the derivation of this effect is based on a fully quantized Hamiltonian. We choose for our purpose the deterministic implementation of spontaneous emission via rate. An approach via stochastic noise-term would be problematic, because we could not evaluate a small signal response in noisy time series, which is the main focus of this thesis.
The rate of spontaneous emission processes per quantum-dot [PAU12] is given by the term

$$R_{\boldsymbol{k}}^{sp} = \frac{\varrho_{\boldsymbol{k}}^2}{\tau_{sp}} = \frac{1}{\tau_{sp}} \cdot \left(\frac{d_{\boldsymbol{k}} + 1}{2}\right)^2,$$

where ($\varrho_{\boldsymbol{k}} = \varrho_{\boldsymbol{k}}^e = \varrho_{\boldsymbol{k}}^h$) is assumed and Eq. 2.13 is used. When adding this rate to the wave equation of the electric field, this term is influenced by the number of quantum dots Z^{QD}, their spin degeneracy 2, the confinement factor Γ, the Purcell factor F_P and the β-factor. The β-factor is the percentage of spontaneously emitted photons, which are emitted inside a resonant cavity wavemode. It is defined by

$$\beta := \frac{\Gamma_{cav}}{\Gamma_{vac} + \Gamma_{cav}}$$

and can, when expanded by Γ_{vac}^{-1}, be expressed via the Purcell factor F_P

$$\beta = \frac{F_P}{1+F_P}.$$

The change of the photon number N_{ph} due to spontaneous emission processes, is then given by

$$\left.\frac{d}{dt}N_{ph}\right|_{sp} = \sum_{\boldsymbol{k},s_z} \beta F_P R_{\boldsymbol{k}}^{sp} = 2Z^{QD}\Gamma\beta F_P \frac{1}{\tau_{sp}} \cdot \left(\frac{d+1}{2}\right)^2,$$

where the factor two takes the spin degeneracy per quantum dot into account. Remembering Eq. (2.41) we can write the change of the wave amplitude function c due to spontaneous emission processes as

$$\Longrightarrow \quad \left.\frac{d}{dt}c\right|_{sp} = \frac{1}{2c}\left.\frac{d}{dt}N_{ph}\right|_{sp} = \frac{Z^{QD}\Gamma\beta F_P}{\tau_{sp}c} \cdot \left(\frac{d+1}{2}\right)^2 \qquad \forall c \in \mathbb{R}^+.$$

The change of inversion due to spontaneous emission processes is slightly different, as only the Purcell factor effects the inversion

$$\left.\frac{d}{dt}d\right|_{sp} = \frac{F_P}{\tau_{sp}} \cdot \left(\frac{d+1}{2}\right)^2.$$

We now write down explicitely the equation systems we want to compare in the following.

The set of real valued Bloch equations with spontaneous emission:

$$\dot{c} = -\kappa c + 2Z^{QD}\Gamma|g|p + \frac{Z^{QD}\Gamma\beta F_P}{\tau_{sp}c} \cdot \left(\frac{d+1}{2}\right)^2, \tag{2.51}$$

$$\dot{p} = -\gamma p + |g|cd, \tag{2.52}$$

$$\dot{d} = -4|g|cp + \frac{d_0(w_e)-d}{T_1(w_e)} - \frac{F_P}{\tau_{sp}} \cdot \left(\frac{d+1}{2}\right)^2. \tag{2.53}$$

The set of rate equations with spontaneous emission:

$$\dot{c} = -\kappa c + \frac{2Z^{QD}\Gamma g^2}{\gamma}cd + \frac{Z^{QD}\Gamma\beta F_P}{\tau_{sp}c} \cdot \left(\frac{d+1}{2}\right)^2, \tag{2.54}$$

$$\dot{d} = -\frac{4g^2}{\gamma}c^2 d + \frac{d_0(w_e)-d}{T_1(w_e)} - \frac{F_P}{\tau_{sp}} \cdot \left(\frac{d+1}{2}\right)^2. \tag{2.55}$$

2.6 Notes to the numerics

The simulations have been performed with different programs and with different algorithms, as each type of numerical problem underlies individual claims. The major part, like programs for solving the differential equation systems and evaluating the time series for bifurcation and modulation diagrams have been written in the programming language

C++. Analytical approaches, like determining Eigenvalues, were done with *Wolfram Mathematica*. All plots were created with *Pythons* plotting package *Matplotlib*.
The integration routines used for numerical calculations and solving the differential equation systems should be briefly mentioned. Three integration methods [Pre07] were compared with each other:

- Runge-Kutta fourth order,
- Dormand-Prince eighth order (adaptive step size control),
- Bulirsch-Stoer (adaptive step size control).

The most straight forward integration technique for ordinary nonlinear differential equations is the Runge-Kutta fourth order method (Appendix A.6), an advancement of the very simple Euler method. It is trustworthy, naturally not error-prone, often used and a great compromise between efficiency and simplicity. For simulating the time series and bifurcation diagrams, where the pump strength is set as the control parameter, the method is -how it turns out- an appropriate choice. But besides the praise there are further aspects to think about. Time steps have to be adapted manually according the system's timescales. This is problematic if the controlled timescales are ranged over several orders of magnitude. In our example a high spontaneous emission rate τ_{sp} requires very short time steps, but this again drastically increases the simulation runtime, as not all parameters in a simulation require this high accuracy. At this point one have to admit, that a method with adaptive step size control is favourable.
The Dormand-Prince method of eighth order, with fifth and third order for error control, and the Bulirsch-Stoer (sometimes called Gragg-Bulirsch-Stoer) method have been compared with each other. The Bulirsch-Stoer algorithm provides higher accuracy for smooth integrands without singularities, whereby the simulation runtime is higher compared to a Runge-Kutta based method. The Dormand-Prince method with eleven function evaluations per time step is part of the Runge-Kutta family and is suitable for strongly volatile functions, with which we are obviously confronted. It is very time saving to decrease the step size when the laser reaches its steady state after the turn-on oscillations. Especially changing the modulation frequency between $10^9\,\mathrm{s}^{-1}$ and $10^{13}\,\mathrm{s}^{-1}$ require extremely different time step sizes. Finally great results could be achieved by the Dormand-Prince algorithm, as simulation runtime was drastically decreased. E.g. for Fig. 5.6a runtime decreases from five days down to 6 hours, compared to the Runge-Kutta method of fourth order.

2.6.1 Parameters

This subsection shall give a brief overview over the system parameters used in all our equations. It is divided into

- parameters, which remain unvaried for all simulations,
- parameters, which may be varied if explicitely declared in the figure caption and
- the main control parameters.

The procedure we choose in order to compare simulations with different parameter sets, is to vary the gain G and adjust the coupling constant $|g|$

$$|g| = \mu\sqrt{\frac{\omega_\lambda}{2\hbar\varepsilon_0\varepsilon_r V_{cav}}} \quad \Longrightarrow \quad |g| = \sqrt{\frac{\gamma c_n G}{2Z^{QD}\Gamma}}.$$

The semiconductor gain G is given in units of cm^{-2}. This is an important empirically accessible quantity, which, if set to a fixed value, is easy to refer to a real laser device. It is not desirable to have a different gain for each simulation due to the change of our control parameters. The main control parameters are the pump parameter d_0 or the electron density in the wetting layer w_e and the timescales

$$\kappa, \quad \gamma, \quad T_1^{-1}(w_e), \quad \tau_{sp}.$$

The Purcell factor F_P and the beta factor β are set to one in order to examine the influence of spontaneous emission isolated.

unvaried parameters			**if not redeclared explicitly**		
meaning	symbol	value	meaning	symbol	value
number of quantum dots	Z^{QD}	1000	gain	G	$700\,\mathrm{cm}^{-2}$
confinement factor	Γ	$0,01$			
refractive index	n	$3,77$			
dielectric constant	ε_r	$\sqrt{n}$			
speed of light in medium	c_n	c_0/n			
dipole moment	μ	$0,6e_0\,\mathrm{nm}$			
transition frequency	ω_λ	$2\pi \cdot 230\,\mathrm{THz}$			
quality factor	Q	ω_λ/κ			
coupling constant	$\|g\|$	$\sqrt{\frac{\gamma c_n G}{2Z^{QD}\Gamma}}$			
Purcell factor	F_P	1			
beta factor	β	1			
cavity volume	V_{cav}	$(10^{-6})^3\,\mathrm{m}^3$			

Table 2.6.1: Parameters used in simulations.

3 Linear stability analysis

Our laser system is modeled by a differential equation system of the form

$$\dot{\boldsymbol{q}} = \boldsymbol{F}(\boldsymbol{q}, \boldsymbol{k}),$$

where $\boldsymbol{q} := (q_1, q_2, ..., q_n)$ is a set of n dynamic variables, $\boldsymbol{k} := (k_1, ..., k_m)$ a set of m control parameters, and $\boldsymbol{F} := (F_1, F_2, ..., F_n)$ a set of n nonlinear functions of $\boldsymbol{q}$. Control parameters can be any kind of nondynamic quantities like the pump current, the cavity size, external fields, material constants or other external parameters.
The linear stability analysis is a powerful tool to describe the temporal evolution of small perturbations of a trajectory $\boldsymbol{u}_{\boldsymbol{q_0}}(t)$, i.e. the behaviour of a trajectory $\boldsymbol{v}_{\tilde{\boldsymbol{q}}_{\boldsymbol{0}}}(t)$ (with a different initial condition $\tilde{q}_0$) close by the solution $\boldsymbol{u}_{\boldsymbol{q_0}}(t)$.
A system without an explicit time dependence

$$\frac{\partial \boldsymbol{F}}{\partial t} = \boldsymbol{0}$$

is called *autonomous*, otherwise *nonautonomous*. The laser rate equations ($n = 2$) and the semiconductor Bloch equations ($n = 3$), which are dealt with in this thesis, are autonomous systems.
Points of interest are the fixed points $\boldsymbol{q'} = (q'_1, q'_2, ..., q'_n)$ of the system, where

$$\boldsymbol{F}(\boldsymbol{q'}, \boldsymbol{k}) = \boldsymbol{0}. \tag{3.1}$$

To find out whether a fixed point is stable or not and how the routes to stability or instability look like in detail, we have to do further investigations.
Considering the perturbed dynamic variables as

$$\boldsymbol{q}(t) = \boldsymbol{q'} + \delta\boldsymbol{q}(t), \tag{3.2}$$

where $\delta\boldsymbol{q}(t)$ is a small perturbation around the fixed point $\boldsymbol{q'}$, we can write the temporal evolution of the perturbation as a first order Taylor expansion around the fixed point

$$\begin{aligned}
\delta\dot{q}_i &= \dot{q}_i - \underbrace{\dot{q}'_i}_{=0} \\
&= F_i(\boldsymbol{q}, \boldsymbol{k}) \\
&\overset{\text{Taylor}}{\approx} \underbrace{F_i(\boldsymbol{q'}, \boldsymbol{k})}_{=0} + \sum_{j=1}^{n} \left.\frac{\partial F_i}{\partial q_j}\right|_{\boldsymbol{q'}} (\delta q_j - \boldsymbol{q'}) \qquad (3.3) \\
&\approx \sum_{j=1}^{n} \underbrace{\left.\frac{\partial F_i}{\partial q_j}\right|_{\boldsymbol{q'}}}_{\underline{\underline{A}}_{ij}} \delta q_j. \qquad (3.4)
\end{aligned}$$

After the Taylor expansion of the derived perturbation we receive a linearized system of differential equations

$$\delta\dot{\boldsymbol{q}} = \underline{\underline{A}} \cdot \delta\boldsymbol{q}. \tag{3.5}$$

The general solution of a system of linear differential equations is known by

$$\delta \boldsymbol{q}(t) = \sum_{i=1}^{n} C_i \vec{\boldsymbol{\eta}}_i e^{\lambda_i t},$$

where n is the number of eigenvalues, C_i are constants, $\boldsymbol{\eta}_i$ the eigenvectors and λ_i the eigenvalues of the linearized system. The dynamics of the perturbations nearby the fixed points are now determined by the eigenvalues λ_i of the Jacobian matrix $\underline{\underline{A}}$. Solving the characteristic polynomial

$$\det(\underline{\underline{A}} - \lambda \mathbb{1}) \stackrel{!}{=} 0 \tag{3.6}$$

gives us the complex eigenvalues

$$\lambda_i = \Gamma_{RO,i} + \mathrm{i}\omega_{RO,i}, \quad i \in \{1, ..., n\}. \tag{3.7}$$

The imaginary parts of the eigenvalues are the eigenfrequencies ω_i in the direction of the i'th eigenvector of the lasing system, which show up as the relaxation oscillation frequencies of the photon number during nonchaotic lasing. The real parts $\Gamma_{RO,i}$ describe the damping of the systems relaxation oscillations and can be recognized as the exponential decay of the relaxation oscillations. The imaginary and real parts of the eigenvalues contain important information about the stability character of a solution, as we will see in the following.

3.1 Phase portraits, stability properties and bifurcations

A phase space visualizes all possible states of a system. All dynamical variables of a differential equation system are plotted versus each other. One single point in a phase space represents a current state of the system. The time variable is not part of the plot, but one solution for different times gives us several points in phase space, which altogether form a well defined trajectory. The trajectory represents a solution of the differential equation system and is fully deterministic, which means every initial point (except for fixed points) in phase space obey the field of directions given by $\boldsymbol{F}$. Each initial condition leads to a different trajectory in phase space. In autonomous systems a trajectory can never cross itself. The uniqueness of a trajectory is lost for nonautonomous systems, thus for a given phase point $\boldsymbol{q}$, different times lead to different (time-dependent) directions $\boldsymbol{F}$.
A phase portrait can be achieved by sketching this qualitative vector field which represents trajectories for different initial conditions. These lines are analogous to streamlines in fluids or field lines of magnetic fields. If all parameters and the initial condition of an equation system are set, the variety of trajectories reduces to a single one. The phase portrait can change qualitatively by modifying a control parameter k, what is called bifurcation. Before we specify in the variety of bifurcations, we should have a closer look at the stability concept.

A solution $\boldsymbol{u}_{\boldsymbol{q_0}}(t)$ is called *locally stable*, if close by solutions $\boldsymbol{v}_{\tilde{\boldsymbol{q}}_0}(t)$ with different initial conditions stay close to $\boldsymbol{u}_{\boldsymbol{q_0}}(t)$ for all times. It is called *globally stable*, if all trajectories in the phase space converge to the initial solution. A local stable solution is *locally*

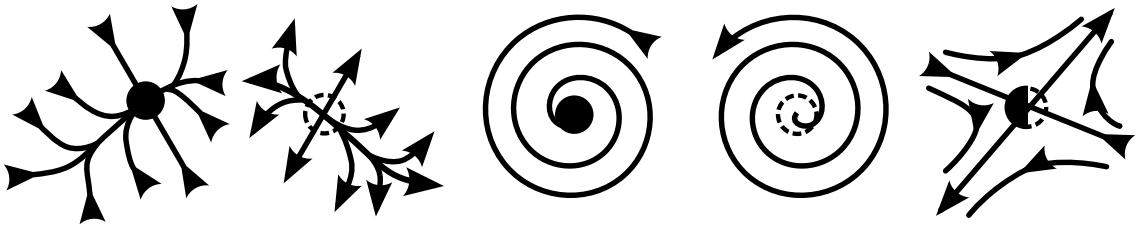

(a) Stable node (b) Unstable node (c) Stable focus (d) Unstable focus (e) Saddle point

Figure 3.1: Schemes of the five qualitatively different configurations of solutions, visualized in two-dimensional phase portraits.

asymptotically stable if

$$\lim_{t\to\infty} |\boldsymbol{u}_{\boldsymbol{q_0}}(t) - \boldsymbol{v}_{\tilde{\boldsymbol{q}}_\mathbf{0}}(t)| = 0$$

is fulfilled. In this case the system moves into a *steady state* where Eq. (3.1) holds. The sufficient condition for local asymptotic stability are negative real parts

$$\mathrm{Re}[\lambda_i] < 0,$$

of the eigenvalues of the linearized system (3.5), because this implies a damped motion of the perturbance. Another important but weaker form of stability is *orbital stability*. Here the phase points nearby a trajectory stay within a given distance for all times. This geometric form of a trajectory is called *limit cycle*. This kind of solution is stable in spite of a non-existent steady state.
The routes to stability or instability can be known by examining the eigenvalues. Fig. 3.1 shows the five different configurations of the eigenvalues. They differ from each other in their sign and existence of imaginary and real part. Trajectories around a given fixed point can approach it, if the real part is negative. If the real part is negative and the imaginary part is zero (Fig. 3.1a - stable node) the trajectories nearby the fixed points simply approach it asymptotically, if therefore the imaginary part is non-zero, the trajectories spiral into the steady state (Fig. 3.1c - stable focus). Analogous to this behaviour we have the case of unstable fixed points (Fig. 3.1b and Fig. 3.1d - Unstable node and unstable focus). Slightly different is the case of a saddle point in Fig. 3.1e, where the eigenvalue is real with one value positive and the other negative, so the perturbance in direction of the eigenvector with the appropriate positive real part increases exponentially and causes an instability. A laser with more than two degrees of freedom is able to become a chaotic system, as the trajectory can then arbitrarily oscillate around a fixed point without crossing itself.

Bifurcation phenomena show up as qualitative changes in phase space topology while changing a control parameter k. They usually occur when different steady-state solution branches intersect or coalesce. The change of the stability character due to the modification of a control parameter is a phenomenon, which only occurs in nonlinear dynamic systems. Nonlinear equations are necessary to describe thermodynamic systems, driven into a state far from thermodynamic equilibrium, due to the coupling to external fluxes of energy, like in our case to an external injected pump current. Thus bifurcations are nonequilibrium phase transitions. These phase transitions are classified by their lowest derivative of the

free energy, that is discontinuous at the bifurcation point. A transition is said to be of order two, if the state variable changes continuously, whereas the derivative with respect to the control parameter is discontinuous. In a first order phase transition the state variable itself changes discontinuously.
In the process of this thesis we will encounter several bifurcation phenomena, what helps us understand the theory.

3.2 Analysis of rate and Bloch equations

We will examine the stability properties of the singular points of our two-variable autonomous system of rate equations and three-variable autonomous system of Bloch equations. For that reason we need to know the singular points of the system, where we may linearize around. This linearization makes the system analytically solvable around the singular points. The examination of the borderlines between the regimes of stability, which occur at the bifurcation points, requires the involving of higher orders in the Taylor expansion (Eq. (3.3)) around the singular points. The results of this section, namely the eigenvalues of the systems, will accompany our simulations through the entire thesis.

3.2.1 Linearizations

We linearize our equation systems as we determine the Jacobian matrix $\underline{\underline{A}}$ from Eq. (3.4). We do this procedure for all of our equation systems we will examine in this thesis, rate and Bloch equations, with and without spontaneous emission, respectively. Note that scattering rates are always considered.

Linearized Bloch equations (Eqs. (2.34) to (2.36)) **without spontaneous emission:**

$$\frac{d}{dt}\begin{pmatrix}\delta c(t)\\ \delta p(t)\\ \delta d(t)\end{pmatrix} = \underbrace{\begin{pmatrix}-\kappa & 2Z^{QD}\Gamma g & 0\\ gd' & -\gamma & gc'\\ -4gp' & -4gc' & -\frac{1}{T_1(w_e)}\end{pmatrix}}_{\underline{\underline{A}}}\begin{pmatrix}\delta c(t)\\ \delta p(t)\\ \delta d(t)\end{pmatrix}. \tag{3.8}$$

Linearized Bloch equations (Eqs. (2.51) to (2.53)) **with spontaneous emission:**

$$\frac{d}{dt}\begin{pmatrix}\delta c(t)\\ \delta p(t)\\ \delta d(t)\end{pmatrix} = \begin{pmatrix}-\kappa - \frac{Z^{QD}\Gamma\beta F_P(d'+1)^2}{4\tau_{sp}c'^2} & 2Z^{QD}\Gamma g & \frac{Z^{QD}\Gamma\beta F_P(d'+1)}{2\tau_{sp}c'}\\ gd' & -\gamma & gc'\\ -4gp' & -4gc' & -\frac{1}{T_1(w_e)} - \frac{F_P(d+1)}{2\tau_{sp}}\end{pmatrix}\begin{pmatrix}\delta c(t)\\ \delta p(t)\\ \delta d(t)\end{pmatrix}. \tag{3.9}$$

Linearized rate equations (Eqs. (2.37) and (2.38)) **without spontaneous emission:**

$$\frac{d}{dt}\begin{pmatrix}\delta c(t)\\ \delta d(t)\end{pmatrix} = \begin{pmatrix}-\kappa + \frac{2Z^{QD}\Gamma g^2 d'}{\gamma} & \frac{2Z^{QD}\Gamma g^2 c'}{\gamma}\\ -\frac{8g^2c'd'}{\gamma} & -\frac{1}{T_1(w_e)} - \frac{4g^2c'^2}{\gamma}\end{pmatrix}\begin{pmatrix}\delta c(t)\\ \delta d(t)\end{pmatrix}. \tag{3.10}$$

Linearized rate equations (Eqs. (2.54) and (2.55)) **with spontaneous emission:**

$$\frac{d}{dt}\begin{pmatrix}\delta c(t)\\ \delta d(t)\end{pmatrix} = \begin{pmatrix} -\kappa + \frac{2Z^{QD}\Gamma g^2 d'}{\gamma} - \frac{Z^{QD}\Gamma\beta F_P(d'+1)^2}{4\tau_{sp}c'^2} & \frac{2Z^{QD}\Gamma g^2 c'}{\gamma} + \frac{Z^{QD}\Gamma\beta F_P(d'+1)}{2\tau_{sp}c'} \\ -\frac{8g^2c'd'}{\gamma} & -\frac{1}{T_1(w_e)} - \frac{4g^2c'^2}{\gamma} - \frac{F_P(d'+1)}{2\tau_{sp}} \end{pmatrix}\begin{pmatrix}\delta c(t)\\ \delta d(t)\end{pmatrix}. \tag{3.11}$$

3.2.2 Fixed points

Solving the Bloch Eqs. (2.34), (2.35) and (2.36) for the steady state after Eq. (3.1) gives us two singular points

$$(i) \quad c_1' = 0, \quad p_1' = 0, \quad d_1' = d_0(w_e), \tag{3.12}$$

$$(ii) \quad c_2' = \sqrt{\frac{2Z^{QD}\Gamma g^2 d_0(w_e) - \kappa\gamma}{4g^2\kappa T_1(w_e)}}, \quad p_2' = \sqrt{\frac{\kappa(2Z^{QD}\Gamma g^2 d_0(w_e) - \kappa\gamma)}{16Z^{QD}\Gamma g^4 T_1(w_e)}} \tag{3.13}$$

$$d_2' = \frac{\kappa\gamma}{2Z^{QD}\Gamma g^2}$$

in the three-dimensional phase space. For the rate equations the phase space reduces to a phase plane. Accordingly to the procedure we made for the Bloch equations, we find for the rate Eqs. (2.37) and (2.38) the two singular points

$$(i) \quad c_1' = 0, \quad d_1' = d_0(w_e), \tag{3.14}$$

$$(ii) \quad c_2' = \sqrt{\frac{2Z^{QD}\Gamma g^2 d_0(w_e) - \kappa\gamma}{4g^2\kappa T_1(w_e)}}, \quad d_2' = \frac{\kappa\gamma}{2Z^{QD}\Gamma g^2}. \tag{3.15}$$

In each case we find a nonlasing fixed point (i), where no photon emission occurs $c_1' = 0$, and a lasing fixed point (ii), with $c_1' > 0$ for pumping beyond the first laser threshold $d_0(w_e) > d_0^{(1)}$. Note that Fixpoints for the rate and Bloch equations with spontaneous emission, respectively, can basically be found analytically, but one cannot distinguish tendencies out of the expressions due to the complexity, which is the reason for doing analytics. Instead Eq. (3.1) will be solved fully numerical for each set of parameters.

3.2.3 Eigenvalues

The eigenvalues of the Jacobian matrix (3.4) give us information about whether a fixed point is stable or not. Furthermore we can determine the routes to stability and instability (Fig. 3.1). Therefore we solve the characteristic equation (3.6) for each fixed point. Analytically reasonable is that for the linearized rate and Bloch equations without spontaneous emission. Also the analytical expression for the eigenvalues of the Bloch equations (Appendix A.4) around the second fixed point (3.13) is not useful for our purpose. Any eigenvalue, which is not listed in this section is computed fully numerical.
The characteristic polynomial for 2x2-matrices can be written by the general expression

$$\det(\underline{\underline{A}} - \lambda\mathbb{1}) = \lambda^2 - \lambda\mathrm{tr}(\underline{\underline{A}}) + \det(\underline{\underline{A}}),$$

which gives us two eigenvalues

$$\lambda_{1,2} = \frac{1}{2}\left(\mathrm{tr}(\underline{\underline{A}}) \pm \mathrm{i}\sqrt{4\mathrm{det}(\underline{\underline{A}}) - \mathrm{tr}^2(\underline{\underline{A}})}\right). \tag{3.16}$$

We find two eigenvalues of the linearized rate equation system without spontaneous emission (3.10) for the first fixed point (3.14)

$$\begin{aligned} \lambda_{r11} &= -\frac{1}{T_1(w_e)}, \\ \lambda_{r12} &= -\kappa + \frac{2Z^{QD}\Gamma d_0(w_e)g^2}{\gamma} \end{aligned}$$

and for the second fixed point (3.15)

$$\begin{aligned} \lambda_{r21} &= \frac{-\gamma + \sqrt{\gamma(-16Z^{QD}\Gamma d_0(w_e)g^2T_1(w_e) + \gamma + 8\kappa T1(w_e)\gamma)}}{2T_1(w_e)\gamma}, \\ \lambda_{r22} &= \frac{-\gamma - \sqrt{\gamma(-16Z^{QD}\Gamma d_0(w_e)g^2T_1(w_e) + \gamma + 8\kappa T1(w_e)\gamma)}}{2T_1(w_e)\gamma}. \end{aligned}$$

For the linearized Bloch equation system without spontaneous emission (3.8) we confine ourselves to the three eigenvalues corresponding to the first fixed point (3.12)

$$\begin{aligned} \lambda_{b11} &= -\frac{1}{T_1(w_e)}, \\ \lambda_{b12} &= \frac{1}{2}(-\kappa - \gamma - \sqrt{-\kappa^2 + 8Z^{QD}\Gamma d_0(w_e)g^2 - 2\kappa\gamma + \gamma^2}), \\ \lambda_{b13} &= \frac{1}{2}(-\kappa - \gamma + \sqrt{-\kappa^2 + 8Z^{QD}\Gamma d_0(w_e)g^2 - 2\kappa\gamma + \gamma^2}). \end{aligned}$$

An example of the informational content of the linear stability analysis is depicted in Fig. 3.2. Here a transcritical bifurcation occurs due to the intersection of two steady state solution branches at the bifurcation point k_0. The system acquires only the stable solution branch given by the fixed points, which is not known until the consideration of the systems eigenvalues. The graphic shows a simple laser turn-on while increasing the pumping parameter d_0.

3.3 Laser thresholds

The linear stability analysis offers the opportunity to get an analytical expression for the system's bifurcation points. Namely the laser thresholds show up as a change of stability. The first laser threshold is the value of the pump parameter at which the laser emission starts (transcritical bifurcation). The second laser threshold describes the change from a stable to a chaotic emitting behaviour (supercritical Hopf bifurcation). In order to calculate expressions for the first threshold, we make use of the linearized system matrix $\underline{\underline{A}}$ of Eq. (3.8). We put in our first singular point and calculate the characteristic polynomial. The condition for the first threshold is a vanishing real and imaginary part

$$\mathrm{Re}[\lambda] = \mathrm{Im}[\lambda] = 0 \quad \Leftrightarrow \quad \lambda = 0.$$

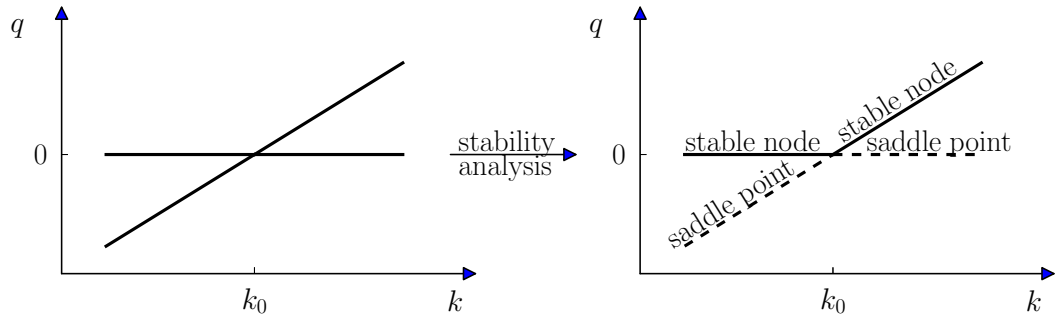

Figure 3.2: Graphic shows schematically a dynamic variable q versus the control parameter k. The left graphic visualizes only the fixed points, the right graphic shows the stable solution branches, in which the system will move. At the bifurcation point k_0 a transcritical bifurcation occurs.

At this point the damping becomes negative while there is still no relaxation oscillation ($\mathrm{Im}[\lambda] = 0$). We find

$$\det(\underline{\underline{A}} - \lambda \mathbb{1}) = \frac{2d_0 g^2 Z^{QD} \Gamma - \kappa\gamma}{T_1} \stackrel{!}{=} 0.$$

Solving this equation for a fixed pump parameter gives us the first laser threshold

$$d_0^{(1)} = \frac{\kappa\gamma}{2g^2 Z^{QD}\Gamma}. \tag{3.17}$$

For the second laser threshold, the same procedure has to be performed, but under the condition of a vanishing real part while the laser emission is oscillating

$$\begin{aligned} \mathrm{Re}[\lambda] = 0, \qquad & \mathrm{Im}[\lambda] \neq 0 \\ \Leftrightarrow & \\ \lambda^3 = -\mathrm{i}\omega^3, \quad \lambda^2 \;=\; & -\omega^2, \quad \lambda = \mathrm{i}\omega. \end{aligned}$$

At this bifurcation point the real part becomes positive again, so there is no damping but a chaotic enhancement of the oscillating emission. As the characteristic polynomial shall be zero, the imaginary and the real part shall be zero, respectively. This condition leads with the second singular point to

$$\begin{aligned} \mathrm{Im}[\det(\underline{\underline{A}} - \lambda\mathbb{1})] &= \omega^3 - \omega\left(\frac{\kappa}{T_1} + \frac{2d_0 g^2 Z^{QD}\Gamma}{\kappa T_1}\right) \stackrel{!}{=} 0, \\ \mathrm{Re}[\det(\underline{\underline{A}} - \lambda\mathbb{1})] &= \omega^2\left(\kappa + \frac{1}{T_1} + \gamma\right) - \left(\frac{4d_0 g^2 Z^{QD}\Gamma - 2\kappa\gamma}{T_1}\right) \stackrel{!}{=} 0. \end{aligned}$$

We solve these equations for ω^2, equate them and find the second laser threshold

$$d_0^{(2)} = -\frac{\kappa^2(1 + 3T_1\gamma + T_1\kappa)}{2g^2 Z^{QD}\Gamma(1 + T_1\gamma - T_1\kappa)}. \tag{3.18}$$

It is useful to formulate a condition for the existence of a second laser threshold. This is true if Eq. (3.18) becomes positive. This directly gives us the so-called *bad cavity condition*

$$\kappa > \frac{1}{T_1} + \gamma. \tag{3.19}$$

If the bad cavity condition is fulfilled, laser emission is chaotic, as long as the device is pumped beyond the second laser threshold.

3.4 Analytical approach for the small signal response

The modulation of quantum dot laser devices is another topic, which can be accessed with the linear stability analysis. In this section we want to derive an expression for modulability of our rate equation system (3.10) without spontaneous emission. An external modulation of the pump current

$$d_0(t) = d_0 + A_0 \sin(\omega t)$$

with the modulation angular frequency ω and its dimensionless amplitude factor A_0 effects the outgoing intensity $|c|^2$, where the amplitude of the transferred modulation signal varies with ω. The system at a certain frequency gets too inerted to follow the external modulation and the transferred amplitude asymptotically approaches zero.
We start our derivation with the damping Γ_{RO} and the relaxation oscillation frequency ω_{RO} of the system. Thus we compare Eq. (3.16) with Eq. (3.7) and find for 2x2-matrices

$$\begin{aligned} \Gamma_{RO}^2 &= \frac{\mathrm{tr}^2(\underline{\underline{A}})}{4}, \\ \omega_{RO}^2 &= \det(\underline{\underline{A}}) - \frac{\mathrm{tr}^2(\underline{\underline{A}})}{4}, \end{aligned}$$

where

$$\begin{aligned} \mathrm{tr}(\underline{\underline{A}}) &= Gd' - \kappa - \frac{1}{T_1(w_e)}, \\ \det(\underline{\underline{A}}) &= \frac{\kappa - Gd'}{T_1(w_e)} + 4G^2 d' c'^2. \end{aligned}$$

The Linearization of the system makes it possible to derive a damped harmonic oscillator equation for the photonic perturbation δc, given by Eq. (3.10). Hence we create the second time derivative and find

$$\begin{aligned} \ddot{\delta c}(t) &= A_{11}\dot{\delta c}(t) + A_{12}\dot{\delta d}(t) \\ &= (A_{11} + A_{22})\dot{\delta c}(t) - (A_{11}A_{22} - A_{12}A_{21})\delta c(t) \\ &\Longleftrightarrow \\ 0 &= \ddot{\delta c}(t) - \mathrm{tr}(\underline{\underline{A}})\dot{\delta c}(t) + \det(\underline{\underline{A}})\delta c(t), \end{aligned}$$

which we can now modify by an external driven pump modulation

$$\ddot{\delta c}(t) - \mathrm{tr}(\underline{\underline{A}})\dot{\delta c}(t) + \det(\underline{\underline{A}})\delta c(t) = A_0 e^{\mathrm{i}\omega t}. \tag{3.20}$$

We solve this linear ordinary differential equation of second order with the exponential ansatz

$$\delta c(t) = S_1 e^{\mathrm{i}\omega t}. \tag{3.21}$$

Note that the outgoing angular frequency ω equals the incoming modulation frequency, but the transferred modulation amplitude S_1 might be different to A_0. We put the ansatz (3.21) in the oscillator Eq. (3.20) and find for the transferred intensity

$$|S_1(\omega)|^2 = \frac{A_0^2}{(\det(\underline{\underline{A}}) - \omega^2)^2 + (\omega \mathrm{tr}(\underline{\underline{A}}))^2}.$$

This equation is called modulation transfer function.
A characteristic quantity in information theory is the *half power point* at which the output intensity (or *power*) has dropped to half of its reference value. The ratio of two intensity levels, the modulated signal intensity $|S_1(\omega)|^2$ and the reference level

$$|S_1(0)|^2 = \frac{A_0^2}{\det(\underline{\underline{A}})},$$

is expressed via the *bel* scale

$$10 \lg \left(\frac{|S_1(\omega_{3db})|^2}{|S_1(0)|^2} \right) = 10 \lg \left(\frac{1}{2} \right) \approx 3,01 \,\mathrm{dB},$$

where ω_{3db} is the cutoff angular frequency and the intensity drop by $1/2$ corresponds to an approximately $-3\,\mathrm{dB}$ level. The aim is to find an analytical expression for the cutoff frequency $f_{3db} = \omega_{3db}/2\pi$, so we start with

$$\begin{aligned} |S_1(\omega_{3db})|^2 &:= \frac{1}{2}|S_1(0)|^2 \\ &\Longleftrightarrow \\ 0 &= \omega_{3db}^4 + \omega_{3db}^2(\mathrm{tr}^2(\underline{\underline{A}}) - 2\det(\underline{\underline{A}})) - \det^2(\underline{\underline{A}}) \end{aligned}$$

and solve this equation for

$$\omega_{3db}^2 = -\frac{\mathrm{tr}^2(\underline{\underline{A}}) - 2\det(\underline{\underline{A}})}{2} + \sqrt{\left(\frac{\mathrm{tr}^2(\underline{\underline{A}}) - 2\det(\underline{\underline{A}})}{2} \right)^2 + \det^2(\underline{\underline{A}})}.$$

We substitute $\omega_0^2 = \omega_{RO}^2 + \Gamma_{RO}^2$ and write the cutoff frequency as

$$f_{3db} = \frac{1}{2\pi} \sqrt{\omega_0^2 - 2\Gamma_{RO}^2 + \sqrt{(2\Gamma_{RO}^2 - \omega_0^2)^2 + \omega_0^4}}. \tag{3.22}$$

In order to compare the latter equation with numerical results, the simulations with the rate equation are depicted in the Appendix A.5.

4 Dynamics of solitary laser

The dynamics of a solitary laser device shall be well studied in order to find convenient parameter sets for further investigations. There is also a wide variety of interesting effects to look at. We will encounter the effects of section 3 like relaxation oscillations, Rabi oscillations, overdamped laser turn-ons, limit cycles and chaos. These phenomena will be visualized with time series, phase space and bifurcation diagrams and will be compared with the eigenvalue spectra, what will give us the opportunity to assess our systems.
Basically laser models are divided into three subclasses [ARE84], which are differentiated by the values of their timescales:

- Class A: $\gamma \approx \frac{1}{T_1(w_e)} \gg \kappa$,
- Class B: $\gamma \gg \kappa \geq \frac{1}{T_1(w_e)}$,
- Class C: $\gamma \approx \frac{1}{T_1(w_e)} \approx \kappa$.

The *class A* lasers show up the most stable behaviour among the laser classes. The definition shown above says the photon lifetime κ^{-1} is much greater than other timescales in the system, which is true for high Q cavities. The equations for inversion and polarization, characterized by T_1 and γ^{-1}, can be eliminated adiabatically, as their change is fast enough to let the system dynamics unaffected. This results in a single photon differential equation and the polarization and inversion pass over to a steady state. This system is not able to have relaxation oscillations, so we will see overdamped turn-ons without oscillations. Typical class A lasers are Ar-ion or He-Ne lasers at certain wavelengths.

In the *class B* case, where the inversion decay T_1^{-1} gets smaller than the photon decay κ, while the polarization stays fast, the system is able to have relaxation oscillations. This case is described by a two-variable rate equation system (2.37) and (2.38). This laser class is intrinsically stable, as a second laser threshold does not exist. However external perturbations like optical self-feedback or optical injection can destabilize the laser emission. Examples for Class B lasers are CO_2 lasers and solid state lasers.

The full system with three degrees of freedom, described by the Bloch Eqs. (2.34) to (2.36), corresponds to a *class C* laser. This is true if all timescales are of the same order of magnitude and have to be considered equally. The second laser threshold can be positive and possibly be reached for a certain pump, what shows up as pulsations or unstable oscillations. Examples for Class C lasers are NH_3 lasers, Ne-Xe lasers, He-Ne lasers and the most infrared gas lasers.
Note that each oscillation mode of a laser material can own a different stability character, as losses and gain are wavelength-dependent.

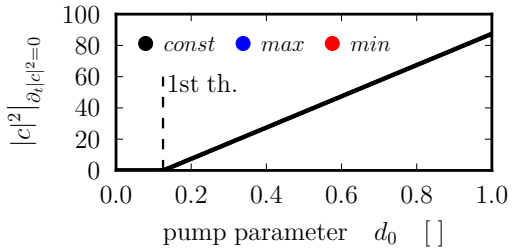

(a) Without scattering rates, without spontaneous Emission.

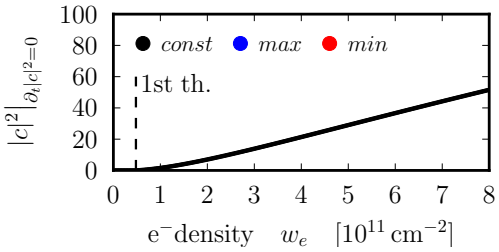

(b) With scattering rates, without spontaneous Emission.

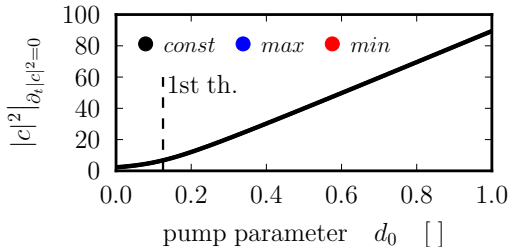

(c) Without scattering rates, with spontaneous Emission.

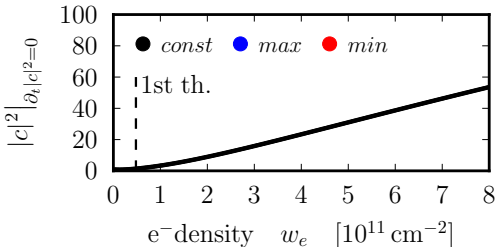

(d) With scattering rates, with spontaneous Emission.

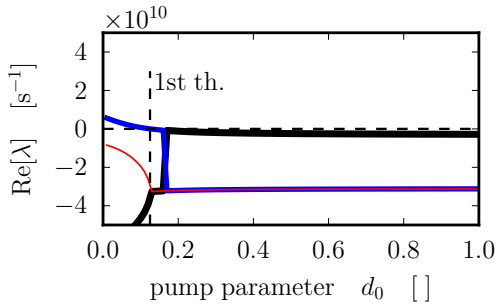

(e) Real parts corresponding to (a).

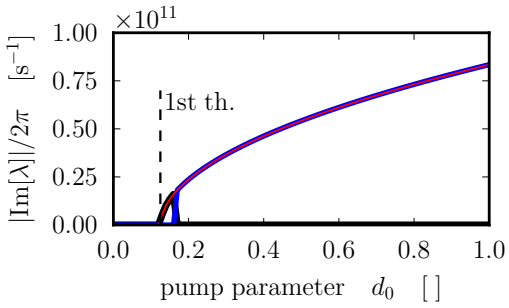

(f) Imaginary parts corresponding to (a).

$T_1^{-1} = 2 \cdot 10^{11}\,\mathrm{s}^{-1}, \quad \kappa = 10^{10}\,\mathrm{s}^{-1}, \quad \gamma = 2 \cdot 10^{11}\,\mathrm{s}^{-1}, \quad \tau_{sp}^{-1} = 10^{10}\,\mathrm{s}^{-1}, \quad G = 10\,\mathrm{cm}^{-1}$

Figure 4.1: Bifurcation diagrams (a-d) and eigenvalues (e-f) of a class A laser simulated with the Bloch equations. The dashed vertical line marks the first laser threshold.

4.1 Class A laser

In order to get an overview of the system's behaviour, we start with some characteristic issues of a class A laser. This is the simplest case and thus a good way to understand basic effects. We can see in Fig. 4.1a a regular transcritical bifurcation with a second order nonequlibrium phase transition. Without considering scattering rates and spontaneous emission, a lasing steady state solution branch bifurcates from a nonlasing state exactly at the first laser threshold, determined by Eq. (3.17). This behaviour changes as scattering

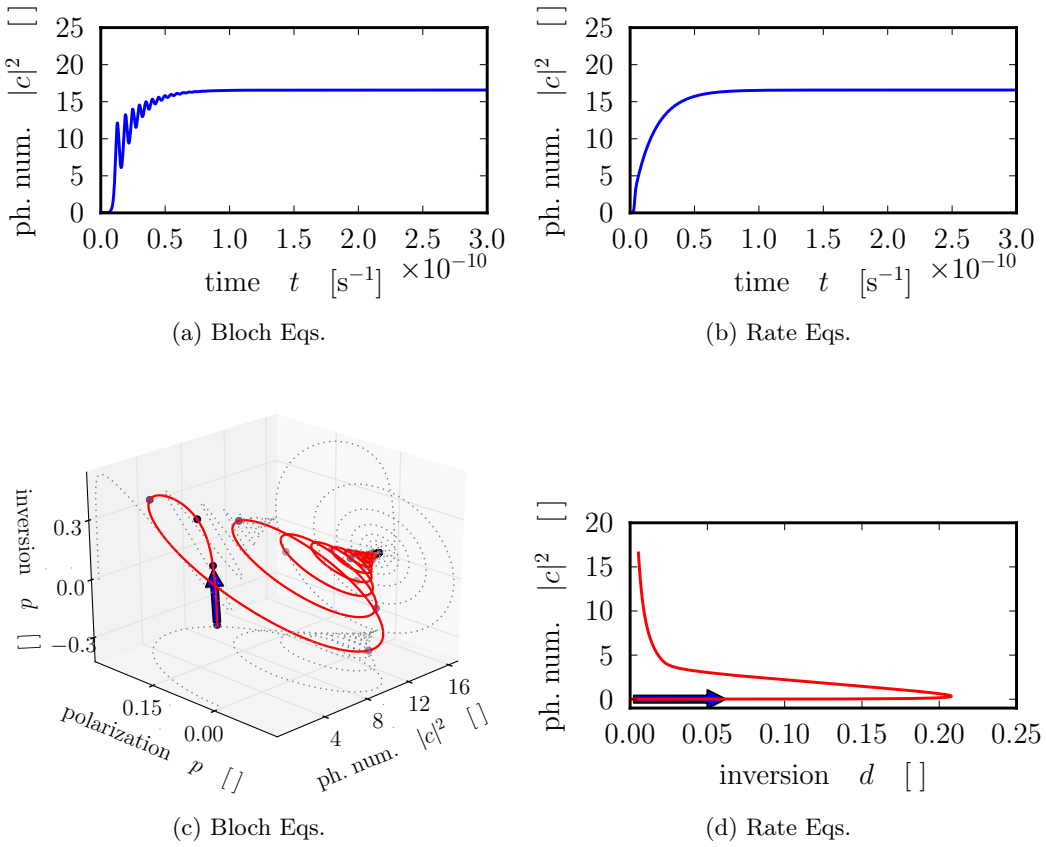

(a) Bloch Eqs.

(b) Rate Eqs.

(c) Bloch Eqs.

(d) Rate Eqs.

$T_1^{-1} = 10^{11}\,\mathrm{s}^{-1}$, $\kappa = 2 \cdot 10^{10}\,\mathrm{s}^{-1}$, $\gamma = 10^{11}\,\mathrm{s}^{-1}$, $G = 700\,\mathrm{cm}^{-1}$, $d_0 = 1$

Figure 4.2: Time series and phase spaces of a class A laser simulated with the Bloch and rate equations, respectively, without scattering rates.

rates are considered in Fig. 4.1b. Laser emission still starts at the first laser threshold, but the lasing solution branch is nonlinear. This is because the net pump $d_0(w_e)$ increases nonlinear with the electron density in the wetting layer w_e, as we can see in Fig. 2.3. In addition w_e effects the inversion lifetime $T_1(w_e)$ which of course has influence on the photon amplitude Eq. (2.34). The second order phase transition becomes destroyed in Fig. 4.1c by the effect of spontaneous emission. The scattering rates are not considered here in order to understand the influence of spontaneous emission. The stable photon emission can be observed before the first laser threshold is reached, even without any pumping if the rate of spontaneous emission is high enough. If we extrapolate the linear part of the solution to the x-axis, we end up at the first laser threshold, which is not true for Fig. 4.1b. Fig. 4.1d shows a mixture of the influence of both spontaneous emission and scattering rates, which we are confronted with in most of the further simulations.
The corresponding eigenvalues are depicted in Fig. 4.1(e,f) and give information about this behaviour. The zero-crossing of a single real part of the eigenvalues marks the first laser

threshold. As soon as two real parts coalesce, an imaginary part appears. The two positive imaginary parts in Fig. 4.1f correspond to the two smallest real parts in Fig. 4.1e. The greatest real part is most unstable and there is no positive imaginary complement. Hence the oscillation in the complex plane is damped away by the smallest real parts.
In general the turn-on of class A lasers is overdamped, which means no relaxation oscillation occurs. No matter what initial conditions are set, the laser emission approaches asymptotically the steady state, which is a stable node (Fig. 3.1). Fig. 4.2 shows a comparison between the rate and Bloch equations without scattering rates and spontaneous emission and for an increased gain G. In Fig. 4.2(a,c) we see fast oscillations during the laser turn-on, which can be associated with Rabi oscillations with an oscillation frequency of about

$$f_\Omega = \frac{\boldsymbol{\mu} \cdot \boldsymbol{E}}{2\pi\hbar} = \frac{|g|c}{2\pi} \approx 0,1\,\mathrm{ps}^{-1}$$

for the above case. They only occur in the Bloch regime, as adiabatic elimination of the polarization prevents oscillations in this direction, and the oscillation amplitude increases with the gain. The rate equations in Fig. 4.2(b,d) are subjected to the same set of parameters and show the same steady state, but without Rabi oscillations during the turn-on. In a strict sense the Bloch case shows whether a class A nor a class B system. These oscillations are due to the polarization equation, as the dynamic of relaxation oscillations would be grasped by the rate equations as well. To conclude this time series require the dynamics of photon amplitude and polarization, whereby a class A laser is restricted to the photon equation.
The next subsection will clarify the difference between the occurrence of Rabi and relaxation oscillations.

4.2 Class B laser

The correspondence between the Bloch and the rate equations is given by a class B laser system. The model can basically be described by two equations and both models, either containing two or three equations, provide the same results. The high polarization decay γ makes the description of polarization dynamics redundant. The bifurcation in Fig. 4.3a looks qualitatively similar to the class A case of Fig. 4.1a, but the route to the steady state changes. The photon number is less due to a smaller inversion decay T_1^{-1}. We see in Fig. 4.3(b,c), that the eigenvalues reveal the fixed point character, which changes from a stable node to a stable focus. The significant difference between these eigenvalues to those of the class A case in Fig. 4.1(e,f) is that the greatest real parts correspond to the positive imaginary parts. This time the system is able to oscillate in the complex plane and is not overdamped. The time series in Fig. 4.3(d-g) show relaxation oscillations in the Bloch and rate regime, respectively. We see that a system with a high γ needs only two equations to grasp the full dynamics. The frequency of the relaxation oscillations is about

$$f_{ro} = \left.\frac{\mathrm{Im}[\lambda]_{max}}{2\pi}\right|_{d_0=1} \approx 2,4\,\mathrm{ns}^{-1},$$

where $\mathrm{Im}[\lambda]_{max}$ is the greatest of the imaginary parts depicted in Fig. 4.3c.

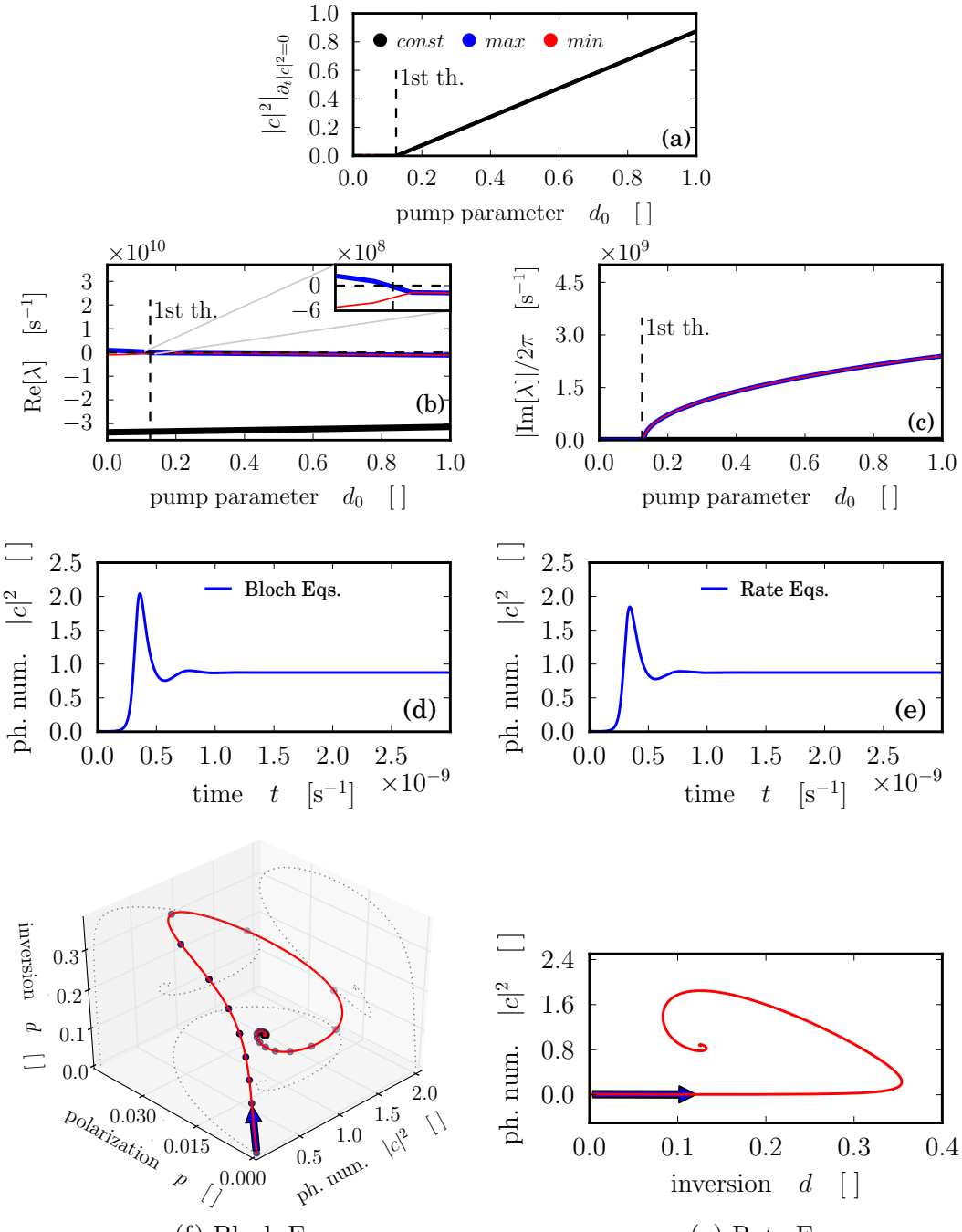

(f) Bloch Eqs.. (g) Rate Eqs..

$T_1^{-1} = 2 \cdot 10^9\,\mathrm{s}^{-1}, \quad \kappa = 10^{10}\,\mathrm{s}^{-1}, \quad \gamma = 2 \cdot 10^{11}\,\mathrm{s}^{-1}, \quad G = 10\,\mathrm{cm}^{-1}$

Figure 4.3: Bifurcation diagram (a), the corresponding eigenvalues (b-c), time series (d-e) and phase spaces (f-g) of a class B laser simulated without scattering rates and without spontaneous emission. Bloch equations. In Fig. (d-g) the pump parameter is set to $d_0 = 1$. The dashed vertical line marks the first laser threshold.

4.3 Class C laser

A system in which all timescales are of the same order of magnitude, so that dynamics of inversion, polarization and photon number have to be considered, is said to be a class C laser. Here the system dynamics cannot be grasped by two equations, as the system has three degrees of freedom. This fact can obviously be seen in Fig. 4.4(a,b). Both graphics are subjected to the same parameter set and show that chaotic behaviour is not captured

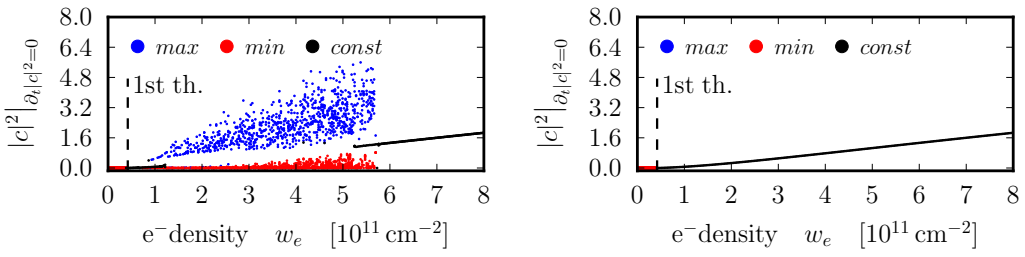

(a) Bloch Eqs..

(b) Rate Eqs..

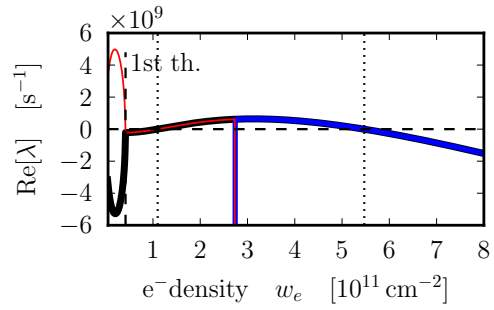

(c) Real parts corresponding to (a).

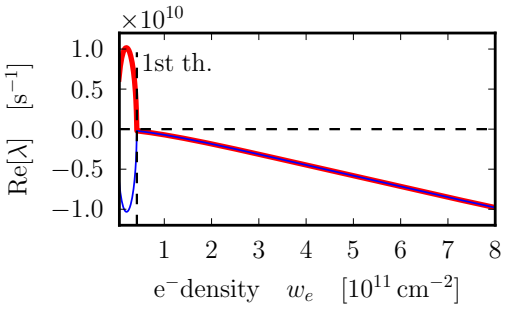

(d) Real parts corresponding to (b).

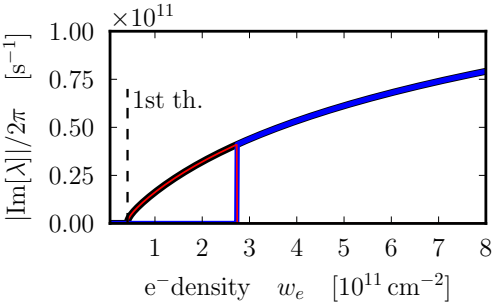

(e) Imaginary parts corresponding to (a).

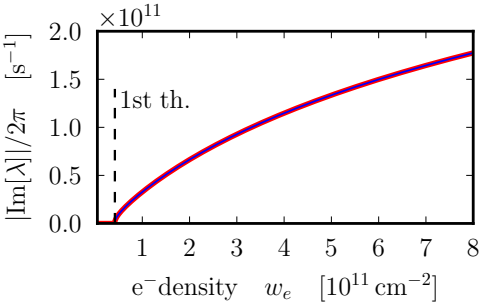

(f) Imaginary parts corresponding to (b).

$$\kappa = 3 \cdot 10^{11}\,\mathrm{s}^{-1}, \quad \gamma = 10^{11}\,\mathrm{s}^{-1}, \quad G = 700\,\mathrm{cm}^{-1}$$

Figure 4.4: Bifurcation diagrams (a-b) and eigenvalues (b-c) of a class C laser simulated with the Bloch and rate equations, with scattering rates and without spontaneous emission. The dashed vertical line marks the first laser threshold and the dotted vertical lines mark the the zero-crossings.

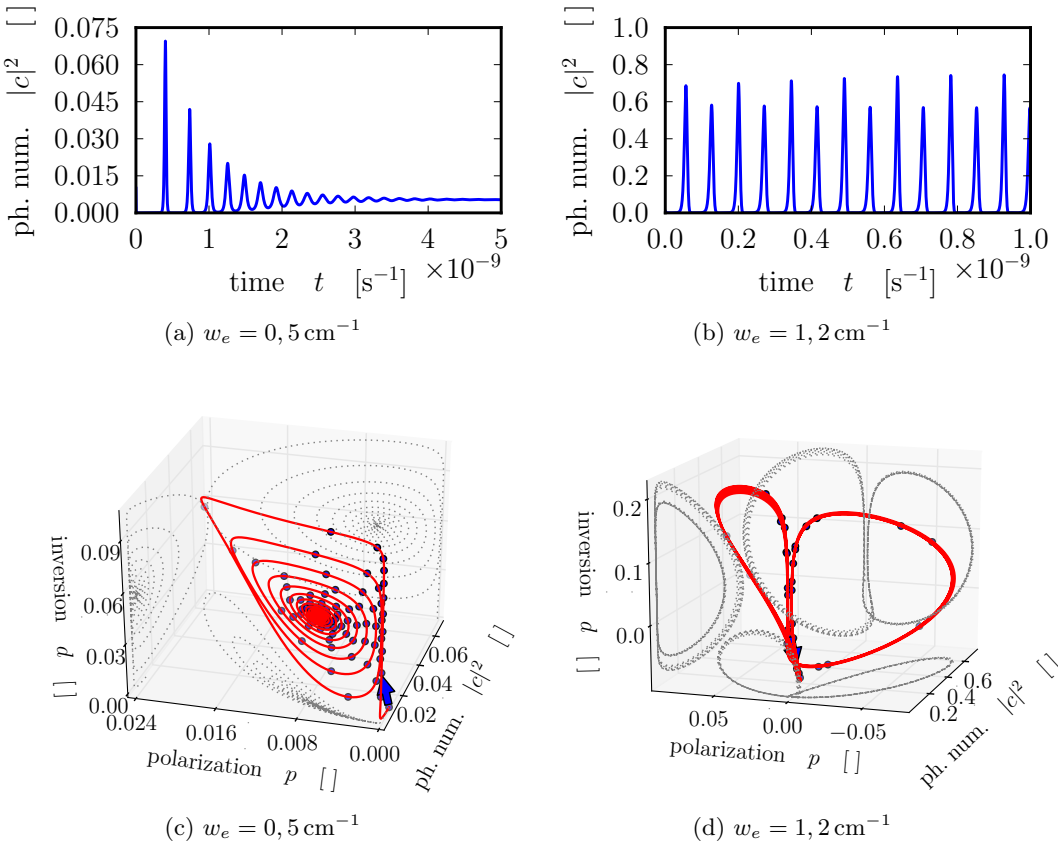

(a) $w_e = 0,5\,\mathrm{cm}^{-1}$ (b) $w_e = 1,2\,\mathrm{cm}^{-1}$

(c) $w_e = 0,5\,\mathrm{cm}^{-1}$ (d) $w_e = 1,2\,\mathrm{cm}^{-1}$

$$\kappa = 3 \cdot 10^{11}\,\mathrm{s}^{-1}, \quad \gamma = 10^{11}\,\mathrm{s}^{-1}, \quad G = 700\,\mathrm{cm}^{-1}$$

Figure 4.5: Time series and phase space of a class C laser simulated with the Bloch equations, respectively, with scattering rates and without spontaneous emission. These graphics correspond to Fig. 4.4a.

by a two-equation system (Fig. 4.4b). Regions which are chaotic in the Bloch regime show up as stable regions in the rate regime. The real parts in Fig. 4.4c corresponding to the Bloch system show three zero-crossings. A positive real part together with a positive imaginary part leads to an uncontrolled increase of the perturbance in the direction of the corresponding eigenvector. Positive real and imaginary parts do not occur in the rate system (Fig. 4.4d).

The parameter set chosen in Fig. 4.4a provides a variety of phenomena. The time series and their visualizations in phase space are shown in Fig. 4.5 and Fig. 4.6. An exemplary time series for laser spiking is depicted in Fig. 4.5(a,c). This nonlinear effect show up as chaotic pulsations while the photon number approaches zero in the interspike intervals. These are strongly deformed oscillations far from the fixed point. Hence the description via linearized system (around the fixed point) is impossible. We see a smooth transition from laser spiking to relaxation oscillations, which again is a linear phenomenon and can

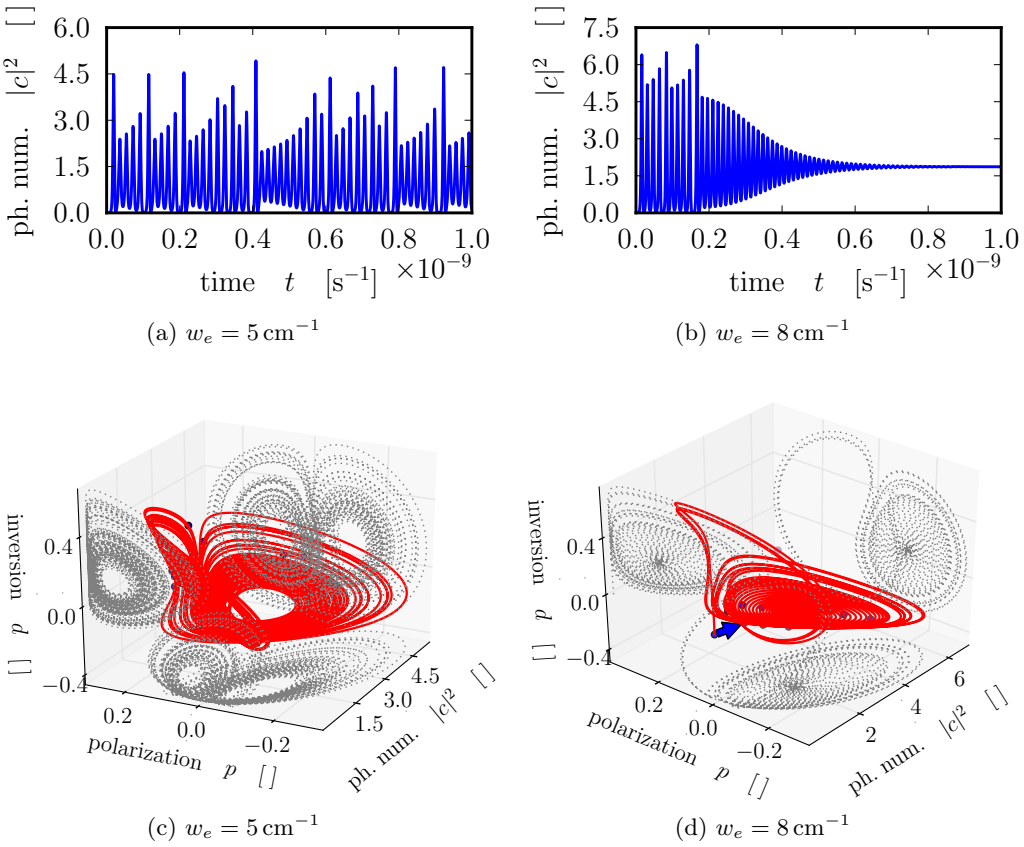

(a) $w_e = 5\,\mathrm{cm}^{-1}$ (b) $w_e = 8\,\mathrm{cm}^{-1}$

(c) $w_e = 5\,\mathrm{cm}^{-1}$ (d) $w_e = 8\,\mathrm{cm}^{-1}$

$$\kappa = 3 \cdot 10^{11}\,\mathrm{s}^{-1}, \quad \gamma = 10^{11}\,\mathrm{s}^{-1}, \quad G = 700\,\mathrm{cm}^{-1}$$

Figure 4.6: Time series and phase space of a class C laser simulated with the Bloch equations, with scattering rates and without spontaneous emission. These graphics correspond to Fig. 4.4a.

be well explained with the eigenvalues (Fig. 4.4(c,e)) of a linearized system.
For a certain pump a transition from a stable focus to a stable limit cycle (unstable fixed point but asymptotic orbitally stable trajectory) and an unstable focus occurs. This transition scheme is called supercritical Hopf bifurcation of limit cycles. The unstable focus and the limit cycle coexist, what can be seen in Fig. 4.4a, where the stable solution branch reaches slightly into the unstable region beyond the zero-crossing of the corresponding real parts. Shortly after this transition a twin limit cycle occurs in Fig. 4.5(b,d).
We see in Fig. 4.4a that the pulse strengths of the twin limit cycle move apart until a chaotic behaviour starts at a certain pump. This chaos can be seen in Fig. 4.6(a,c), where every time the laser emission tries to stabilize after each spike, the oscillation increases steadily.
Fig. 4.6(b,d) shows a region, where the strongly nonlinear oscillations become weakly damped relaxation oscillations and the system finally moves into a steady state.

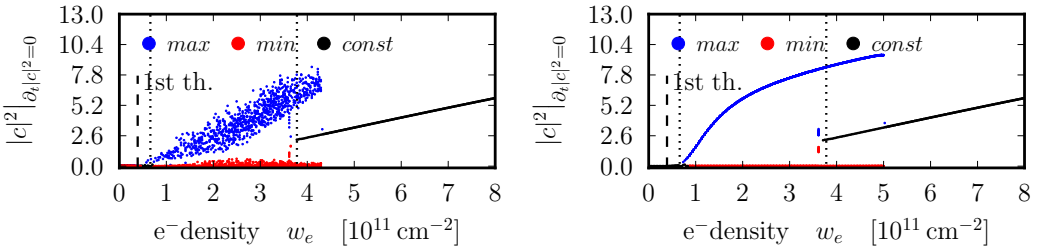

(a) Without spontaneous emission.

(b) With spontaneous emission.

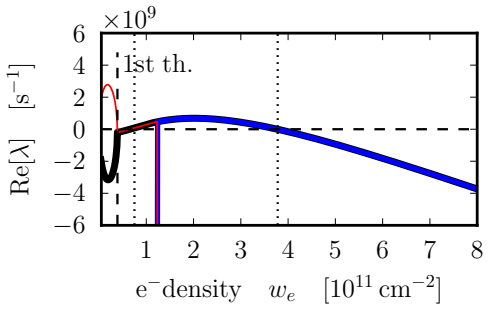

(c) Real parts corresponding to (a).

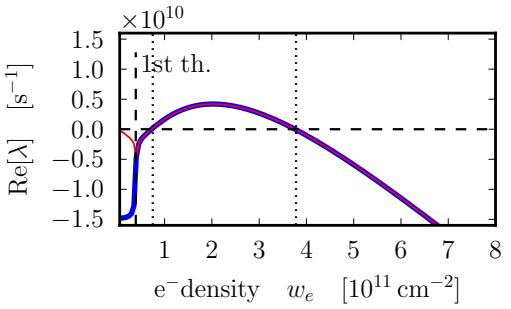

(d) Real parts corresponding to (b).

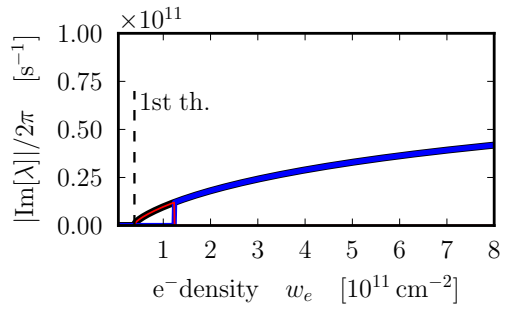

(e) Imaginary parts corresponding to (a).

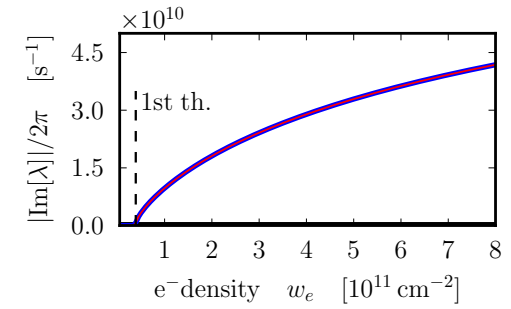

(f) Imaginary parts corresponding to (b).

$$\kappa = 10^{11}\,\mathrm{s}^{-1}, \quad \gamma = 10^{10}\,\mathrm{s}^{-1}, \quad \tau_{sp}^{-1} = 10^{8}\,\mathrm{s}^{-1}, \quad G = 700\,\mathrm{cm}^{-1}$$

Figure 4.7: Bifurcation diagrams (a-b) and eigenvalues (b-c) of a class C laser simulated with the Bloch equations with scattering rates. Comparison of a system with (b,d,f) and without (a,c,e) spontaneous emission. The dashed vertical line marks the first laser threshold and the dotted vertical lines mark the the zero-crossings.

As a final step of this section we want to compare the Bloch system with (Fig. 4.7a) and without (Fig. 4.7b) spontaneous emission. Obviously spontaneous emission can have a stabilizing effect on laser emission. Again we can observe the bistability in both bifurcation diagrams. To determine the exact types of bifurcation a path tracking analysis would be an advantage, as unstable regions cannot be grasped easily. In a multi stable system, the solution depends strongly on the initial conditions. If one start the solution algorithm with

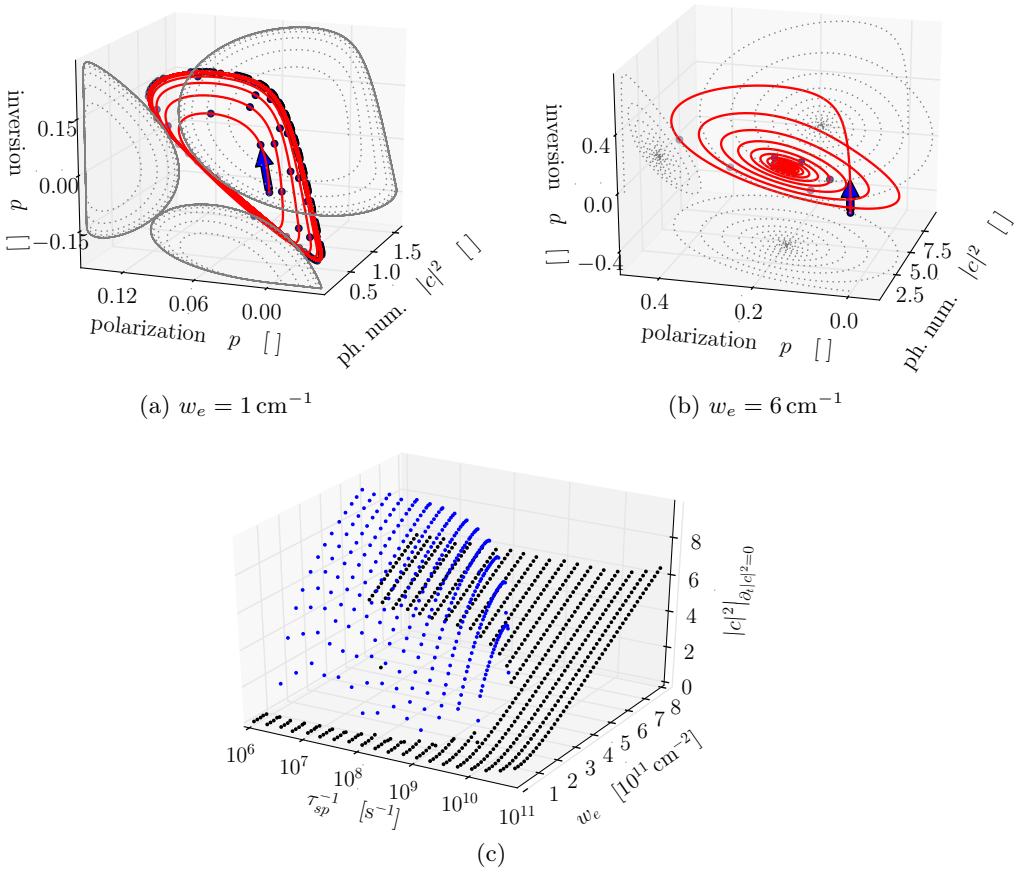

(a) $w_e = 1\,\mathrm{cm}^{-1}$ (b) $w_e = 6\,\mathrm{cm}^{-1}$

(c)

$$\kappa = 10^{11}\,\mathrm{s}^{-1}, \quad \gamma = 10^{10}\,\mathrm{s}^{-1}, \quad \tau_{sp}^{-1} = 10^{8}\,\mathrm{s}^{-1}, \quad G = 700\,\mathrm{cm}^{-1}$$

Figure 4.8: (a,b) Phase space of a class C laser simulated with the Bloch equations. (c) Bifurcation diagram for varied spontaneous emission rates τ_{sp}. (a,b,c) correspond to Fig. 4.7b.

a varied control parameter but with the initial conditions of a stable solution branch, one can end up with a stable emission even if the fixed point is unstable. This is the reason, why a parameter up and down sweep differ from each other. Both solution branches are of interest and are plotted in the bifurcation diagrams. The curves in Fig. 4.7b let us assume a limit cycle bifurcation by condensation of paths [SCH87]. The eigenvalues with spontaneous emission show an increased damping with a decreased imaginary part, which together cause the stabilization. Exemplary phase trajectories corresponding to Fig. 4.7b show a clean limit cycle (Fig. 4.8a) and smooth relaxation oscillations (Fig. 4.8b). Fig. 4.8c shows the bifurcation development for an increased spontaneous emission rate. We notice a stabilization of the chaotic behaviour towards a limit cycle up until steady state emission. For low spontaneous emission rates the system leaves the bad cavity region with increasing the electron density in the wettinglayer w_e, which is illustrated in Fig. 5.1. The effect of

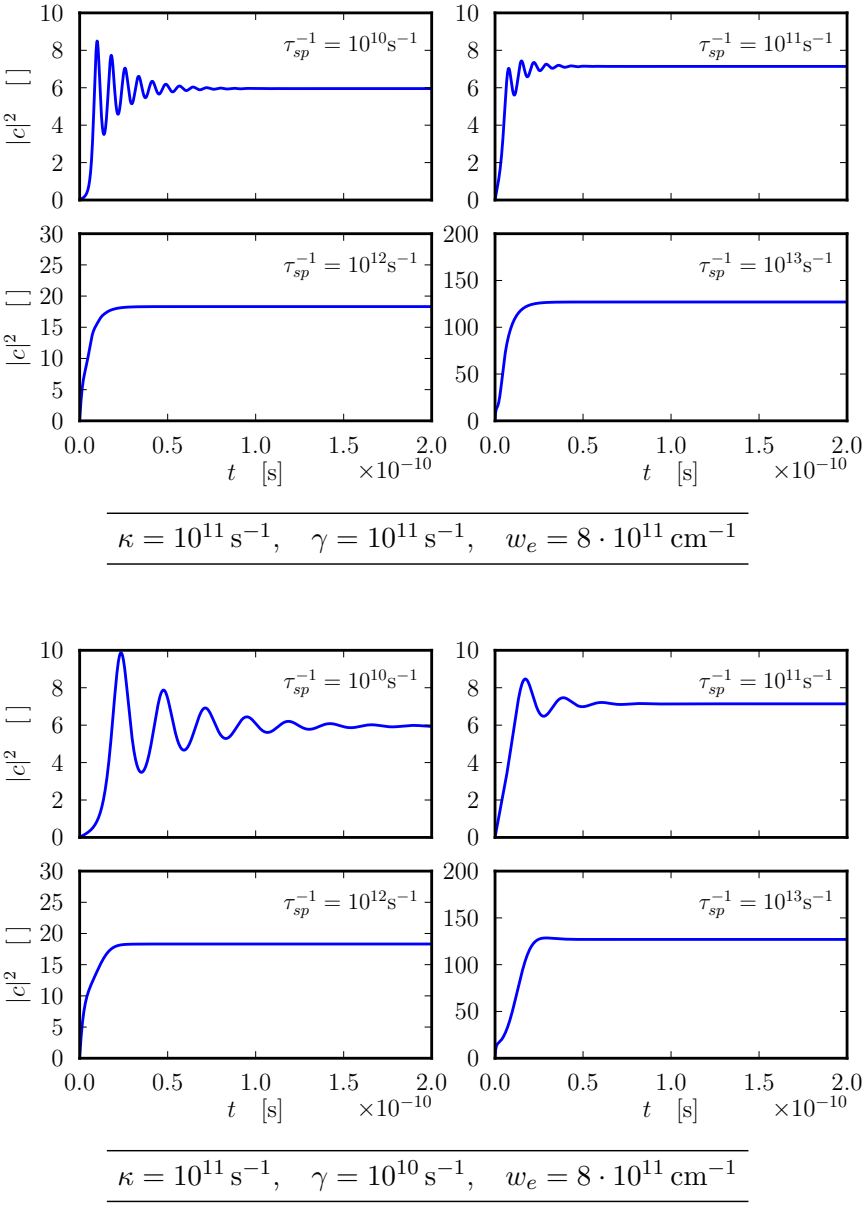

Figure 4.9: Time series with varied spontaneous emission rates, simulated with Bloch equations.

stabilization due to spontaneous emission is of great interest, as it changes the character of the expected light emission of the corresponding laser class. Thus a class B or C laser can emit free of relaxation oscillations. We will illustrate this by means of exemplary time series in Fig. 4.9 for two different γ-values. A smaller γ obviously lowers the imaginary part (Fig. 4.9 bottom). A rate for spontaneous emission counters cavity losses at a certain point, which finally entails a better cavity. The overdamping of relaxations oscillations is caused by decreasing real parts and further takes effect on the modulation behaviour, investigated in the following section.

5 Small signal response

This chapter deals with the numerical approach of the small signal response we introduced in section 3.4 on page 28. The increasing complexity of our equation systems requires numerical investigations and makes analytical approaches unfavourable. We aim to examine class C lasers in the *good cavity* region, where the Bloch equations lead to different results than the rate equations. We will shortly show a correspondence between the rate and Bloch regime for high polarization decay rates γ. With this intension we first need to find a convenient parameter set, we can use for both models, the toy model without scattering rates and without spontaneous emission and the full model with scattering rates and spontaneous emission. In the toy model we simulate the spontaneous emission effect by controlling the inversion decay rate T_1^{-1}. This shows up as an increased, unspecified decay of the inversion, what may happen due to spontaneous emission. After studying the toy model we will intensively examine the full model, where the spontaneous emission is implemented as a standalone rate and the inversion decay $T_1^{-1}(w_e)$ is set by the electron density in the wettinglayer w_e.

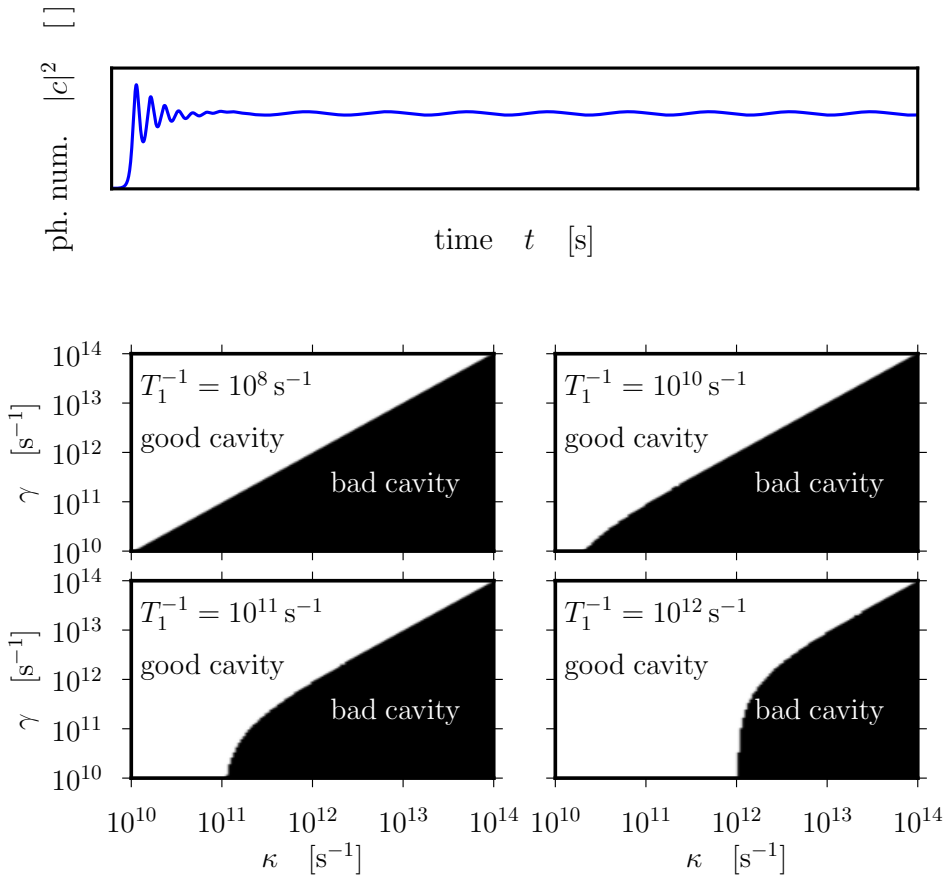

Figure 5.1: Exemplary time series with modulated pump current, where modulation amplitude is strongly increased due to visualization reasons. Bad and good cavity regions for a certain parameter set calculated with Eq. (3.19).

In order to find a parameter set we can use in both models, we take a look at Fig. 5.1. We see in Fig. 2.3 on page 14 the pump implies an inversion decay rate of

$$10^9\,\mathrm{s}^{-1} \lesssim T_1^{-1}(w_e) \lesssim 2 \cdot 10^{11}\,\mathrm{s}^{-1}. \tag{5.1}$$

As long as we take the pump as a control parameter, we have to choose the inversion decay γ greater than the photon decay κ in order to avoid chaotic emissions within the bad cavity region. In a later section we will examine a parameter room without controlling the pump, so we can consider an inversion decay slower than the photon decay.
The comparability between the graphs of the toy model and the full model is restrictedly possible, whereby a transformation is depicted in Appendix A.7.

5.1 The toy model

In the first numerical modulation response simulations the inversion decay T_1^{-1} and the pump d_0 are set as control parameters, while the inversion and photon decay rates are varied for each simulation. The following simulations are based on the toy model of Bloch and rate Eqs. (2.34) to (2.36) and (2.37) to (2.38) without spontaneous emission and without scattering rates, respectively. The inversion decay rate has at least to be ranged according to Ineq. (5.1). We increase this range by several orders of magnitude in order to get a wider overview of the system's behaviour.
It is a well known fact that resonances appear in time series with modulated pump currents at the relaxation oscillation frequency, given by the imaginary part

$$f_{RO,max} = \frac{|\mathrm{Im}_{\max}(\lambda_i)|}{2\pi}$$

of the less damped Eigenvalue of the corresponding linearized system. The less damped Eigenvalue is the one with the greatest real part $\Gamma_{RO,max}$. If and how strong this resonance appears depends on the value of the real part, as these resonances can also be overdamped. In the last chapter we have seen Rabi frequencies appear only in the Bloch system. This is not possible in the rate system, because of the lack of polarization dynamics cause the loss of this necessary degree of freedom. We can see in Fig. 4.2c Rabi oscillations are prevailing in the polarization-inversion-plane, while relaxation oscillations are prevailing in the photon-inversion-plane (Fig. 4.3c). In the last mentioned case the polarization has no additional influence on dynamics what can be seen in Fig. 4.3d. That means the time series of Bloch and rate equations are then equivalent and have the same steady state solution. Hence we want to examine how the influence of polarization dynamics show up in the small signal response. At this point we do not know whether differences in the systems can be explained by the resonances with the Rabi frequency or with the relaxation oscillation frequency, or both.
Therefore we choose two exemplary parameter sets with $\kappa = 10^{11}\,\mathrm{s}^{-1}$ in Fig. 5.2 and $\kappa = 10^{12}\,\mathrm{s}^{-1}$ in Fig. 5.3 and vary γ, respectively. In these figures we show a composition of the cutoff, Rabi and relaxation oscillation frequencies and the real parts. In addition we depict modulation transfer curves in Fig. 5.4 to see how the system actually behaves at certain exemplary regions in parameter space.

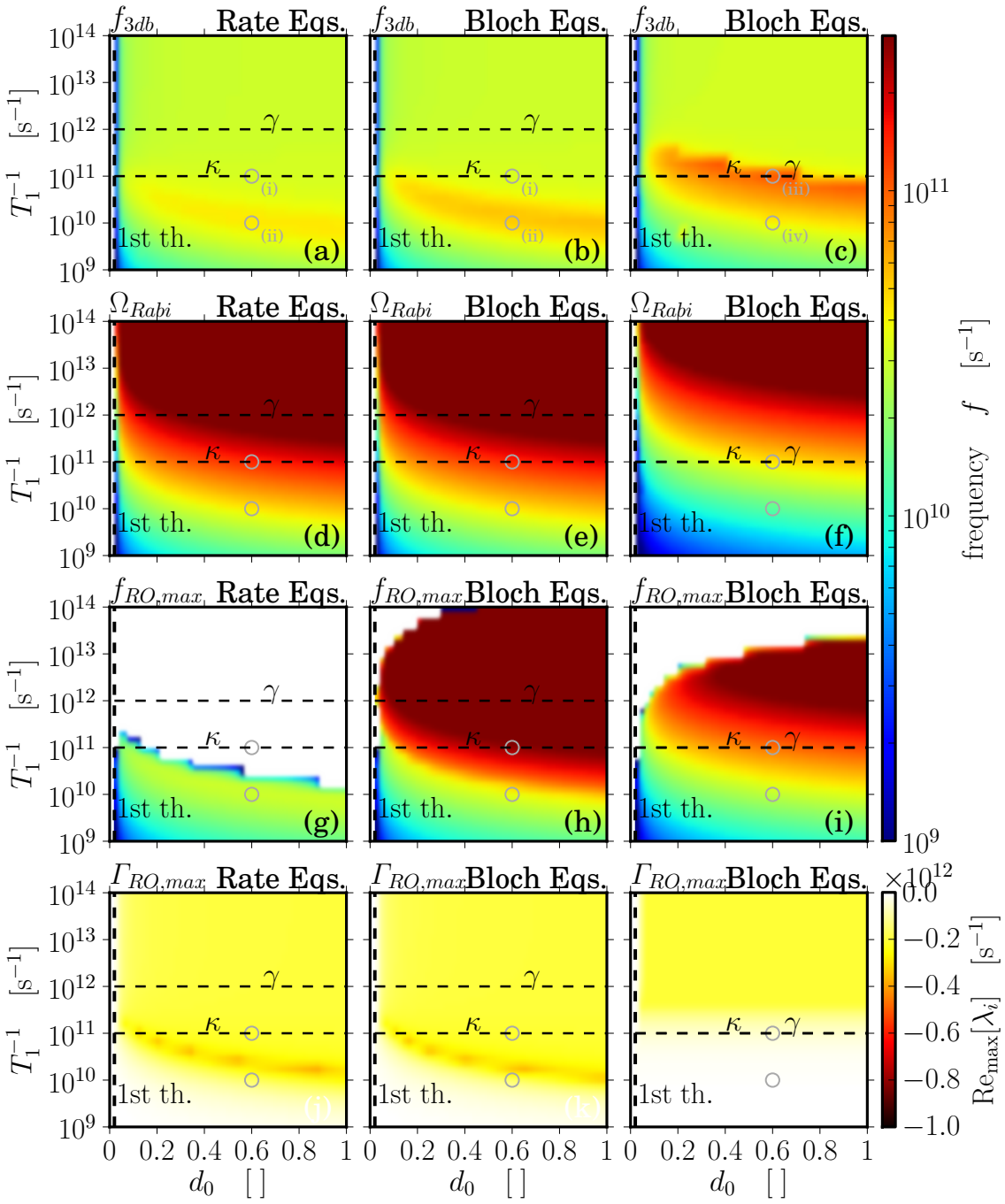

Figure 5.2: Comparison of rate (a,d,g,j) and Bloch (b,c,e,f,h,i,k,l) equations for a given $\kappa = 10^{11}\,\mathrm{s}^{-1}$, where (a,b,c) show the cutoff frequency f_{3db}, (d,e,f) the Rabi frequency Ω_{Rabi}, (g,h,i) the maximum real part $\Gamma_{RO,max}$ of the linearized system and (j,k,l) its corresponding imaginary part $f_{RO,max}$. The control parameters are the inversion pump d_0 and the inversion decay T_1^{-1}, respectively. The grey circles with small roman numbers refer to the modulation transfer curves in Fig. 5.4. The dashed vertical line marks the first laser threshold. The dashed horizontal lines mark the values of the photon decay κ and the polarization decay γ.

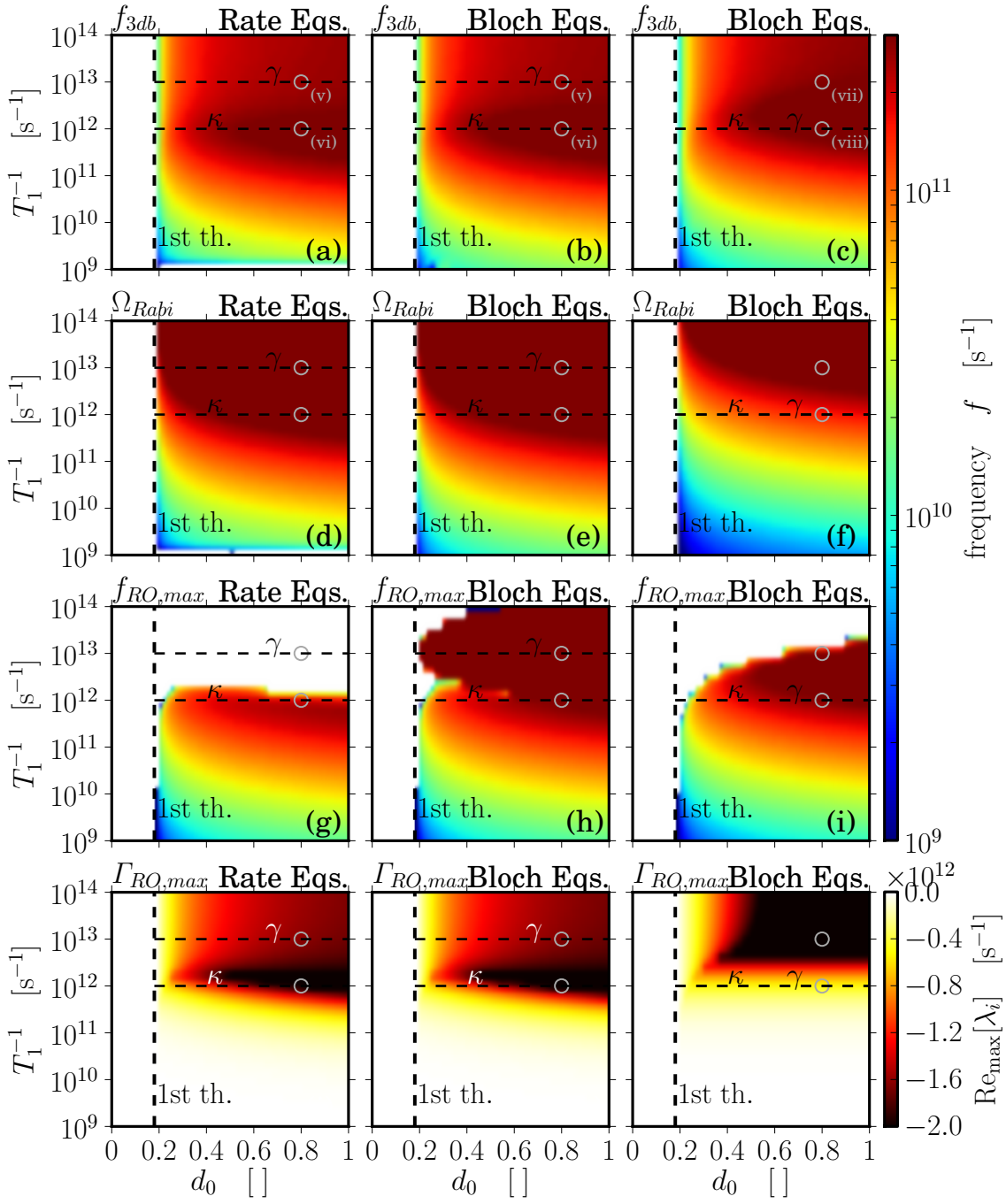

Figure 5.3: Comparison of rate (a,d,g,j) and Bloch (b,c,e,f,h,i,k,l) equations for a given $\kappa = 10^{12}\,\mathrm{s}^{-1}$. Figure caption is identical to Fig. 5.2.

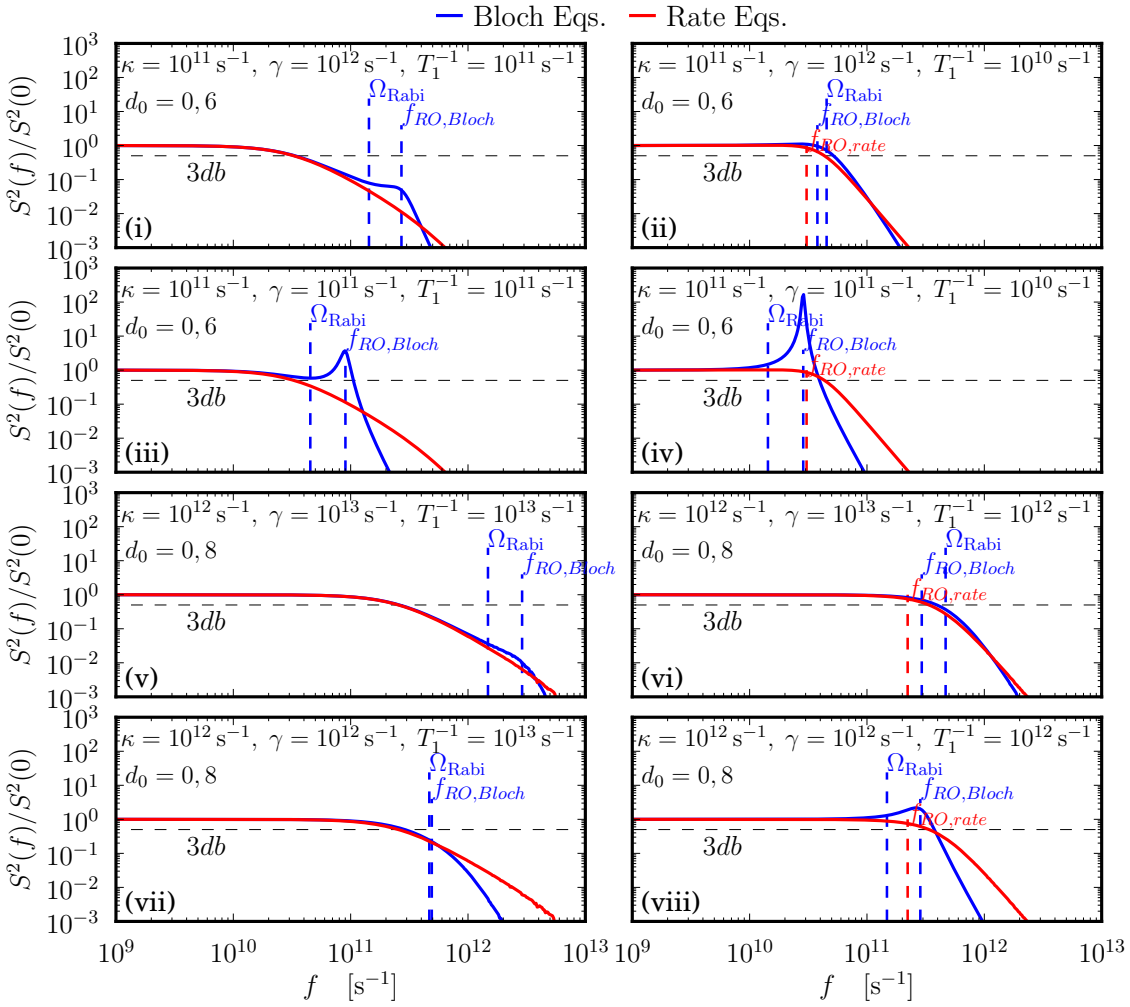

Figure 5.4: Normalized transferred small signal intensities versus the modulation frequency f for rate and Bloch equations. The parameters are noted at the top of each subfigure, but can also be concluded from the corresponding circles in Fig. 5.2 and 5.3, marked by the small roman numbers (i-viii). The corresponding Rabi Ω_{Rabi} and relaxation oscillation frequencies of the Bloch $f_{RO,Bloch}$ and rate $f_{RO,rate}$ equations are marked with dashed lines.

We start with the description of Fig. 5.2. We see one column for the rate equations and two columns for the Bloch equations. The two columns for the Bloch equations differ in their γ values. First of all it is important to create a correspondence between the Bloch and the rate system. Thus we compare the first and second column and recognize that we gain almost identical results in the rate and Bloch system with a high polarization decay γ. We expect the adiabatic elimination of the polarization dynamics is valid for high γ values, so in this case the rate equations can be applied without hesitation. This is also the parameter region which is already well studied. The rate system can fail under certain circumstances, if all system time scales are of the same order of magnitude (class C regime).

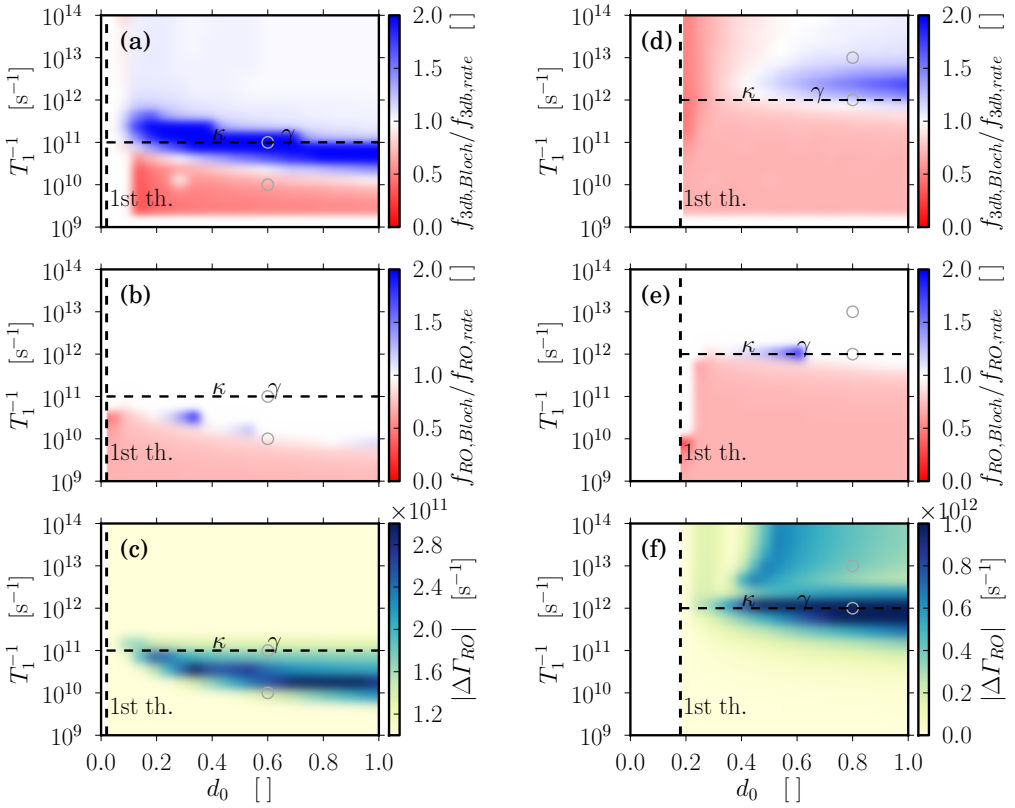

Figure 5.5: Relative quantities, where (a,b,c) correspond to Fig. 5.2 and (d,e,f) to Fig. 5.3. (a,d) show the ratio between the cutoff frequencies of Bloch $f_{3db,Bloch}$ and rate $f_{3db,Bloch}$ equations, (b,e) the ratio of their relaxation oscillation frequencies $f_{RO,Bloch}/f_{RO,rate}$ and (c,f) the absolute difference between their maximum real parts $|\Delta\Gamma_{RO}| = |\Gamma_{RO,max,Bloch} - \Gamma_{RO,max,rate}|$.

We see in the third column the situation changes as soon as we decrease the polarization decay. Changing the γ value in the rate system does not entail a change (Fig. A.2 and Fig. A.3), whether in the modulation behaviour nor in the Eigenvalue spectra.
Comparing the relaxation oscillation frequencies $f_{RO,max}$ of rate and Bloch equations in Fig. 5.2(g,h) we see an additional Eigenvalue unequal to zero. Apart from this new Eigenvalue the structure of the Rabi oscillations, the maximum imaginary and real part in the parameter space is similar for a fast polarization decay. The resonances in the modulation transfer curves for the rate, as well as for the Bloch equations, occur at the relaxation oscillation frequency, as seen in Fig. 5.4. These transfer curves shall now be discussed. Comparing the Bloch and rate equations in Fig. 5.4i we recognize the resonance peak only in the Bloch system, what can be explained by the absence of the imaginary part in the rate system. The resonance has no effect on the cutoff frequency in Fig. 5.2, because the relaxation oscillation frequency is much greater than the cutoff frequency of the rate system, where the polarization dynamics are not considered. Thus in Fig. 5.4ii both Bloch and

rate system, have an existing imaginary part, but the Bloch system has a slightly greater real part, which means a less damped motion in direction of the eigenvector representing the relaxation oscillations. This discrepancy between the real parts in the Bloch and rate system increases with decreasing the polarization decay rate. The effect of the increased real part in the Bloch system (Fig. 5.2l) is a less damped resonance (Fig. 5.4(iii,iv)). In Fig. 5.4iii again only the Bloch system has a non-zero imaginary part, where in Fig. 5.4iv both systems have positive imaginary parts. The last mentioned figure shows no resonance peak in the rate system, because the real part is much smaller compared to the one of the Bloch system. The Bloch system shows a clear deviation - a much less damped relaxation oscillation - as a result of considering the polarization dynamics. We want to summarize our findings in Fig. 5.5(a,b,c). Our aim is to predict deviations between the modulation behaviour of Bloch and rate equations without actually simulating the full Bloch system. We can reach this goal by considering the information contained in the linearized systems. In other words we want to predict Fig. 5.5a by knowing the ratio between the imaginary and real parts (Fig. 5.5(b,c)) of the Eigenvalues of the Bloch and rate system, respectively. First of all it has to be mentioned, that only regions in the parameter space can be compared, where both the rate and Bloch system, have non-zero imaginary parts. Regions, where deviations between the real *or* the imaginary parts appear show possibly, but not necessarily, regions with deviations in the modulation behaviour. The blue and red regions in Fig. 5.5a stand for a parameter space, where the Bloch equations should be preferred, where in the light yellow regions the rate equation approximation is valid. Hence we recognize in Fig. 5.5b for a slow inversion decay T_1^{-1} a greater imaginary part in the rate equations. This results in a resonance coming up in the rate equations shortly after the resonance in the Bloch equations, so that a higher modulability can be expected, as long as the damping in this region stays equal. Fig. 5.5c shows the region in parameter space, where deviations in the real parts occur. Here the maximum real part of the Bloch equations are much greater, which shows up as less damped relaxation oscillations. If in this region the imaginary parts approach the cutoff frequency (which is the case in Fig. 5.4(iii,iv)), a deviation can be expected. In addition we can conclude, that if the imaginary part of the Bloch equations is slightly greater than the cutoff frequency of the rate equations, the Bloch equations predict a better modulability (Fig. 5.4iii). If in the other case the imaginary part is slightly smaller than the cutoff frequency, an early cutoff can occur (Fig. 5.4iv). If the discrepancy between those quantities is too large, neither of these two options will happen.

In order to verify our conclusions we examine a second parameter set with higher photon losses κ in Fig. 5.3. The first thing we notice here is that the maximum of modulability follows the photon decay rate κ and increases if all time scales are equal. The behaviour of this system equals the first parameter set. In Fig. 5.4v the rate system has no positive imaginary part, where the relaxation oscillation frequency in the Bloch system is much greater than the cutoff frequency. Consequential the resonance peak is too far away to show an influence on the cutoff frequency. The second class B case in Fig. 5.4vi show almost identical real and imaginary parts in the Bloch and rate system (Fig. 5.3(g,h,j,k)). The imaginary part in the Bloch system is marginally greater, which causes a likewise marginally increase of modulability. The first class C case in Fig. 5.4vii shows greater deviations. Although the imaginary part in the Bloch system is next to the cutoff region, no deviation to the rate system can be recognized. This is a result of the very high damping, which can be

seen in Fig. 5.3l. The situation is different for the second class C case in Fig. 5.4viii, where the damping is much smaller. The result is a resonance peak, which accidentally hardly changes the cutoff frequency, because the peak shows up at a frequency smaller than the cutoff. The behaviour of the second parameter set is summarized in Fig. 5.5(d,e,f). The first graphic shows the regions, where the actual deviations occur. The second graphic shows that in the region where the imaginary part in the rate system is smaller than in the Bloch system, the real parts are equal. This causes a decreasing modulability due to the polarization dynamics. The third graphic shows the region, where the Bloch relaxation oscillations are much less damped, while the imaginary part is near the cutoff frequency (Fig. 5.3i).
Analytical simulations for the rate system via Eq. (3.22) are shown in Appendix A.5, which provide similar results. In the toymodel the linearized system gives a proper explanation of the deviations in the modulability. Let us have a look at the more complicated model with an explicitely implemented spontaneous emission rate and scattering rates.

5.2 The full model

The full model (Eqs. 2.51 to 2.53 and Eqs. 2.54 to 2.55) considers scattering rates and a phenomenologically added spontaneous emission rate. This entails a greater difficulty simulating these systems, but shall basically prove similar behaviour as the toy model. Changing the inversion decay rate T_1^{-1} implies a not further specified loss. The effects of an explicitely implemented spontaneous emission rate are differentiated. It implies a more controllable rate caused only by the effect of spontaneous emission. The spontaneous emission rate can now exactly be determined and distinguished from the natural inversion decay of the system. We know from section 2.3, where the wettinglayer was introduced, that the inversion decay is determined by the electron density in the wettinglayer w_e, which again is given by the pump current. We will shortly see that regions, where deviations between the rate and the Bloch system occur, can not be expected around the point in the parameter space, where all time scales are of the same order of magnitude (contrary to the toy model). As a matter of comparability the following procedure is identical to the section before.
The modulation transfer curves in Fig. 5.8 show again that the resonance peaks strictly follow the relaxation oscillation frequency. In case of Fig. 5.8I the relaxation oscillation frequency (Fig. 5.6h) of the Bloch system is much larger than the cutoff frequency in the rate system and still increases with increasing the pump (Fig. 5.8II). In both cases the imaginary part does not appear in the rate system. In Fig. 5.8II can also be observed, that the slightly increased maximum real part causes a less damped resonance with the relaxation oscillation. The maximum real part (Fig. 5.6l) increases and the corresponding imaginary part (Fig. 5.6i) decreases when the polarization decay γ approaches the photon decay κ. This is the reason for a noticable improvement of modulability (Fig. 5.8III and Fig. 5.8IV). An interesting behaviour appears in Fig. 5.8IV, where the transferred modulation intensity goes beneath the 3db line, surpasses it again due to the resonance and decreases with further modulation frequency steps. This effect is knowingly not considered in the cutoff frequency image (Fig. 5.6c), as only the first cutoff guarantees a continuously well transferred modulation signal for all lower frequencies than the cutoff frequency.

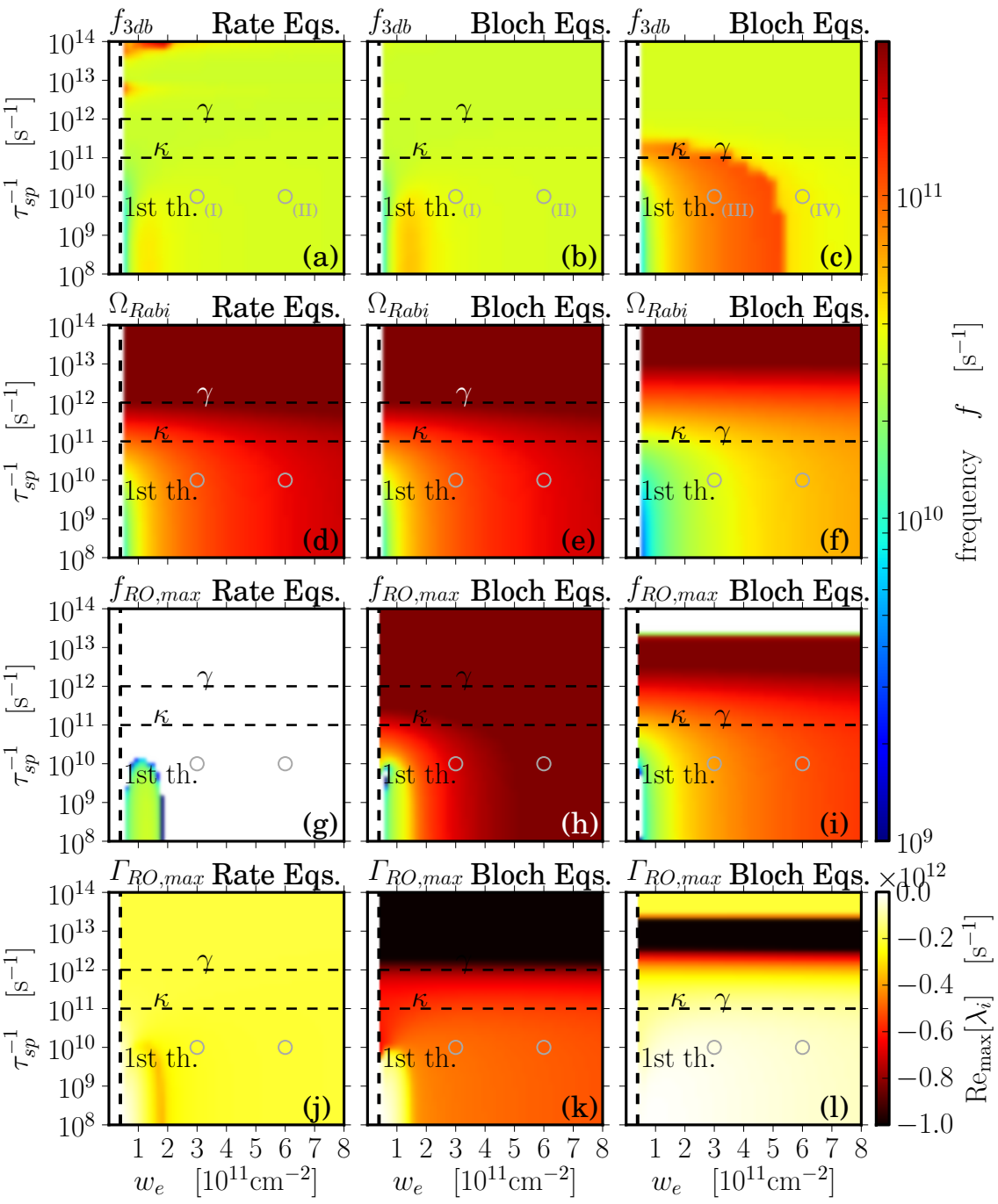

Figure 5.6: Comparison of rate (a,d,g,j) and Bloch (b,c,e,f,h,i,k,l) equations for a given $\kappa = 10^{11}\,\mathrm{s}^{-1}$. The control parameters are the electron density in the wetting layer w_e and the spontaneous emission decay τ_{sp}^{-1}, respectively. Figure caption is identical to Fig. 5.2.

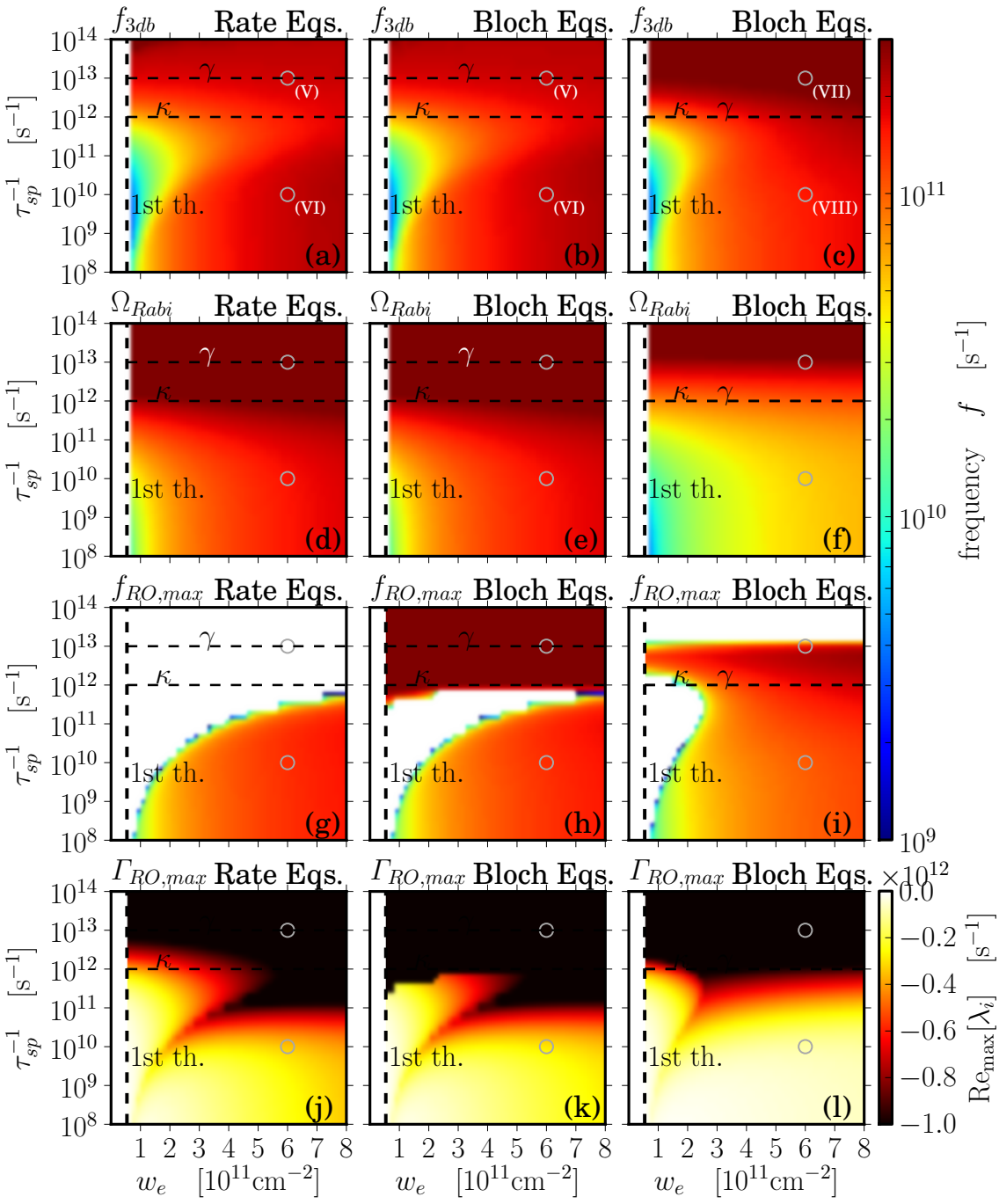

Figure 5.7: Comparison of rate (a,d,g,j) and Bloch (b,c,e,f,h,i,k,l) equations for a given $\kappa = 10^{12}\,\mathrm{s}^{-1}$. Figure caption is identical to Fig. 5.6.

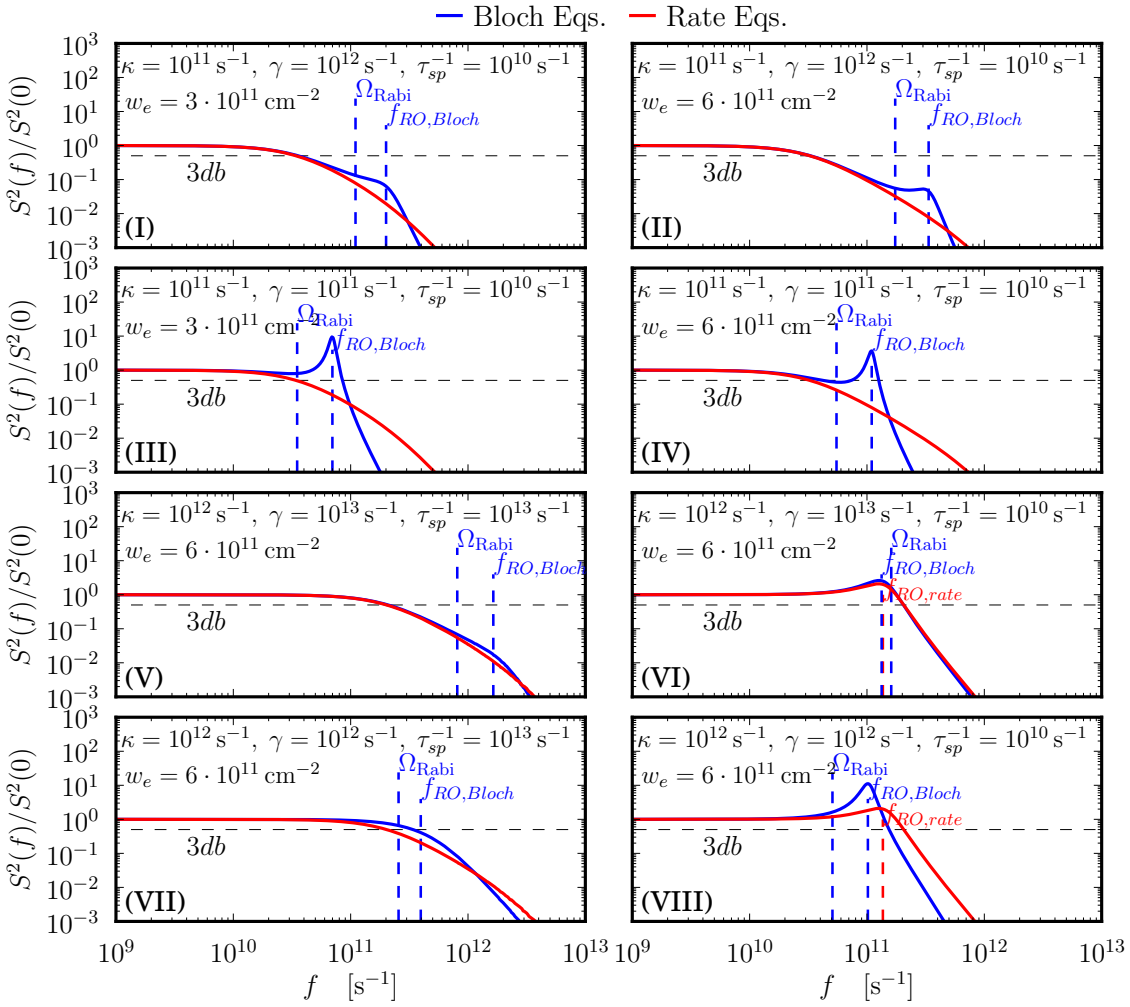

Figure 5.8: Normalized transferred small signal intensities versus the modulation frequency f for rate and Bloch equations. Graphs correspond to the circles with capital roman numbers in Fig. 5.6 and 5.7. Figure caption is identical to Fig. 5.4.

The second parameter set (Fig. 5.7) again is based on higher photon losses ($\kappa = 10^{12}\,\mathrm{s}^{-1}$). Interesting here is that the worst modulability is achieved for $\tau_{sp}^{-1} = \kappa$. In addition the region with the smallest deviation in modulation behaviour occurs where all time scales are of the same order of magnitude. This behaviour could not be observed in the toy model. Fig. 5.8V is comparable to Fig. 5.8I and shall not be discussed. In Fig. 5.8VI both the rate and Bloch system show similar resonance peaks due to the similar maximum real and imaginary part (Fig. 5.7(h,k)). When the polarization decay approaches the photon decay, the deviations increase. In Fig. 5.8VII a very small resonance in the Bloch system can be observed, which is due to the very small real part(Fig. 5.7l). The last image (Fig. 5.8VIII) shows a smaller cutoff frequency in the Bloch system. This is due to the smaller relaxation oscillation frequency compared to the rate system. The resonance peak is stronger in the Bloch system, due to the higher maximum real part, seen in Fig. 5.7(j,l).

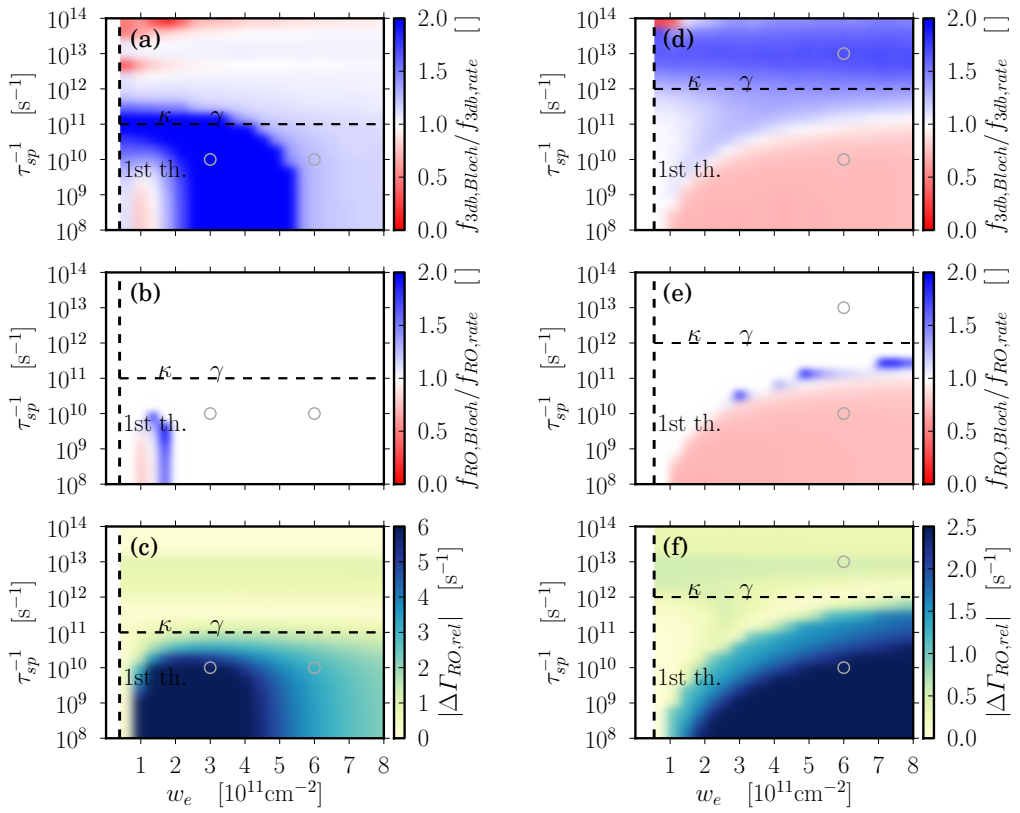

Figure 5.9: Figure caption is identical to Fig. 5.5. The relative difference between the maximum real parts is given by $\Delta\Gamma_{RO,rel} = \frac{|\Gamma_{RO,max,Bloch} - \Gamma_{RO,max,rate}|}{\Gamma_{RO,max,rate}}$.

We want to summarize this subsection in Fig. 5.9. The ratio of the cutoff frequencies corresponding to the first parameter set (Fig. 5.6) are shown in Fig. 5.9a. The ratio of the relaxation oscillation frequency in Fig. 5.9 is not revealing. Therefore the maximum real part gives a clear hint where the deviations can be expected, as long as the corresponding imaginary parts are nearby the cutoff frequency. Thus we recognize a good accordance in Fig. 5.9(a,c). The relative difference of the real parts for high spontaneous emission decay (Fig. 5.9c top) can not be noticed in the modulability, as no imaginary part exists for this decay rate (Fig. 5.6i top). The second parameter set (Fig. 5.7) is compared in Fig. 5.9(d,e,f). The Bloch equations predict a higher modulability for high spontaneous emission decay rates and a lower for small rates, compared to the rate equations. For the higher decay rates we note a small deviation in the real parts with no comparable imaginary parts. Nevertheless we already noticed an existing imaginary part, which does not correspond to the less damped real part. This relaxation oscillation frequency is still higher than the cutoff frequency, what explains the deviations on top of Fig. 5.9d. For slow spontaneous emission rates we find an relaxation oscillation frequency lower than the cutoff frequency of the rate system, together with a large deviation in the maximum real part in Fig. 5.9f. Hence we expect an earlier frequency cutoff compared to the rate system.

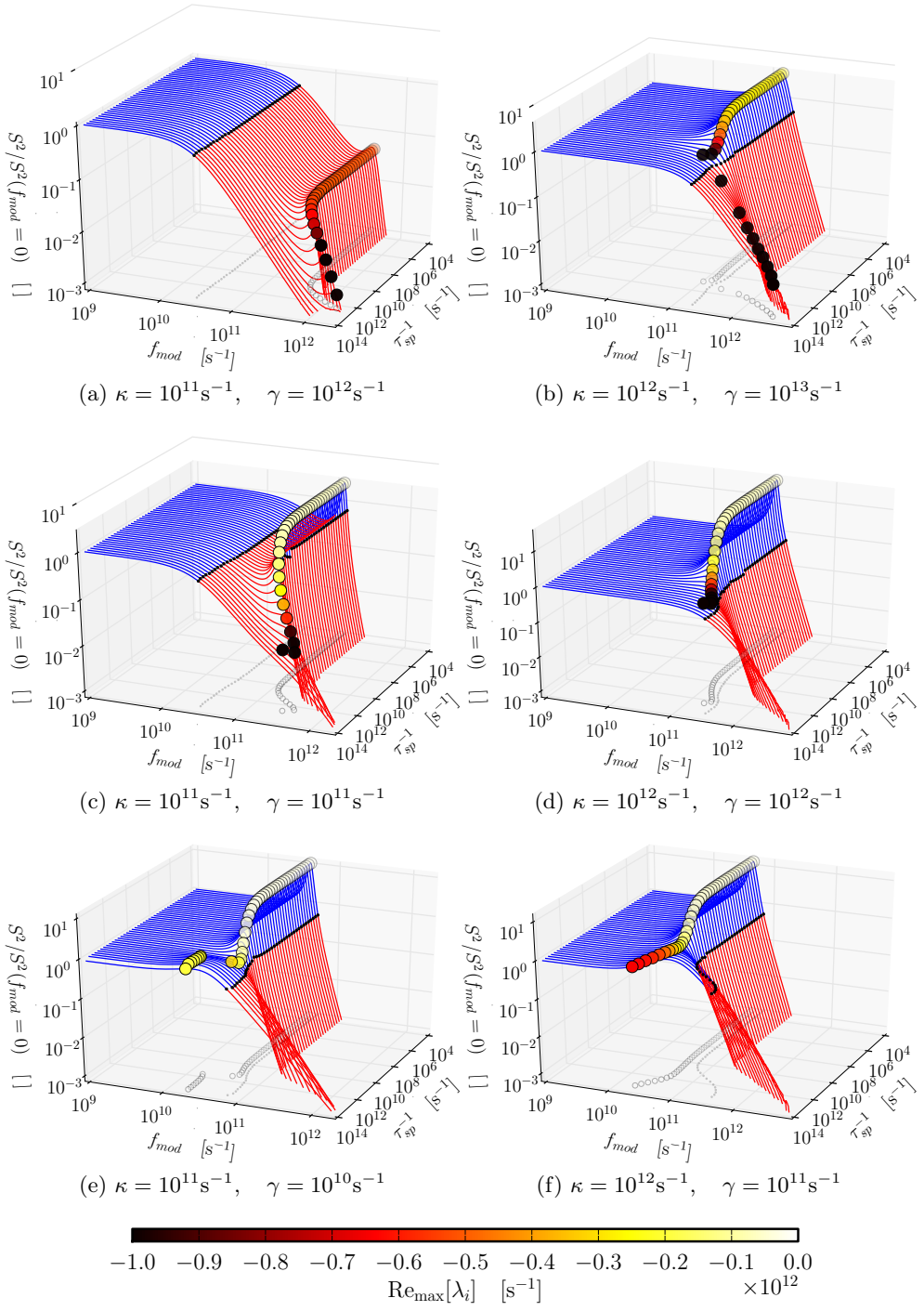

$$w_e = 8 \cdot 10^{11}\,\mathrm{cm}^{-2}, \quad G = 700\,\mathrm{cm}^{-1}$$

Figure 5.10: Modulation response curves for different spontaneous emission rates τ_{sp}^{-1} simulated via Bloch equations. The blue regions represent normalized intensities above the cutoff frequency f_{3db}, the red regions are below f_{3db}. The big circles indicate the imaginary parts of the linearized system, colorcoded by the value of the corresponding real part. The white circles and grey dots on the τ_{sp}^{-1}-f_{mod}-base plane are the projections of the imaginary part circles and the cutoff frequency dots.

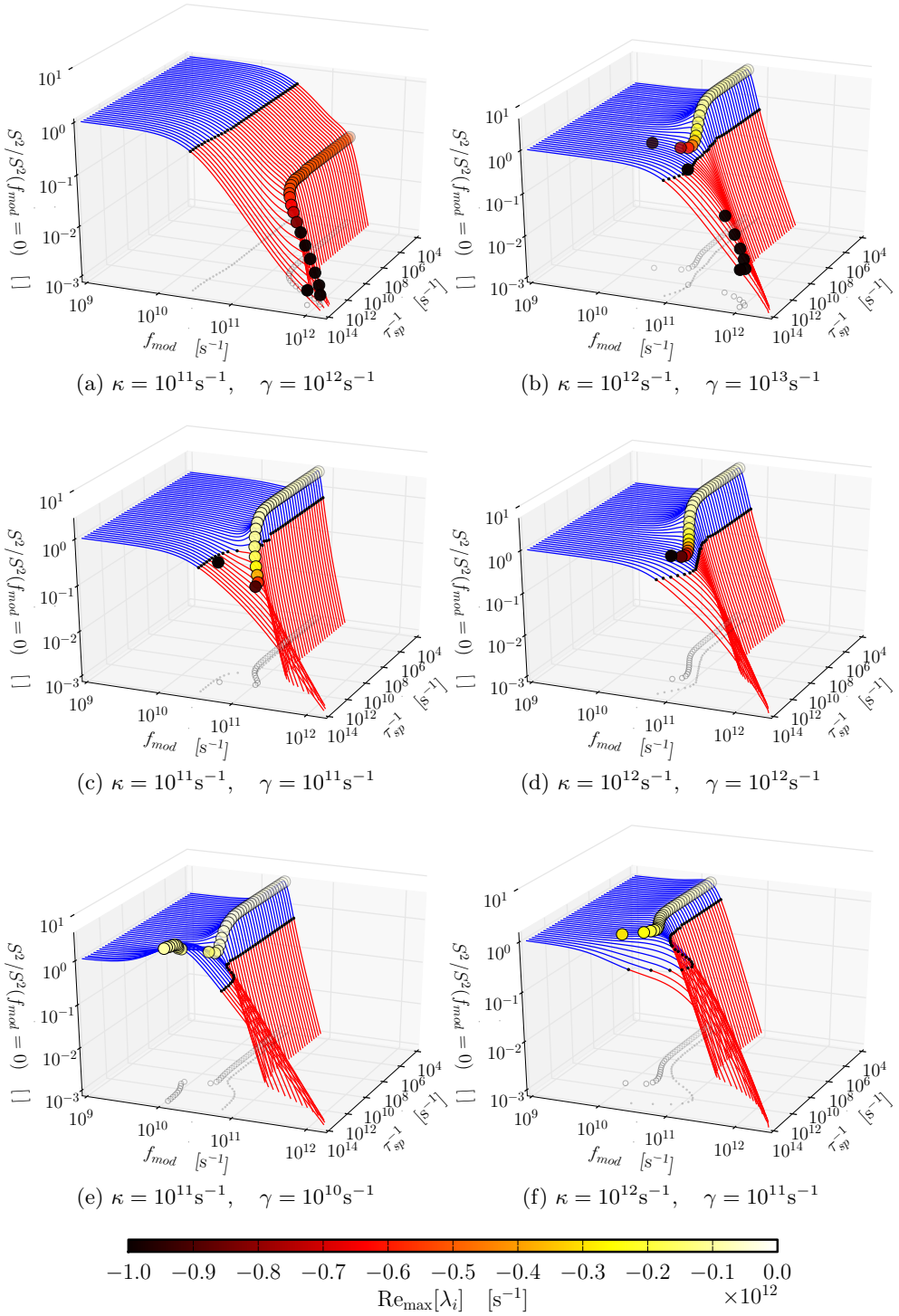

(a) $\kappa = 10^{11}\mathrm{s}^{-1}$, $\gamma = 10^{12}\mathrm{s}^{-1}$

(b) $\kappa = 10^{12}\mathrm{s}^{-1}$, $\gamma = 10^{13}\mathrm{s}^{-1}$

(c) $\kappa = 10^{11}\mathrm{s}^{-1}$, $\gamma = 10^{11}\mathrm{s}^{-1}$

(d) $\kappa = 10^{12}\mathrm{s}^{-1}$, $\gamma = 10^{12}\mathrm{s}^{-1}$

(e) $\kappa = 10^{11}\mathrm{s}^{-1}$, $\gamma = 10^{10}\mathrm{s}^{-1}$

(f) $\kappa = 10^{12}\mathrm{s}^{-1}$, $\gamma = 10^{11}\mathrm{s}^{-1}$

$w_e = 8 \cdot 10^{11}\,\mathrm{cm}^{-2}, \quad G = 200\,\mathrm{cm}^{-1}$

Figure 5.11: Figure caption is identical to Fig. 5.10. Simulated with lowered gain.

As a consequence of the previous findings, we know that lower cutoff frequencies can not be referred to a lower modulability, as for lower transferred intensities, frequencies far beyond the cutoff are still transferred very well. This makes it worth to have a look at the full modulation curves in Fig. 5.10 for a gain of ($G = 700\,\mathrm{cm}^{-1}$) and Fig. 5.10 for a gain of ($G = 200\,\mathrm{cm}^{-1}$). In these simulations the polarization decay can be chosen below the photon decay rate, as a fixed electron density in the wettinglayer fixes the inversion decay, so that the system stays within the *good cavity* region. The modulation transfer curves are only shown for the Bloch equations, as the graphics with a fast polarization decay (Fig. 5.10(a,b) and Fig. 5.11(a,b)) are similar to the rate equation simulations. The dynamics for ($\gamma < \kappa$) are reserved to the Bloch equations. In each simulation of both figures we recognize an increasing real part for higher spontaneous emission rates, which obviously weakens the resonance peaks. At the same time the imaginary parts increases for ($\gamma > \kappa$). This behaviour can also be observed in the toy model of the previous subsection. The resonances entail a great modulability for a particular modulation bandwidth, but also cause an early cutoff. If we move in the class C regime, we recognize for low spontaneous emission decay a noticable effect of the decreasing and more weakly damped imaginary parts. For higher spontaneous emission rates the imaginary parts further decreases until it approaches zero. For ($\gamma < \kappa$) we observe in Fig. 5.10(c,f) and Fig. 5.11(c,f) a resonance, which causes a great boost of both the cutoff frequency and the modulation behaviour for following frequencies. A simulation with different gain basically shows up the same effects, but with slightly different Eigenvalue spectra. All in all we can conclude that a prediction of deviations of modulability between the Bloch and rate system is possible, if the linearized systems and their Eigenvalue spectra are studied carefully.

6 Discussion

The here chosen model shall be briefly discussed and connected to recent research works. Decreasing the cavity volume entails a variety of consequences, which is why the Purcell factor itself was knowingly not changed during the simulations. Latest nanocavity lasers reach enhanced spontaneous emission rates due to both scaling down the cavity (Purcell enhancement) and adding metallic shells or contacts. In the latter case the effect of increased spontaneous emission rates is caused by resonant surface plasmon coupling [NEO02]. Common nanolaser principles depend on both effects and still operate with cavity lengths of up to the microscale. Important is the increased spontaneous transition rate and a atrong coupling to a single resonant wavemode in small cavity volumes [YAM91]. For example in a microdisk cavity a spontaneous emission enhancement of 15 has been observed [WEI00, GER98]. This order of magnitude is consistent with Fig. 2.4. But considering a cube with an edge length of 10 nm, a Purcell enhancement of approximately 10^{11} can be expected. This cube then only contains two to three quantum dots, considering a volume of $V_{QD} \approx 400\,\mathrm{nm}^3$. Decreasing the cavity dimensions further causes a change in the transition frequency, the quality factor and the Purcell enhanced stimulated emission rate. This clearly shows that the Purcell factor should not be the only controlled quantity, but the rate of spontaneous emission in general in order to keep neutrality to the models of the respective devices.

We now want to elaborate on a few recent research works. A heuristically motivated rate equation system was investigated in [LAU09] with respect to the modulation bandwidth of nanocavity LEDs. These regimes are characterized by below threshold operation conditions, where the rate of spontaneous emission dominates the rate of stimulated emission. The influence of both rates were investigated separately in a sample device and it was shown, that Purcell enhanced spontaneous emission can enhance the modulation bandwidth as long as the rate of stimulated emission is low. This result is consistent with the findings of [TUC85], where the modulation speed is found to be determined and limited by the stimulated emission rate, underlying the effect of gain compression. The modeled device is characterized in Fig. A.5. As we compare the model to ours we oppose that the depicted quantities in Fig. A.5(c-e), the cutoff frequency, the imaginary and the real parts, strongly depend on the polarization decay, which is not considered in this model. Thus we find cases, where the spontaneous emission leads to increased cutoff frequencies, and cases, where the opposite takes place, depending on the polarization dynamics. Another interesting aspect investigated in [LAU09] is the maximum cutoff frequency in such a device. The maximum is found to be

$$f_{3db,max} \approx \frac{1}{2\pi} \frac{1}{\sqrt{\kappa^{-2} + \tau_{sp}^2}},$$

where the rate of stimulated emission is neglected, as the device shall be biased below threshold. The optimal quality factor then occurs for an equality of photon and spontaneous emission lifetime

$$\kappa^{-1} \approx \tau_{sp}.$$

We notice that our toy model ansatz is most similar to such a device with only one rate

that contributes to inversion decay and does not underlie gain compression and furthermore emits with a β-factor of one into a resonant cavity mode due to the small mode volume. It can be observed in our simulations, that the maximum cutoff frequency occurs under this condition. But it has to be mentioned, that this is not true for our full model with scattering rates and a separate spontaneous emission rate. In the class C regime ($\gamma \lesssim \kappa$) the modulation bandwidth enhancement occurs with a tendency of $\tau_{sp}^{-1} \gtrsim \kappa$.

Furthermore we find good agreement to [WIE14], where stabilising and destabilising effects of polarization dynamics are studied. We agree in finding only a very small region in parameter space, where the polarization has a stabilising effect, which means where a small real part appears and where the real part can decrease with lowering the polarization decay. A comparison between our model and [WIE14] was performed, which is depicted in Fig. A.6.

Another important aspect is the comparison to the microscopic theory [LOR13, GRE12a]. The rate equations in [LOR13] are derived via Markovian approximation, which corresponds to an adiabatic elimination of polarization. The Markov approximation is said to be trivially true in steady state, which is why a good accordance is found between the rate equations and the microscopic theory. Nevertheless deviations were found for non-steady state results, which were connected to non-Markovian effects and the additional influence of carrier-photon correlations. These deviations decreased with neglected carrier-photon correlations, but did not vanish. We agree with these deviations and showed impressively in Sec. 4, especially in Fig. 4.3(f,g), that the rate equation system completely suppresses oscillations in the $|c|^2$-p-plane and only grasps the projection of the Bloch equation system, even if the steady state stays unchanged. This additional degree of freedom entails an instability, as the system always oscillates in this plane, as soon as the parameter region allows to do so. The logical consequences are resonances with external modulations, which do not appear in the rate equation system.

On the one hand lowering the polarization decay induces in our model mostly an increase of the real part of the eigenvalues in the linearized system, which results in a resonance peak in the modulation transfer curve. Shortly after the peak a steep decline of the transferred intensity can be observed. On the other hand the spontaneous emission decay counters this effect with decreasing the real part. This is true for all photon decay rates κ and high pump strengths, but deviations were found for low pump strengths. These deviations are depicted in Fig. 5.6(j-l), 5.7(j-l) and A.6. If this interaction between polarization and spontaneous emission results in a positive or a negative influence on modulation behaviour turns out to be very individual, as one can conclude from Fig. 5.10 and 5.11. Furthermore for a high spontaneous emission decay it depends on the polarization timescale, whether the imaginary part of the linearized system decreases or increases. This also has great impact, as the appearance of the resonance peak changes the curve fundamentally. However what all our investigations share is a boost of the modulation cutoff frequency f_{3db} and a reduction of the steep decline of the transferred intensity after a resonance peak in a modulation transfer curve for a slow polarization ($\gamma < \kappa$) and a high spontaneous emission decay ($\tau_{sp}^{-1} > \kappa$), which is clearly underestimated with the rate equation model. In other words for high spontaneous emission the resonance peak itself shows up with a greater

modulation bandwidth. The relaxation oscillation frequency does not match with the peak in that case, what can be originated from the very strong damping. As it is known from Fig. 4.9, high spontaneous emission rates rise the photon number in the cavity by a factor hundred and more, which may lead to the development of the peak in spite of an increased damping. It is clearly no *large signal regime*, as this peak appears similarly for different small modulation amplitudes. One possible explanation for this extraordinary peak could be the change of the ratio of spontaneous and stimulated emission rates, paired with a change of the stability character by polarization. This is in accordance with [LAU09], where the bandwidth is increased if spontaneous emission dominates the laser emission. Note that Purcell enhanced spontaneous emission saturates with increasing the quality factor [SUH10].

7 Conclusion and outlook

Scaling down the cavity dimensions implies the necessity of reinvestigation of the dynamics, stability and modulability under the influence of increased heat generation of small devices, surface plasmon coupling and last but not least the effect of increased spontaneous emission, whereby we investigate the latter effect. A small cavity is characterized by an increased spontaneous transition rate and a photonic density of states, which consists of a single wave mode and reaches its maximum for a resonant driven cavity. Thereby the β-factor increases drastically due to the high coupling efficiency [YAM91], which is why the simulations were performend with $\beta = 1$. Minor consequences of a lowered cavity volume are changing transition frequencies, the higher quality factor or the number of involved quantum dots, paired with a changed confinement. It was aspired to keep our model as simple as possible, while including a minimum of realistic features and effects of our interest, such as scattering rates from a wettinglayer to the lasing quantum dots, polarization dynamics, a deterministic spontaneous emission rate and Purcell enhancement of spontaneous emission. The model was motivated, derived and simplified in Sec. 2, the Purcell factor was derived. Detailed analytics, including the linearizations of the equation systems, the fixed points, the eigenvalues for rate and Bloch equations, and the modulation transfer function for 2x2-matrices, can be found in Sec. 3. All numerical simulations were steadily compared with the linearized counterpart, in order to achieve better understanding and the possibility of a prediction of the system's behaviour. The investigation of dynamics in Sec. 4 was to globally characterize our model. We successively showed class A, B, and C operating conditions by means of time series, eigenvalues and bifurcation analysis, compared the Bloch and the rate regime and clarified the influence of scattering rates and spontaneous emission, respectively. Especially mentionable is the stabilising effect of spontaneous emission, as it pushes the system away from a bad cavity condition. Another insight is the mostly destabilising (tendency to increasing real parts and decreasing imaginary parts) effect of slow polarization, which is consistent with the findings of [WIE14] (Fig. A.6). A detailed analysis of the small signal response is given in Sec. 5, a linear response, where the consequences of the stability change due to polarization and spontaneous emission can be observed directly. Here a rather neutral (toy) model was compared to our more real-

istic (full) model, whereby a quality factor according the device of Fig. 1.1 was chosen. While in the toy model the maximum cutoff frequency is achieved for ($\gamma \approx \kappa \approx T_1^{-1}$), the the full model has a tendency for $\tau_{sp}^{-1} \gtrsim \kappa \approx T_1^{-1}$. It is clearly exposed that the interaction between the polarization and the spontaneous emission timescales can have great and very individual impact on the modulation behaviour. The resonances in these modulation curves originate from the third eigenvalue in the Bloch equation system, which does not appear in the rate equation system. The adiabatic elimination of the polarization dynamics completely suppresses oscillations in the $|c|^2$-p-plane. Oscillations in this plane immediately correspond to Rabi oscillations. This additional degree of freedom results in resonances with external modulations.

After all, we discussed our model and the results in Sec. 6 and performed a detailed comparison to recent research works. In conclusion we find either well studied, simplified models about the effect of spontaneous emission in the rate equation system, or the effect of polarization dynamics on stability properties in the Bloch equation system, but not both. This gap is closed with this thesis.

We found a significant enhancement of the modulation bandwidth for a slow polarization ($\gamma < \kappa$) and a high spontaneous emission decay ($\tau_{sp}^{-1} > \kappa \approx T_1^{-1}$), which is characterized by a resonance peak and suppression of the steep intensity decline after the peak. The maximum rate of stimulated emission limits the modulation bandwidth [LAU09], whereby at this point the spontaneous emission decay is much greater than all other timescales of the system. As this peak is absent in the rate equation simulations, theses simplified models cannot be trusted in predicting realistic device properties. It can be of great interest for device design, where a high bandwidth is needed.
It remains to clarify when exactly this second extraordinary peak in the modulation transfer curves for ($\gamma < \kappa$) and ($\tau_{sp}^{-1} > \kappa$) appears, which is why the rate of spontaneous and stimulated emission and their contributions in the eigenvalue spectrum should be investigated separately. Another interesting approach would be a stability analysis of a higher order. If the peak appears for Purcell enhanced spontaneous emission in nano devices, can Purcell enhanced stimulated emission counter this ratio? Besides the effect of increased spontaneous emission, other effects like temperature dependencies and Purcell enhanced stimulated emission, caused by down scaling the cavity dimensions, and their effect on linear stability and modulability should be investigated.

A Appendix

A.1 Auxiliary calculation

Here we show a detailed calculation from Eq. (2.27) to Eq. (2.29). We begin with the derivation of Eq. (2.28)

$$\dot{E}_\lambda^\pm(t) = \left(\dot{\bar{E}}_\lambda(t) \mp \mathrm{i}\omega_\lambda \bar{E}_\lambda(t)\right) e^{\mp \mathrm{i}\omega_\lambda t}. \tag{A.1}$$

The first step of the *SVEA* $\left(|\dot{\bar{E}}_\lambda(t)| \ll |\omega_\lambda \bar{E}_\lambda(t)|\right)$ gives us

$$\dot{E}_\lambda^\pm(t) \approx \mp \mathrm{i}\omega_\lambda E_\lambda^\pm(t). \tag{A.2}$$

We continue with a further derivation of Eq. (A.1), perform the second step of the *SVEA* $\left(|\ddot{\bar{E}}_\lambda| \ll |\omega_\lambda \dot{\bar{E}}_\lambda|\right)$ and find

$$\begin{aligned} \ddot{E}_\lambda^\pm(t) &= \left(\ddot{\bar{E}}_\lambda(t) \mp 2\mathrm{i}\omega_\lambda \dot{\bar{E}}_\lambda(t) - \omega_\lambda^2 \bar{E}_\lambda(t)\right) e^{\mp \mathrm{i}\omega_\lambda t} \\ &\approx \mp 2\mathrm{i}\omega_\lambda \left(\dot{E}_\lambda^\pm(t) \pm \mathrm{i}\omega_\lambda E_\lambda^\pm(t)\right) - \omega_\lambda^2 E_\lambda^\pm(t), \end{aligned} \tag{A.3}$$

where we used the relation $\left(\dot{\bar{E}}_\lambda(t) e^{\mp \mathrm{i}\omega_\lambda t} = \dot{E}^\pm(t) \pm \mathrm{i}\omega_\lambda E^\pm(t)\right)$. We put Eq. A.2 and Eq. A.3 into Eq. (2.27) and receive

$$\mp 2\mathrm{i}\omega_\lambda \left(\dot{E}_\lambda^\pm(t) \pm \mathrm{i}\omega_\lambda E_\lambda^\pm(t)\right) \mp \frac{\mathrm{i}\omega_\lambda \sigma}{\varepsilon_0} E_\lambda^\pm(t) = \frac{\omega_\lambda^2}{\varepsilon_0} P_\lambda^\pm.$$

We divide the latter equation by $(2\mathrm{i}\omega_\lambda)$, substitute with the photon decay rate ($\kappa = \sigma/2\varepsilon_0$) and find

$$\begin{aligned} \mp \dot{E}_\lambda^\pm(t) &= (+\mathrm{i}\omega_\lambda \pm \kappa)\, E_\lambda^\pm(t) + \frac{\omega_\lambda^2}{2\mathrm{i}\omega_\lambda \varepsilon_0} P_\lambda^\pm \qquad \Big| \cdot (\mp 1) \\ \dot{E}_\lambda^\pm(t) &= (\mp \mathrm{i}\omega_\lambda - \kappa)\, E_\lambda^\pm(t) \pm \frac{\mathrm{i}\omega_\lambda}{2\varepsilon_0} P_\lambda^\pm. \end{aligned}$$

A.2 Scattering rates

The full scattering rates [LUE11a], which consider both electron and hole dynamics, are given by

$$
\begin{aligned}
S_e^{in}(w_e, w_h) &= \Big(0,00895343 w_e^2 + 0,0000926157 w_h^2\Big) \Big/ \Bigg(\Big(1 - 0,0439039 \frac{w_h}{w_e} \\
&\quad +0,211373 w_e + 0,194881 w_h - 0,00985679 w_e^2 + 0,00207208 w_h^2 \\
&\quad +0,0170416 w_e w_h \Big) e^{(-0,0114633 w_e + 0,0116515 w_h)} \Bigg), \\
S_h^{in}(w_e, w_h) &= \Big(0,00895343 w_e^2 + 0,0000926157 w_h^2\Big) \Big/ \Bigg(\Big(1 - 0,0439039 \frac{w_h}{w_e} \\
&\quad +0,211373 w_e + 0,194881 w_h - 0,00985679 w_e^2 + 0,00207208 w_h^2 \\
&\quad +0,0170416 w_e w_h \Big) e^{(0,0162571 w_e + 0,000169687 w_h)} \Bigg), \\
S_e^{out}(w_e, w_h) &= S_e^{in}(w_e, w_h) \cdot \frac{0,084133}{e^{0,215347 w_e} - 1,0}, \\
S_h^{out}(w_e, w_h) &= S_h^{in}(w_e, w_h) \cdot \frac{0,25828}{e^{0,0205776 w_h} - 1.0},
\end{aligned}
$$

where w_e and w_h is the electron and hole density in the wettinglayer in units of $\left[10^{11}\,\mathrm{cm}^{-2}\right]$. The resulting rates are in units of $\left[\mathrm{ps}^{-1}\right]$ and were fitted for a temperature of $(T = 300\,\mathrm{K})$.

A.3 Runge-Kutta fourth order algorithm

The Runge-Kutta fourth order algorithm has the following form:

$$\begin{aligned} k_1 &= hf(x_n, y_n) \\ k_2 &= hf(x_n + \frac{1}{2}h, y_n + \frac{1}{2}k_1) \\ k_3 &= hf(x_n + \frac{1}{2}h, y_n + \frac{1}{2}k_2) \\ k_4 &= hf(x_n + h, y_n + k_3) \\ y_{n+1} &= y_n + \frac{1}{6}k_1 + \frac{1}{3}k_2 + \frac{1}{3}k_3 + \frac{1}{6}k_4 + O(h^5) \end{aligned}$$

This ordinary differential equation solver performs four evaluation steps $k_{1,\ldots,4}$ per integration step h. List. 1 shows the code implementation of this algorithm in *C++*, templated on the ordinary differential equation object *dgl*. One function call updates the solution vector y to its new value after a given timestep h. The *void*-method *dgl*() of the *dgl*-object takes the time t, the solution vector y and its derivative $\frac{\mathrm{d}y(t)}{\mathrm{d}t}(= k_{1,\ldots,4})$ as an argument and updates the latter value.

```
template <class T>
void rk4(VecDoub& y, const double t, const double h, T& dgl)
{
  int n = y.size();
  //Initialization of vector objects, which are characterized by arrays of
      a given length n with double-valued entries and vector specific
      methods.
  VecDoub yt(n), k1(n), k2(n), k3(n), k4(n);

  dgl(t, y, k1);

  for (int i=0; i<n; ++i)
    yt[i] = y[i] + h * k1[i]/2.;
  dgl(t+h/2., yt, k2);

  for (int i=0; i<n; ++i)
    yt[i] = y[i] + h * k2[i]/2.;
  dgl(t+h/2., yt, k3);

  for (int i=0; i<n; ++i)
    yt[i] = y[i] + h * k3[i];
  dgl(t+h, yt, k4);

  for (int i=0; i<n; ++i)
    y[i] += h * ( k1[i]/6. + (k2[i]+k3[i])/3. + k4[i]/6. );
}
```

Listing 1: Runge-Kutta fourth order code implementation example in *C++*.

A.4 Eigenvalues of the Bloch equations

We derive the analytical expression for the eigenvalues of the Bloch equations without spontaneous emission. Therefore we solve the characteristical polynomial of the matrix $\underline{\underline{A}}$ in Eq. (3.8)

$$\begin{aligned}
\det(\underline{\underline{A}} - \lambda\mathbb{1}) &= -c'g(4c'g\kappa + 8g^2p'Z^{QD}\Gamma + 4c'g\lambda) \\
&\quad +(-2d'g^2Z^{QD}\Gamma + \kappa\gamma + \kappa\lambda + \gamma\lambda + \lambda^2)(-\lambda - T_1^{-1}) \\
&= 4c'^2g^2\kappa - 8c'g^3p'Z^{QD}\Gamma - 4c'^2g^2\lambda + 2d'g^2Z^{QD}\Gamma T_1^{-1} \\
&\quad -\kappa\gamma T_1^{-1} - \kappa\lambda T_1^{-1} - \gamma\lambda T_1^{-1} - \lambda^2 T_1^{-1} + 2d'g^2Z^{QD}\Gamma\lambda \\
&\quad -\kappa\gamma\lambda - \kappa\lambda^2 - \gamma\lambda^2 - \lambda^3 \\
&= -\lambda^3 - \lambda^2(\gamma + \kappa + T_1^{-1}) \\
&\quad -\lambda(\kappa\gamma - 2d'g^2Z^{QD}\Gamma + T_1^{-1}(\gamma + \kappa) + 4c'^2g^2) \\
&\quad -4c'^2g^2\kappa - 8c'g^3p'Z^{QD}\Gamma + 2d'g^2Z^{QD}\Gamma T_1^{-1} - \kappa\gamma T_1^{-1} \\
&\stackrel{!}{=} 0.
\end{aligned}$$

This expression can be written in the normal form

$$\lambda^3 + a\lambda^2 + b\lambda + c = 0,$$

where

$$\begin{aligned}
a &= \gamma + \kappa + T_1^{-1}, \\
b &= \kappa\gamma - 2d'g^2Z^{QD}\Gamma + T_1^{-1}(\gamma + \kappa)4c'^2g^2, \\
c &= 4c'g^2\kappa + 8c'p'g^3Z^{QD}\Gamma - 2d'g^2Z^{QD}\Gamma T_1^{-1} + \kappa\gamma T_1^{-1}.
\end{aligned}$$

With Cardano's method we can substitute

$$\begin{aligned}
\lambda &= z - \frac{a}{3}, \\
p &= b - \frac{a^2}{3}, \\
q &= \frac{2a^3}{27} - \frac{ab}{3} + c,
\end{aligned}$$

out of which we find

$$z^3 + pz + q = 0.$$

It remains to determine

$$z = u + v,$$

where

$$\begin{aligned} u &= \sqrt[3]{-\frac{q}{2}+\sqrt{D}}, \\ v &= \sqrt[3]{-\frac{q}{2}-\sqrt{D}}, \\ D &= \left(\frac{q}{2}\right)^2+\left(\frac{p}{3}\right)^3. \end{aligned}$$

The three solutions of z are then given by

$$\begin{aligned} z_1 &= u+v, \\ z_{2,3} &= -\frac{u+v}{2} \pm \mathrm{i}\sqrt{3}\frac{u-v}{2}. \end{aligned}$$

We can rewrite these solutions with respect to

$$\begin{aligned} \lambda_1 &= u+v+\frac{a}{3}, \\ \lambda_{2,3} &= \underbrace{-\frac{u+v}{2}+\frac{a}{3}}_{\Gamma_{RO}} \pm \mathrm{i}\underbrace{\sqrt{3}\frac{u-v}{2}}_{\omega_{RO}}, \end{aligned}$$

which are the three Eigenvalues of the Bloch equations without spontaneous emission for ($D > 0$). This calculation can easily be expanded for the linearized system with spontaneous emission in Eq. (3.9).

A.5 Analytical modulation response simulations

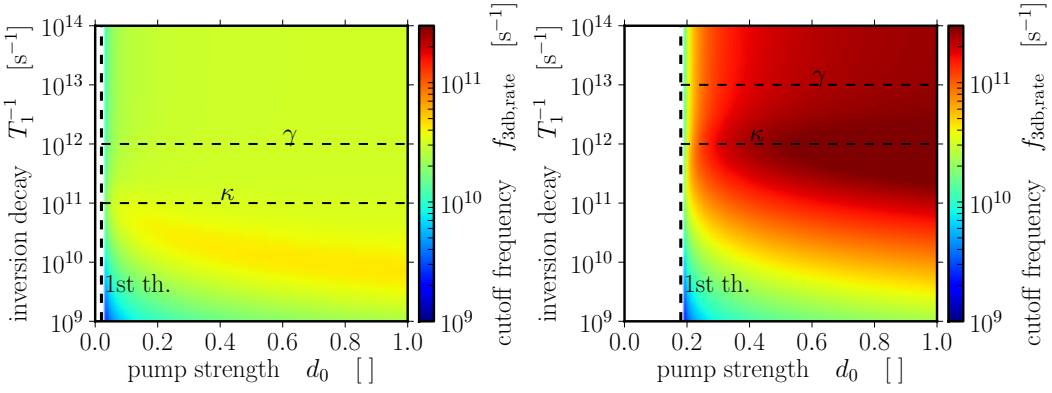

(a) Full model. (b) Full model.

Figure A.1: Analytical simulations for the rate system via Eq. (3.22). The numerical counterparts are depicted in Fig. 5.2a and 5.3a. The figure caption is identical.

A.6 Small signal response

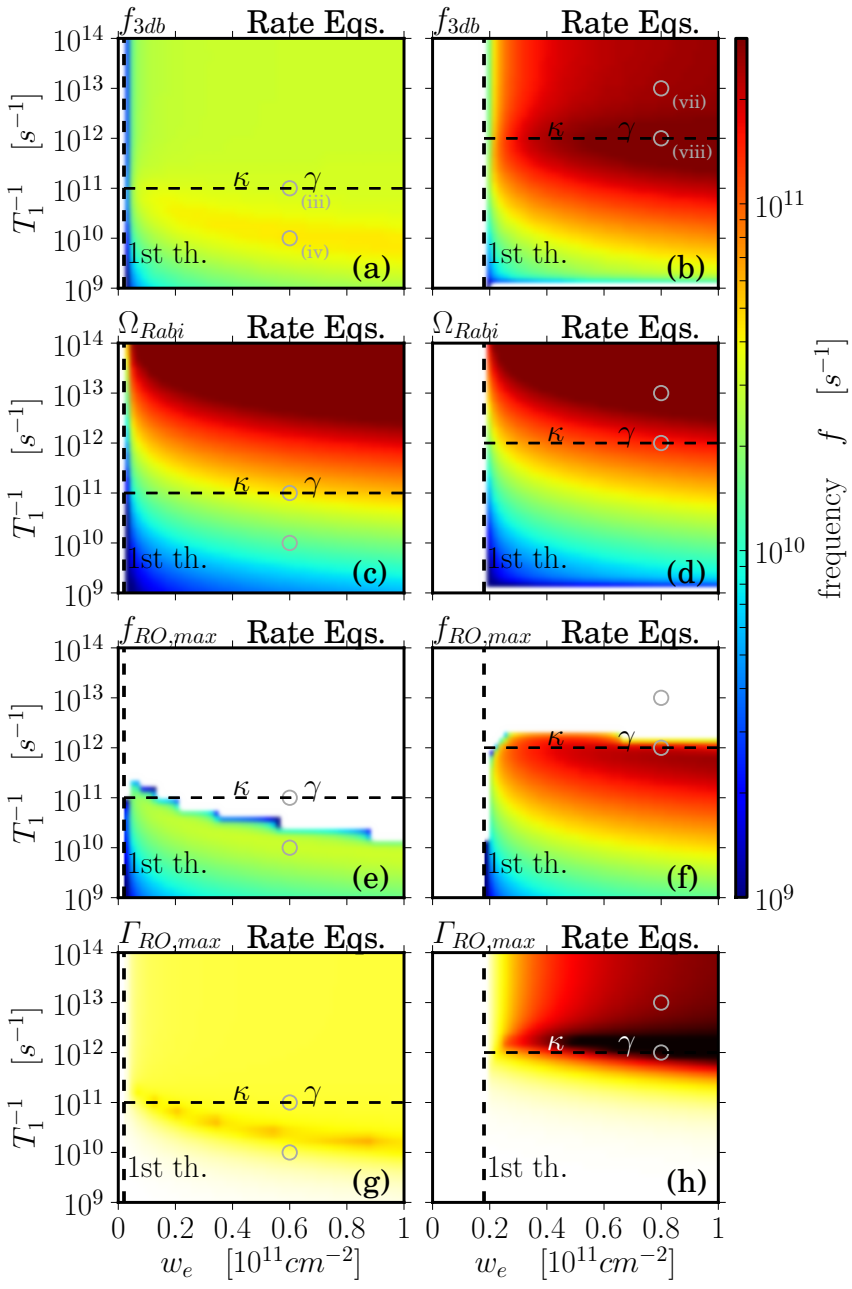

Figure A.2: Supplement to Fig. 5.2 (left column) and Fig. 5.3 (right column) for ($\kappa = \gamma$), simulated with the rate equations. The colorcodes for the real parts are shown in the referred graphics, as both graphs scale differently. Figure caption is identical.

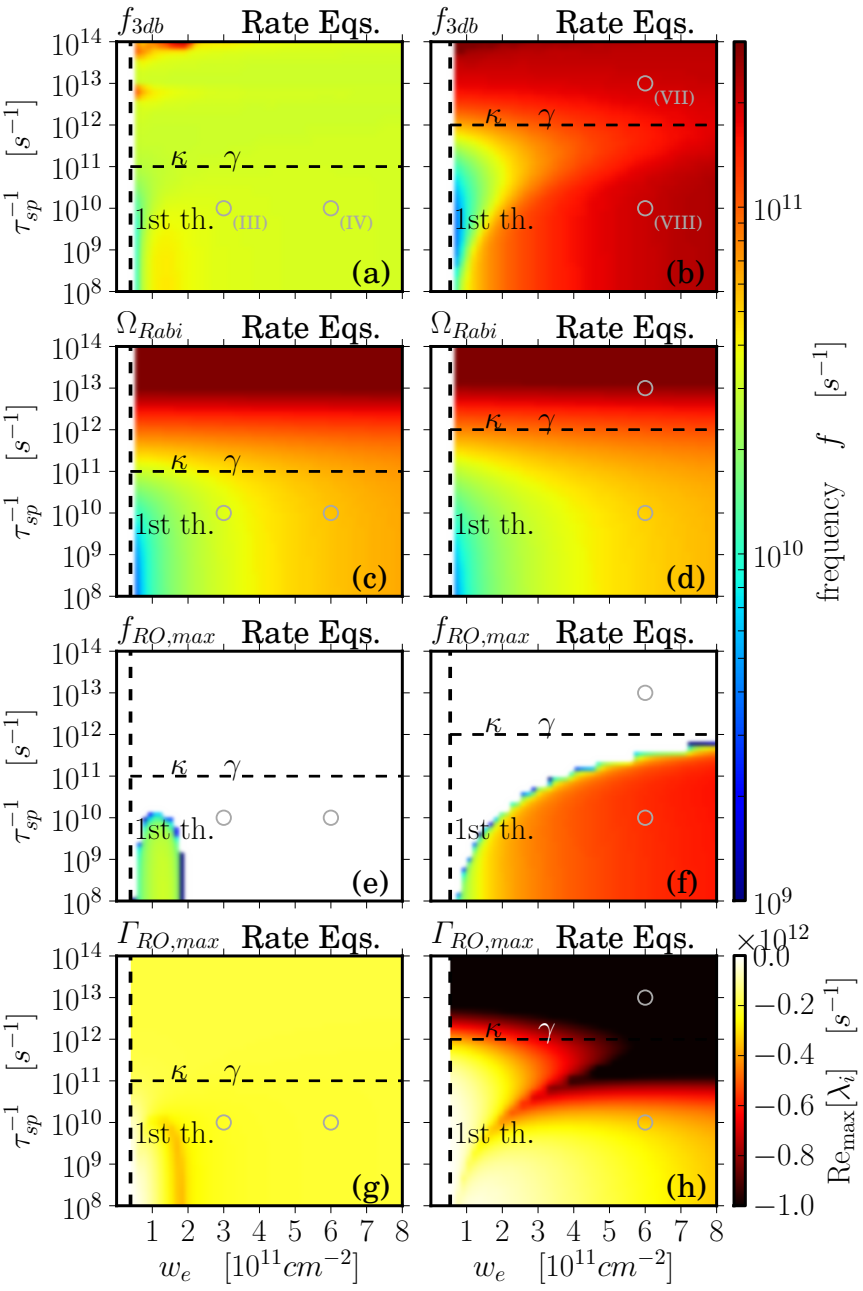

Figure A.3: Supplement to Fig. 5.6 (left column) and Fig. 5.7 (right column) for ($\kappa = \gamma$), simulated with the rate equations. Figure caption is identical.

A.7 Comparability between toy and full model

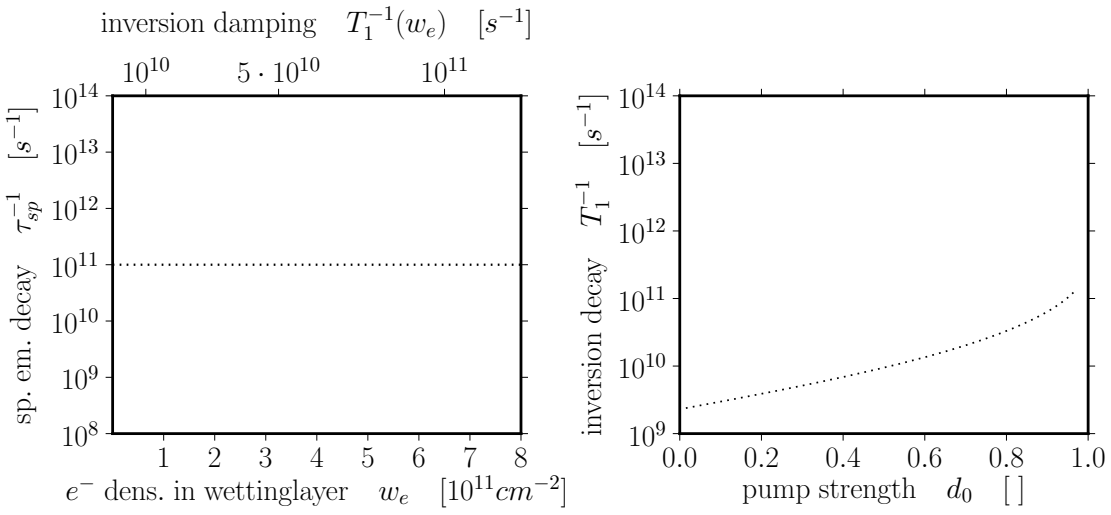

(a) Full model.

(b) Toy model.

Figure A.4: These graphics show a blank plot (without plotted data), as it is used for depicting the cutoff and Rabi frequencies f_{3db} and Ω_{Rabi}, as well as the imaginary and real parts $\mathrm{Im}_{\max}$ and $\mathrm{Re}_{\max}$ in Sec. 5. Any horizontal line in the full model corresponds to the dotted line in the toy model, where an additional spontaneous emission decay rate is not considered. Hence the dotted line in the toy model corresponds to zero spontaneous emission in the full model. Increasing τ_{sp}^{-1} shifts the dotted line in the toy model upwards, as this would increase the net inversion decay.

A.8 Sample device of [LAU09]

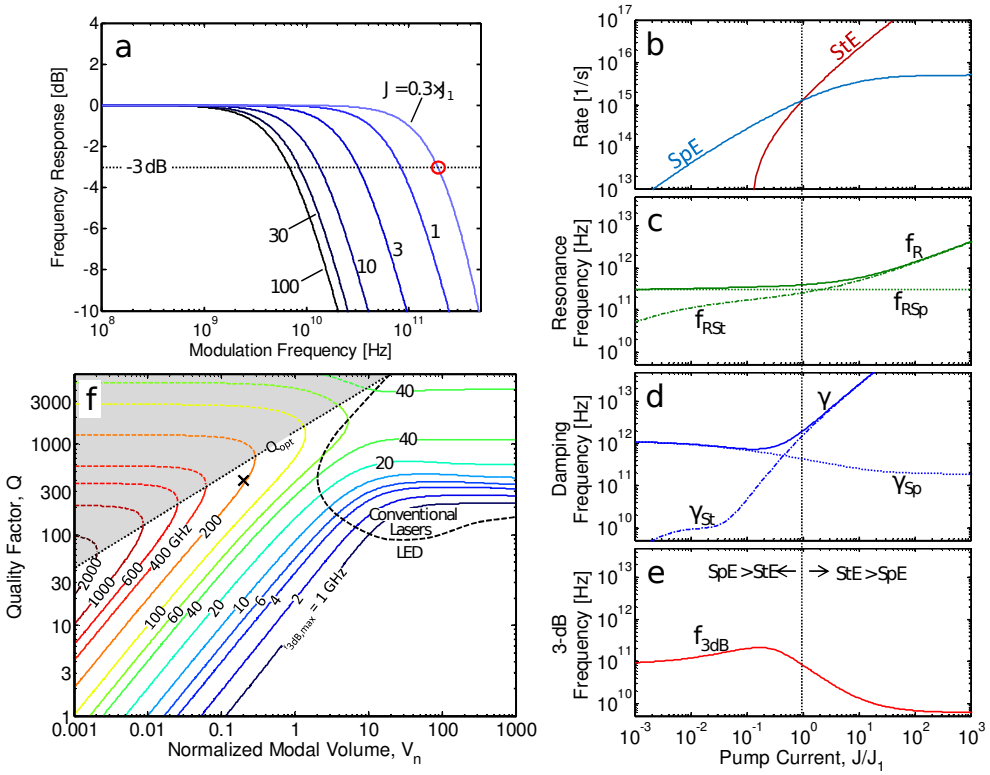

Figure A.5: Figure and figure caption provided by [LAU09]. (a) Normalized frequency response as a function of different pump currents for a Purcell enhanced nanocavity light emitter with $Q = 400$ and $V_n = 0,2$. The largest 3db bandwidth (red circle) occurs below threshold and is $f_{3db,max} \approx 200\,\text{GHz}$. When biased above threshold, the bandwidth decreases to 6 GHz. (b) Spontaneous emission (SpE) and stimulated emission (StE) rates versus pump current (normalized to J_1). For currents below the dotted line, the SpE rate is greater than the StE rate. This is reversed above J_1. (c) Resonance frequency (f_R) and (d) damping rate (γ) versus current. In (c) and (d) the contributions from SpE and StE are sperately shown using a "Sp" and "St" subscript, respectively. (e)3db bandwidth (f_{3db}) versus current. When StE dominates, the bandwidth drops due to increased damping from gain compression. (f) Contour plot of maximum 3db bandwidth for nanocavity emitters (including both lasers and LEDs) with different modal volumes and quality factors. The dashed contour seperates the devices where the maximum bandwidth is found below or above J_1, labeled "LED" and "Conventional Lasers", respectively. The strong-coupling regime is similarly labeled with a dotted line. The "x" marks the example device in panel (a) through (e).

A.9 Comparison to [WIE14]

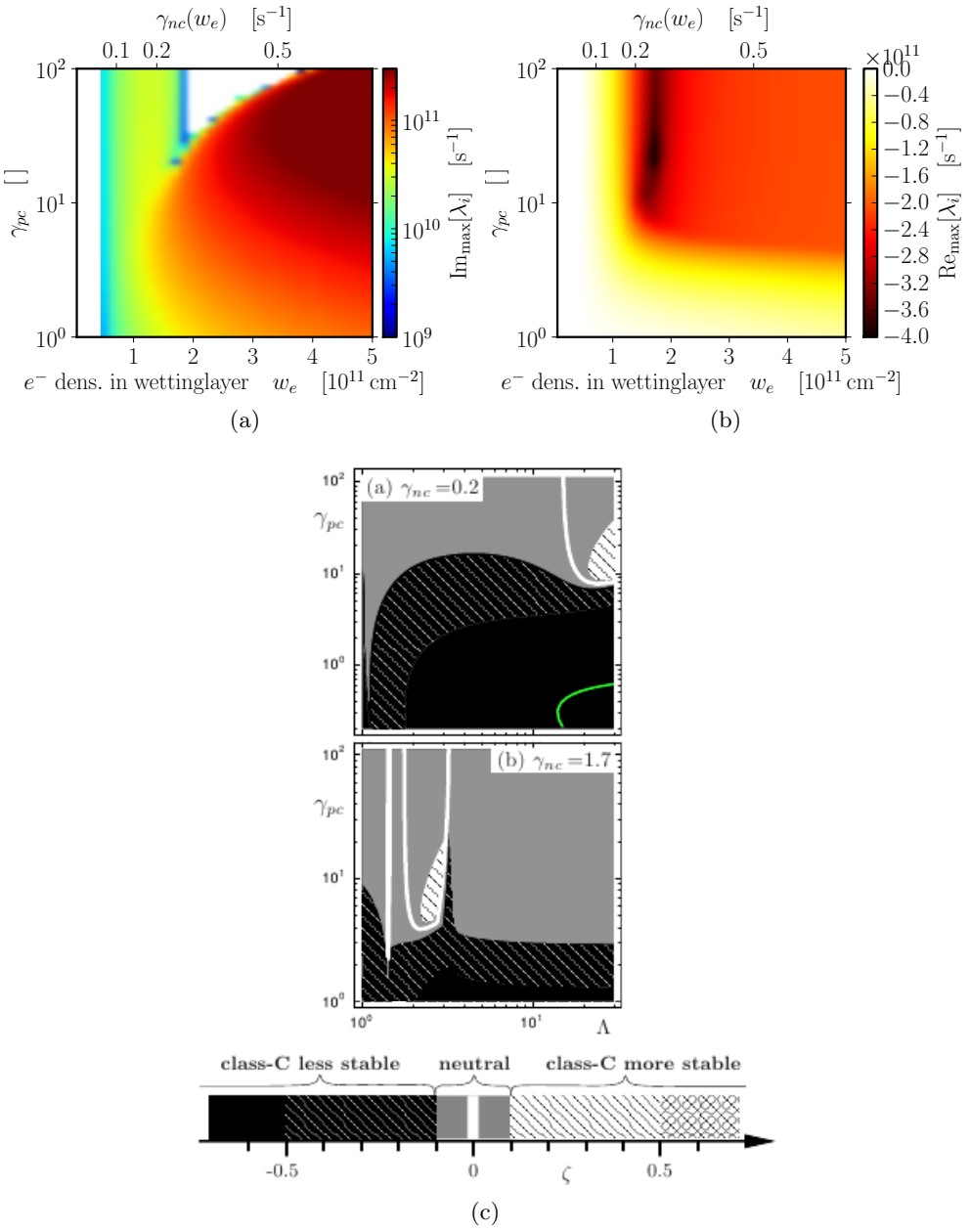

Figure A.6: (a-b) maximum imaginary and real part versus $\gamma_{pc} = \gamma/\kappa$ and electron density in the wettinglayer w_e, simulated with Bloch equations (Eqs. (2.51) to (2.53)) with $\kappa = 10^{11}\,\mathrm{s}^{-1}$ and $\tau_{sp}^{-1} = 10^8\,\mathrm{s}^{-1}$. Second x-axis shows $\gamma_{nc}(w_e) = {T_1}^{-1}(w_e)/\kappa$ (c) Graphic provided by [WIE14]. Stability parameter $\left(\zeta = \frac{\mathrm{Re}[\lambda_B]-\mathrm{Re}[\lambda_C]}{\mathrm{Re}[\lambda_B]}\right)$ versus γ_{pc} and pump Λ. The parameter ζ describes the relative deviation between the real part under class B $\mathrm{Re}[\lambda_B]$ and under class C $\mathrm{Re}[\lambda_C]$ conditions.

Deutsche Zusammenfassung

Mit dem Tag der technischen Realisierung einer ersten Besetzungsinversion in einem Drei-Niveau Rubin Festkörperlaser im Jahre 1960 , war der Weg für den Einzug des Lasers in alle Bereiche des gesellschaftlichen Lebens geebnet. Neben zahlreichen Anwendungsgebieten wie der Materialbearbeitung, der Unterhaltungsindustrie, der Messtechnik, der Spektroskopie, der Grundlagenforschung, der Kernfusion oder der Medizin, hat sich der Einsatz von Halbleiterlasern auch als Mittel der Wahl für optische Datenübertragung etabliert. Besonders Quantenpunkt-Laser sind mit ihren attraktiven Eigenschaften seit der Entwicklung ausgefeilter Herstellungsprozesse wie der Molekularstrahlepitaxie oder der metallorganischen Gasphasenepitaxie in den Fokus gerückt. Gegenüber herkömmlichen Halbleiterlasern sind sie durch einen niedrigeren Energie- und Materialverbrauch, einen niedrigen Amplituden-Phasenkopplungs-Faktor (α-Faktor), eine größere Toleranz zu optischer Rückkopplung und vor allem eine Temperaturunabhängigkeit des Schwellstroms charakterisiert. In gleichem Maße, wie die Tendenz zur Bauteilminiaturisierung von Signal-Transmittern und -Verstärkern in den Mikro- oder sogar Nanometerbereich anwächst, so wächst auch die Notwendigkeit einer Neuuntersuchung der altbekannten Erkenntnisse über Quantenpunkt-Laser hinsichtlich ihres Bifurkations- und Modulationsverhaltens. Vielversprechende Konsequenzen werden der Purcell-Verstärkung der spontanen Emission zugeschrieben. Grundlage für den Purcell-Effekt bildet die vergrößerte spontane Übergangsrate in einer kleiner werdenden Kavität und die starke Kopplung an eine einzige Feldmode mit einer maximierten photonische Zustandsdichte unter Vorraussetzung einer resonanten Licht-Materie-Wechselwirkung. In der Vergangenheit wurde gezeigt, dass die photonische Zustandsdichte auch durch die Kopplung an Oberflächen-Plasmonen in Kavitäten mit metallischer Außenwand auftritt. Tatsächlich tragen beide Effekte zum gewünschten Ergebnis bei.
Seit der Erkenntnis, dass die komplexen Dynamiken eines Quantenpunkt-Lasers durch die Halbleiter-Blochgleichungen beschrieben werden können und der Entdeckung der strukturellen Äquivalenz zwischen den bereits gut untersuchten Haken-Lorentz-Gleichungen und den Halbleiter-Blochgleichungen wurden große Mühen auf sich genommen, die bekannten Stabiliätscharakteristika auf eine moderne Lasertheorie zu übertragen. Eine anerkannte Methode analytischen Zugang zu der nichtlinearen Laserdynamik zu erhalten, ist es, die Polarisationsdynamik gemäß dem Versklavungsprinzip adiabatisch zu eliminieren, was die semiklassische Theorie in die klassischen, heuristisch motivierten Ratengleichungen überführt. Auf der Basis des Ratengleichungsregimes wurden bereits Stabilität und Modulationsverhalten unter Einfluss der spontanen Emission ausführlich untersucht, sowohl in semiklassischen, als auch in voll quantisierten Systemen. Auch die Stabilitätsänderungen, die sich unter Betrachtung der Polarisationsdynamik, externer optischer Lichteinspeisung und zeitverzögerter Rückkopplung ergeben, wurden bereits intensiv bearbeitet. Mit dieser Masterarbeit soll der Einfluss der spontanen Emission unter Berücksichtigung der Polarisationsdynamik untersucht und die Lücke dadurch geschlossen werden. Im Grundlagenkapitel wurden Die Gleichungssysteme motiviert, hergeleitet und dahingehend vereinfacht, den anfänglich fünf-dimensionalen Phasenraum im Blochregime ohne Informationsverlust auf drei Dimensionen zu reduzieren und die Ergebnisse zu visualisieren. Es wurde darauf Wert gelegt, das System so einfach wie möglich zu gestalten und trotzdem ein Mindestmaß an realistischen Eigenschaften einzubinden. Dazu zählt die Einführung von Streuraten, unter der Annahme von gleichen Elektron- und Lochdichten, mit denen Ladungsträger aus einer

Benetzungsschicht in die zur Laseremission beitragenden Quantenpunkte gestreut werden. Neben dem detaillierten Vergleich der beobachteten Dynamiken mit den Eigenwertspektren der linearisierten Systeme im Rahmen einer linearen Stabilitätsanalyse, wurde auch die stetige Korrespondenz zum Ratengleichungslimit für schnellen Polarisationszerfall aufgezeigt. Auf diese Weise wurde das System umfassend charakterisiert und verschiedene Stabilitätsregime (Klasse A, B, C) aufgezeigt. Auch der isolierte Einfluss der spontanen Emission und der Streuraten wurden untersucht. Eine bemerkenswerte Eigenschaft der spontanen Emission ist es, den Kavitätsverlusten entgegenzuwirken und die Laseremssion zu stabilisieren, was dazu führt, dass ein anfänglich chaotisches System unter Betrachtung der spontanen Emission periodisches oder sogar stabiles Verhalten aufweist. Es zeigt sich, dass die Einbindung der Polarisationsdynamik in einem System ohne optische Injektion oder zeitverzögerter Rückkopplung meist eine destabilisierende Wirkung hat. Dies äußert sich in einer Vergrößerung des Realteils füer kleineren Polarisationszerfall. Begründet liegt das in dem dritten Freiheitsgrad der Bloch Gleichungen, welcher aufgrund der adiabatischen Eliminierung nicht in den Ratengleichungen zu finden ist. Dieser erzeugt einen dritten Eigenwert, welcher eine Oszillation in der von Polarisation und elektrischem Feld aufgespannten Ebene hervorruft. Diese Wechselwirkung zwischen Polarisation und elektrischem Feld lässt sich unmittelbar einer Rabi Oszillation zuordnen. Je langsamer die Polarisation, desto größer ist die Amplitude der Oszillationen der Polarisation und desto größer auch die Resonanz mit einer externen Modulation.
Folglich wurden die jüngst erworbenen Erkenntnisses über Stabilitätswechsel im Falle der Kleinsignal-Antwort untersucht, ein linearer Effekt, in dem Auswirkungen dieser Art direkten Einfluss nehmen und beobachtet werden können. Hier wurde deutlich, dass Abweichungen zwischen Raten- und Blochgleichungen stets dort zu erwarten sind, wo Abweichungen im Eigenwertspektrum auftreten. Darüber hinaus stellt sich heraus, dass Polarisationsdynamik und spontane Emission zwei rivalisierende Effekte sein können, welche beide signifikanten und sehr individuellen Einfluss auf die Modulationstransferkurven nehmen. Die Polarisationsdynamik induziert meist eine Resonanzspitze, welche in den Ratengleichungen nicht zu beobachten ist. Die spontane Emission dämpft hingegen das Auftreten dieser Resonanz und führt bei einer hohen Rate, gepaart mit einer langsamen Polarisation zu einer Vergrößerung der übertragenen Intensität. Gleichzeitig wird die Bandbreite der Resonanzspitze deutlich vergrößert, wobei der steile Intensitätsabfall unterbleibt. Diese zusätzlichen Resonanzen nehmen maßgeblichen Einfluss auf das Modulationsverhalten und erscheinen nicht unter adiabatischer Eliminierung der Polarisation, weshalb eine Simulation einer realistischen Laserdynamik nicht mit vereinfachten Ratengleichungen durchgeführt werden sollte. Da die Rate der stimulierten Emission die maximale Modulationsbandbreite festlegt, wäre es interessant zu erfahren, ob dieser außerordentliche Peak exakt an dem Punkt erscheint, an dem die spontane Emission die Raten im System dominiert. Ein möglicher Ansatz wäre es, die stimulierten und spontanen Emissionsraten getrennt zu untersuchen. Es ist zu klären, ob die Purcell verstärkte stimulierte Emission diesem Verhältnis entgegenwirken kann. Andere Effekte, welche aus einer Kavitätsverkleinerung resultieren, wie die Änderung der Übergangsfrequenzen, die geringe Quantenpunktzahl, die höheren Gütefaktoren, die konstruktionsbedingte Temperaturerhöhung, und vor allem ihre Wechselwirkungen, gilt es zu untersuchen.

Bibliography

[ARE84] F. T. Arecchi, G. L. Lippi, G. P. Puccioni, and J. R. Tredicce: Deterministic chaos in laser with injected signal, Opt. Commun. **51**, 308–315 (1984).

[CHO99] W. W. Chow and S. W. Koch: Semiconductor-Laser Fundamentals (Springer, Berlin, 1999).

[CHO05] W. W. Chow and S. W. Koch: Theory of semiconductor quantum-dot laser dynamics, IEEE J. Quantum Electron. **41**, 495–505 (2005).

[DIN13] K. Ding, M. T. Hill, Z. C. Liu, L. J. Yin, P. J. van Veldhoven, and C. Z. Ning: Record performance of electrical injection sub-wavelength metallic-cavity semiconductor lasers at room temperature, Opt. Express **21**, 4728–4733 (2013).

[EIN17] A. Einstein: Zur Quantentheorie der Strahlung, Phys. Z. **18**, 121–128 (1917).

[GER98] J. M. Gérard, B. Sermage, B. Gayral, B. Legrand, E. Costard, and V. Thierry-Mieg: Enhanced spontaneous emission by quantum boxes in a monolithic optical microcavity, Phys. Rev. Lett. **81**, 1110–1113 (1998).

[GLO12] B. Globisch, C. Otto, E. Schöll, and K. Lüdge: Influence of carrier lifetimes on the dynamical behavior of quantum-dot lasers subject to optical feedback, Phys. Rev. E **86**, 046201 (2012).

[GRE12a] N. Gregersen, T. Suhr, M. Lorke, and J. Mørk: Quantum-dot nano-cavity lasers with purcell-enhanced stimulated emission, Appl. Phys. Lett. **100**, 131107 (2012).

[HAK75] H. Haken: Analogy between higher instabilities in fluids and lasers, Phys. Lett. A **A 53**, 77–78 (1975).

[HAK83] H. Haken: Synergetics, An Introduction (Springer, Berlin, 3 edition, 1983).

[HAK85] H. Haken: Light, Vol. 2 (North-Holland, Amsterdam, 1985).

[LAU09] E. K. Lau, A. A. Lakhani, R. S. Tucker, and M. C. Wu: Enhanced modulation bandwidth of nanocavity light emitting devices, Opt. Express **17**, 7790–7799 (2009).

[LIN12] B. Lingnau, K. Lüdge, W. W. Chow, and E. Schöll: Influencing modulation properties of quantum-dot semiconductor lasers by electron lifetime engineering, Appl. Phys. Lett. **101**, 131107 (2012).

[LOR13] M. Lorke, T. Suhr, N. Gregersen, and J. Mørk: Theory of nanolaser devices: Rate equation analysis versus microscopic theory, Phys. Rev. B **87**, 205310 (2013).

[LUE09] K. Lüdge and E. Schöll: Quantum-dot lasers – desynchronized nonlinear dynamics of electrons and holes, IEEE J. Quantum Electron. **45**, 1396–1403 (2009).

[LUE10] K. Lüdge and E. Schöll: Nonlinear dynamics of doped semiconductor quantum dot lasers, Eur. Phys. J. D **58**, 167–174 (2010).

[LUE11a] K. Lüdge: Modeling Quantum Dot based Laser Devices, in Nonlinear Laser Dynamics - From Quantum Dots to Cryptography, edited by K. Lüdge (WILEY-VCH Weinheim, Weinheim, 2012), chapter 1, pp. 3–34.

[LUE13] K. Lüdge, B. Lingnau, C. Otto, and E. Schöll: Understanding electrical and optical modulation properties of semiconductor quantum-dot lasers in terms of their turn-on dynamics, Nonlinear Phenom. Complex Syst. **15**, 350–359 (2012).

[MAI60] T. H. Maiman: Stimulated optical radiation in ruby, Nature **187**, 493 (1960).

[MAJ10] N. Majer, K. Lüdge, and E. Schöll: Cascading enables ultrafast gain recovery dynamics of quantum dot semiconductor optical amplifiers, Phys. Rev. B **82**, 235301 (2010).

[MAX65] J. C. Maxwell: A dynamical theory of the electromagnetic field, Phil. Trans. Roy. Soc. **155**, 459–512 (1865).

[NEO02] A. Neogi, C. W. Lee, H. O. Everitt, T. Kuroda, A. Tackeuchi, and E. Yablonovitch: Enhancement of spontaneous recombination rate in a quantum well by resonant surface plasmon coupling, Phys. Rev. B **66**, 153305 (2002).

[NIN90] C. Z. Ning and H. Haken: Detuned lasers and the complex lorenz equations: Subcritical and supercritical hopf bifurcations, Phys. Rev. A **41**, 3826–3837 (1990).

[NIN92] C. Z. Ning and H. Haken: Elimination of variables in simple laser equations, Appl. Phys. B **55**, 117–120 (1992).

[NIN10] C. Z. Ning: Semiconductor nanolasers, phys. stat. sol. (b) **247**, 774–788 (2010).

[OTT12] C. Otto, B. Globisch, K. Lüdge, E. Schöll, and T. Erneux: Complex dynamics of semiconductor quantum dot lasers subject to delayed optical feedback, Int. J. Bifurcation Chaos **22**, 1250246 (2012).

[PAU12] J. Pausch, C. Otto, E. Tylaite, N. Majer, E. Schöll, and K. Lüdge: Optically injected quantum dot lasers - impact of nonlinear carrier lifetimes on frequency locking dynamics, New J. Phys. **14**, 053018 (2012).

[Pre07] W. H. Press, B. P. Flannery, S. A. Teukolsky, and W. T. Vettering: Numerical Recipes (3rd ed.) (Cambridge University Press, Cambridge, 2007).

[SCH58] A. L. Schawlow and C. H. Townes: Infrared and optical masers, Phys. Rev. **112**, 1940 (1958).

[SCH87] E. Schöll: Nonequilibrium Phase Transitions in Semiconductors (Springer, Berlin, 1987).

[SUH10] T. Suhr, N. Gregersen, K. Yvind, and J. Mørk: Modulation response of nanoleds and nanolasers exploiting purcell enhanced spontaneous emission, Opt. Express **18**, 11230–11241 (2010).

[TUC85] J. R. Tucker and M. J. Feldman: Quantum detection at millimeter wavelengths, Rev. Mod. Phys. **57**, 1055 (1985).

[WEG10] M. Wegert, N. Majer, K. Lüdge, S. Dommers-Völkel, J. Gomis-Bresco, A. Knorr, U. Woggon, and E. Schöll: Nonlinear gain dynamics of quantum dot optical amplifiers, Semicond. Sci. Technol. **26**, 014008 (2011).

[WEI00] C. Weisbuch, H. Benisty, and R. Houdré: Overview of fundamentals and applications of electrons, excitons and photons in confined structures, J. Luminescence **85**, 271–293 (2000).

[WIE14] S. Wieczorek and W. W. Chow: Stabilising and destabilising effects of polarization dynamics in class c lasers with optical external injection or time-delayed feedback (2014).

[YAM91] Y. Yamamoto, S. Machida, and G. Björk: Microcavity semiconductor laser with enhanced spontaneous emission, Phys. Rev. A **44**, 657–668 (1991).